Bistatic Automotive Radar Sensing: Signal Processing for Motion Parameter Estimation

Author:
Ali MOUSSA

1st Supervisor:
Dr. Wei LIU

2nd Supervisor:
Dr. Charith ABHAYARANTE

A thesis submitted in fulfillment of the requirements
for the degree of Doctor of Philosophy

in the

Department of Electronic and Electrical Engineering
Faculty of Engineering
The University of Sheffield

April 2024

Declaration of Authorship

I, Ali MOUSSA, declare that this thesis titled, “Bistatic Automotive Radar Sensing: Signal Processing for Motion Parameter Estimation” and the work presented in it are my own. I confirm that:

- This work was done wholly or mainly while in candidature for a research degree at this University.
- Where any part of this thesis has previously been submitted for a degree or any other qualification at this University or any other institution, this has been clearly stated.
- Where I have consulted the published work of others, this is always clearly attributed.
- Where I have quoted from the work of others, the source is always given. With the exception of such quotations, this thesis is entirely my own work.
- I have acknowledged all main sources of help.
- Where the thesis is based on work done by myself jointly with others, I have made clear exactly what was done by others and what I have contributed myself.

Signed: **Ali Moussa**

Date: **2nd April 2024**

Abstract

Radar sensors are nowadays an integral part of a road vehicle for their ability of detecting targets and extracting information about their motion and location. However, little research has been done on the ability of a vehicle to operate such application when the transmitter is located externally, a setup commonly referred to as bistatic. This thesis incorporates the communication potential of new radio with the merits of bistatic radar to advance the existing automotive sensing technology. It proposes an application envisioned in a smart highway where a vehicle switches to an economic mode, and the long-range radar module relies on cooperative roadside transmitters to locate other road targets. Firstly, a proof of concept is developed using existing Fourier techniques to show the advantage of the bistatic setup over the popular monostatic counterpart. It is proven that a theoretical bistatic range up to twice the monostatic one may be achieved, as well as the ability of correctly locating targets with elevated noise levels (up to 3 dB). A sparse representation of the bistatic automotive radar signal model is then developed and a sparsity-based method for two-dimensional location and Doppler estimation is proposed. After that, an extension of this application to a multistatic scheme is proposed by deploying multiple cooperative roadside sensors, and adopting the group-sparsity concept for parameter estimation. Two methods for data association with varying complexity and performance are proposed with both achieving 100% pairing probability at typical noise levels in the presence of 2 targets. Finally, a rigorous signal model for the wideband case is derived and the associated artefacts are identified. A sparsity-based solution for decoupled motion parameter estimation is proposed which naturally resolves such unwanted artefacts. Extensive computer simulations were conducted to mimic a real automotive scenario and verify the capability of the proposed methods. It was shown through Monte Carlo trials, under different operational settings, that the proposed solutions can outperform the state-of-art bearing an added computational cost. In most cases the improvement in estimation accuracy is at least 1 resolution cell, and can range up to 20 resolution cells in some cases, meanwhile up to 40 folds increase in processing run-time was recorded with the proposed algorithms.

Acknowledgements

I would like to hugely thank Dr. Wei for his untenable support and guidance throughout the years. In particular, I am grateful for him for believing in myself at every stage and showing great patience during my journey. While I owe part of my success in completing this project to his constant motivation and integral teaching, I totally believe that his contribution to my university learning will be echoed in any future success, to which I am sincerely thankful. I also would like to thank Dr. Charith for his support, especially at the early stages of this project.

I would like to thank my family, and my lovely wife, Levi, for providing me with unlimited emotional and moral support.

I dedicate this thesis to my Mom and Dad who were the first to ever believe in myself and got me on the right path form a young age to eventually succeed at this level.

Contents

List of Figures

List of Tables

List of Abbreviations

1D	One **D**imensional
2D	Two **D**imensional
3D	Three **D**imensional
4D	Four **D**imensional
5G	Fifth **G**eneration
ACC	**A**daptive **C**ruise **C**ontrol
ADAS	**A**dvanced **D**river **A**ssistance **S**ystem
ADC	**A**nalogue-to-**D**igital **C**onverter
AWGN	**A**dditive **W**hite **G**aussian **N**oise
CBR	**C**oherent **B**istatic **R**adar
CC	**C**ross-**C**orrelation
CFAR	**C**onstant **F**alse **A**larm **R**ate
COTS	**C**ommercial **O**ff **T**he **S**helf
CRB	**C**ramer-**R**ao **B**ound
CS	**C**ompressive **Se**ensing
CSSM	**C**oherent **S**ignal **S**ubspace **M**ethod
CW	**C**ontinuous **W**ave
DAQ	**D**ata **AQ**-uisition
DEW	**D**istant **E**arly **W**arning
DFT	**D**iscrete **F**ourier **T**ransform
DOA	**D**irection **O**f **A**rrival
DoF	**D**egree **o**f **F**reedom
ECM	**E**lectronic **C**ounter-**M**easures
ESPRIT	**E**stimation of **S**ignal **P**arameters via **R**otational **I**nvariant **T**echniques
EVD	**E**igen **V**alue **D**ecomposition
FFT	**F**ast **F**ourier **T**ransform
FIM	**F**isher **I**nformation **M**atrix
FM	**F**requence **M**odulation
FMCW	**F**requency **M**odulated **C**ontinuous **W**ave
GNSS	**G**lobal **N**avigation **S**atellite **S**ystem
GS	**G**roup **S**parsity
GPS	**G**lobal **P**ositioning **S**ystem
HDTV	**H**igh-**D**efinition **T**ele**V**ision
HF	**H**igh **F**requency
IF	**I**ntermediate **F**requency
IOO	**I**lluminator **O**f **O**pportunity
ISSM	**I**ncoherent **S**ignal **S**ubspace **M**ethod
ITU	**I**international **T**elecommunication **U**nion
LASSO	**L**east **A**bsolute **S**hrinkage and **S**election **O**perator

LS	**L**east-**S**quares
LTE	**L**ong **T**erm **E**volution
LOS	**L**ine **O**f **S**ight
LPI	**L**ow-**P**robability of **I**intercept
ML	**M**aximum **L**ikelihood
MIMO	**M**ultiple-**I**nput **M**ultiple-**O**utput
MMIC	**M**onolithic **M**icrowave **I**ntegrated **C**ircuit
MMV	**M**ultiple **M**easurement **V**ectors
MUSIC	**MU**ltiple **SI**gnal **C**lassification
NCAP	**N**ew **C**ar **A**ssessment **P**rogram
NF	**N**oise **F**igure
NLS	**N**on-linear **L**east **S**quares
OFDM	**O**rthogonal **F**requency-**D**ivision **M**ultiplexing
OTH	**O**ver-**T**he-**H**orizon
PBR	**P**assive **B**istatic **R**adar
PDF	**P**robability **D**ensity **F**unction
PLL	**P**hase-**L**ocked **L**oop
PPS	**P**ulse-**P**er-**S**econd
RCS	**R**adar **C**ross **S**ection
RF	**R**adio **F**requency
RMSE	**R**oot-**M**ean-**S**quared **E**rror
SFCW	**S**tepped **F**requency **C**ontinuous **W**ave
SAR	**S**ynthetic **A**perture **R**adar
SMV	**S**ingle **M**easurement **V**ector
SNR	**S**ignal-to-**N**oise **R**atio
SVD	**S**ingular **V**alue **D**ecomposition
TV	**T**ele**V**ision
UAV	**U**nmanned **A**erial **V**ehicle
ULA	**U**niform **L**inear **A**rray
UTC	**C**oordinated **U**niversal **T**ime
V2I	**V**ehicle to **I**nfrastructre
VCO	**V**oltage-**C**ontrolled-**O**scillator

List of Symbols and Notations

B	modulation bandwidth	Hz
c	speed of light	m/s
d	antenna adjacent spacing	m
f_0	carrier frequency	Hz
f_s	sampling frequency	Hz
g_d	Doppler search grid index	
G_d	length of Doppler search grid	
g_p	polar location search grid index	
G_p	length of polar location search grid	
g_{ij}	Cartesian location search grid index	
G_t	signal gain at the transmitter	
G_r	signal gain at the receiver	
h	roadside sensor index	
H	number of roadside sensors	
i	horizontal index of the Cartesian search grid	
I	horizontal length of the Cartesian search grid	
j	vertical index of the Cartesian search grid	
J	vertical length of the Cartesian search grid	
k	target index	
K	number of targets	
l	antenna index	
L	number of antennas	
m	chirp index	
M	number of chirps	
n	sampled time index	
N	number of samples	
P_n	received noise power	W
P_t	transmitted signal power	W
t	continuous real time	s
t_f	fast time	s
T	time period	s
T_c	chirp time duration	s
ε, ε_{1-6}	sparse reconstruction error	
λ	wavelength	m
μ	modulation rate	s^{-2}
σ_{bi}	bistatic radar cross section	m^2
σ_{mono}	monostatic radar cross section	m^2
σ_e	estimated parameter standard deviation	
σ_n	noise standard deviation	

Chapter 1

Introduction

Radio detection and range finding (Radar), is a system that uses radio-waves to determine distance, direction and and radial velocity of objects in its vicinity. As with many other technologies, initial radar trials were for military use and were kept a secret during World War II. However, it has since found interest in many different civilian applications, as well as military ones. In this thesis, the focus is on the automotive application of radar, rapidly accelerated by the evolution of electric vehicles and autonomous driving. Recently, market leaders in automotive radar development and production, such as Continental, Bosch, and ZF, announced their flagship radar modules providing four-dimensional (4D) imaging, to support the ever anticipated level 5 driving with full automation capability [1, 2, 3]. Offering unprecedented technical specifications despite the miniaturisation of the radar modules, some systems are said to achieve up to 300 metres of range with their front long-range radar modules, ultimately placing them on the forefront of sensor supremacy.

The physics behind the basic operation of these radar modules is very well understood. A radio-wave which is transmitted through the air, gets reflected back after hitting an object, and is then collected via a sensor. The time difference between transmitted and the received signal relates to the distance of the illuminated object. So, the rationale behind achieving longer range without consuming more power is simply by minimising the losses in the travelling signal strength. What is interesting, however, is that no matter how much we reduce the losses inside the electrical circuits and improve the propagation medium for radar signals, we will always be limited by the natural expansion of radio-wave fronts, leading to what is known as propagation loss. In other words, the minimum power required to achieve 300 metres of range with the current geometry of the said state-of-art radar modules is in fact fixed. Nonetheless, what if it was possible to place either the transmitter or the receiver somewhat closer to the illuminated object, with the transmitter having more relaxed limitations on its operating power? It seems trivial that breaking the boundaries with radar range is theoretically possible by separating the transmitter from the receiver in a geometry that significantly reduces the radio-wave's travel distance (and consequently reduces the inevitable propagation losses), and offers extra flexibility and added operational benefits compared to the widely adopted monostatic radar that encapsulates both transmitters and receivers in one unit.

Improving performance in terms of resolution and accuracy is another area that has seen significant improvement in automotive radar. Yet, the challenge remains that illuminating an object using a single radio-wave source from a fixed angle can only achieve an asymptotic level of performance until some radical improvement comes into place. In this thesis, an alternative approach to automotive radar sensing is proposed. The commonly used monostatic radar, containing a transceiver system formed by a transmitter and receiver in a singular module, is replaced by a bistatic radar system where the transmitter operates independently and is physically separated from the receiver. In this proposed approach, the transmitters are incorporated with the road infrastructure and the vehicle's radar module is in a purely receiving mode. When multiple transmitters are considered, each transmit-receive pair forms a bistatic setup with the overall system forming what is known as a multistatic radar.

1.1 Aim and Objectives

In the wake of electrification and automation of vehicles, a great mass of research has been drawn into automotive radar sensing, being an integral part of such evolution. This inevitably motivates exploring the prospects of its application in a world of emerging wireless communication super-infrastructures, namely new radio (NR). Briefly, the aim of this research is to review the existing applications of automotive radar, and to provide some answers to the ever-lasting question of "What can be done better?". More concisely, we aim to improve the performance of automotive radar by targeting one or more of the following key areas: transmitted waveform, mode and geometry of transmission, and signal processing techniques.

Accordingly, the objectives of this research can be stated as follows.

1. Formulate the radar problem and determine the parameters to be estimated. This entails solving the geometry of the application and relating its parameters to the ones within the radar's deterministic capability.

2. Following the choice of desired radar waveform, transmission mode, and geometry, derive a rigorous mathematical signal model based on real-world considerations and permissible assumptions.
3. Propose a signal processing method for estimating the desired parameters from the raw signal data based on the model previously derived. In most cases, the proposed method should outperform the state-of-art in estimation performance and/or computational cost. However, in some cases, due to the uniqueness of the problem, matching the performance of the state-of-art either by direct adoption of its implementation or a modified approach is sufficient.
4. Test the radar application through computer simulations and generate the performance metrics under different settings in various scenarios.
5. Evaluate the performance of the application and suggest directions for future work.

The research conducted in this thesis naturally extends the literature in two well-developed areas: automotive radar sensing and bistatic radar. It also fills a gap created by combining the idea of bistatic radar with automotive sensing since such proposal not only presents a proof of concept based on the existing signal processing techniques, but further advances the state-of-art techniques through novel sparsity-based signal recovery. While the area of bistatic and multistatic radar is massively understudied, particularly for automotive applications, literature on wideband multi-dimensional motion parameter estimation in this framework is evidently limited. Here, the proposed application of bistatic automotive radar is extended to the wideband case with proposed motion parameter estimation methods falling under the category of advanced signal processing techniques. Moreover, to realise the bistatic operation of this application, a certain level of time synchronisation is required. This work does not explicitly focus on this scope of research, yet it provides pointers to some areas in the literature that would mutually benefit from turning some of the assumptions into research questions, ultimately translating to more advancement and development overall.

1.2 Structure of Thesis

This thesis, overall, is structured in a standard format where Chapter 2 reviews the existing literature around the topic, and the remaining Chapters

3-6 embody the contributions this research has added to the literature.

Chapter 2 is divided into two major sections. The first Section reviews automotive radar sensing from the early days to current applications and challenges. It offers the reader a broad insight into radar sensing ranging from the popular and commercial applications in the automotive industry, to the technical aspects of their functionality. The second Section reviews bistatic radar by highlighting its history, applications, and challenges. While both sections provide a rich review of their correspondent scopes, plenty of direction to relevant literature is provided for interested readers.

Chapters 3-6 follow a similar structure that inherently fulfils the objectives stated in Section 1.1. Each Chapter starts with an introduction that provides some brief literature review and formulates the problem, after which the content of each Section is highlighted. The remaining sections contain the signal model, the proposed data processing method, simulation results, and concluding remarks, respectively.

1.3 Contributions and Published Work

- Chapter 3 :
    - A novel application of bistatic radar is proposed for automotive sensing. The improvement to existing automotive radar is related to the mode and geometry of transmission.
    - A signal model is derived for the case of a single transmitting sensor and a single receiver for range, Doppler, and DOA estimation. The novelty here stems in the solution to the geometry of the bistatic automotive scenario and modelling the radar signal to allow unambiguous estimation of the motion parameters.
    - A bound on the acceptable time synchronisation is determined, and the unique conditions for such synchronisation task are formulated.

  The contributions of this Chapter are published in

  A. Moussa and W. Liu,“Enhanced Detection in Automotive Applications Using Bistatic Radar with Cooperative Roadside Sensors,”*2021 CIE International Conference on Radar (Radar)*, Haikou, Hainan, China, 2021, pp. 1649-1653.

- Chapter 4 :

  - Following the application of bistatic radar to automotive sensing proposed in Chapter 3, a sparsity-based method for joint range, Doppler, and DOA estimation is proposed. The improvement to existing automotive radar is related to the signal processing technique.
  - The Cramer-Rao bound is derived for this estimation problem and is used as the benchmark for the estimation performance.

  The contributions of this Chapter are published in

  A. Moussa and W. Liu, "A Two-Stage Sparsity-Based Method for Location and Doppler Estimation in Bistatic Automotive Radar," *2023 IEEE Statistical Signal Processing Workshop (SSP)*, Hanoi, Vietnam, 2023, pp. 487-491.

- Chapter 5
  - More novelty is introduced by extending this proposed application to multistatic configuration with multiple transmitting sensors. The improvement to existing automotive radar is related to the mode and geometry of transmission.
  - The drawbacks the state-of-art signal processing techniques face due to the inability of fusing multiple incoherent sources of information on the data level are discussed.
  - An algorithm employing group sparsity is proposed for motion parameter estimation by processing multistatic measurements simultaneously.
  - Two data association techniques are proposed for the case of multiple targets to allow pairing of the estimated location and Doppler parameters.

  The contributions of this Chapter are published in

  A. Moussa, W. Liu, Y. D. Zhang and M. S. Greco, "Multi-Target Location and Doppler Estimation in Multistatic Automotive Radar Applications," in *IEEE Transactions on Radar Systems*, vol. 2, pp. 215-225, 2024.

- Chapter 6
  - A rigorous signal model is derived for the wideband case in the proposed application.

- The artefacts associated with the wideband problem are identified and their effect on parameter estimation is discussed.
- Upper bounds on the modulation bandwidth are derived for each measurement domain to provide a criterion under which narrowband assumptions are no longer valid.
- A general approach for processing wideband signals in bistatic automotive radar is proposed using estimation in decoupled measurement domains.
- An algorithm based on group sparsity is proposed for processing wideband bistatic measurements for range, Doppler, and DOA estimation separately alongside solutions for pairing the estimated parameters from the decoupled domains.

The contributions of this Chapter are published in

A. Moussa and W. Liu, “Fast and Accurate Range-Doppler Estimation in Multi-Target Wideband Automotive FMCW Radar,” in *Proceedings of the 2020 International Conference on UK-China Emerging Technologies (UCET)*, Glasgow, UK, 2020, pp. 1-4.

The published and submitted articles during the production of this thesis are in chronological order as follows

1. A. Moussa, W. Liu, Y. D. Zhang and M. S. Greco, “Multi-Target Location and Doppler Estimation in Multistatic Automotive Radar Applications,” in *IEEE Transactions on Radar Systems*, vol. 2, pp. 215-225, 2024.
2. A. Moussa and W. Liu, “A Two-Stage Sparsity-Based Method for Location and Doppler Estimation in Bistatic Automotive Radar,” in *Proceedings of the 2023 IEEE Statistical Signal Processing Workshop (SSP)*, Hanoi, Vietnam, 2023, pp. 487-491.
3. A. Moussa and W. Liu,“Enhanced Detection in Automotive Applications Using Bistatic Radar with Cooperative Roadside Sensors,” in *Proceedings of the 2021 CIE International Conference on Radar (Radar)*, Haikou, Hainan, China, 2021, pp. 1649-1653.
4. A. Moussa and W. Liu, “Fast and Accurate Range-Doppler Estimation in Multi-Target Wideband Automotive FMCW Radar,” in *Proceedings of the 2020 International Conference on UK-China Emerging Technologies (UCET)*, Glasgow, UK, 2020, pp. 1-4.

1.4 Notations

Notations used in this thesis are as follows:

Vectors and matrices are represented as lowercase and uppercase boldface letters, respectively. Subscripts in *Italic* font used with variables (only) denote the index of the corresponding variable (such as θ_k, θ_h, $\theta_{h,k}$, θ_{g_p}, etc.), whereas any other subscripts or superscripts written in boldface font or used with constant predefined parameters are merely part of the notation.

$\{.\}^*$, $\{.\}^T$, and $\{.\}^H$ denote the complex conjugate, transpose, and Hermitian transpose of a vector or matrix, respectively.

$\circ$, $\otimes$, and $\odot$ denote the outer product, the Kronecker product, and the element-wise (Hadamard) multiplication, respectively.

diag$\{.\}$ returns a diagonal matrix, arg$\{.\}$ returns the argument of a complex number, eignval$\{.\}$ returns the eigenvalues, det$\{.\}$ returns the matrix determinant, vec$\{.\}$ is the vectorisation operation, E$\{.\}$ is the expectation computation, $\Re\{.\}$ is the real part extraction operation, $|.|$ is the absolute value, and $\mathcal{O}(.)$ is the asymptotic notation.

$||.||_1$, $||.||_2$, $||.||_{2,1}$, and $||.||_F$ are the ℓ_1-norm, ℓ_2-norm, $\ell_{2,1}$, and the Frobenius norm, respectively.

The range parameters and Cartesian coordinates are in metres (m), velocity parameters in metres per second (m/s), and DOA/angle parameters in degrees (°).

Chapter 2

Background Literature

2.1 Automotive Radar Sensing

2.1.1 History and Applications

The first literature on automotive radar sensing traces back to 1964 when [4] proposed using a RF system for prevention of vehicle collisions. More investigations on the use of radar for automotive sensing followed in endeavours supported by the U.S Department of transportation [5, 6, 7, 8, 7, 9, 10, 11, 12, 13], and meanwhile other efforts originated from some Japanese car manufacturers [14, 15]. In addition to that, the German Ministry of Science and Technology supported related work which was solely based on technologies and devices available at the time [16, 17, 18, 19].

In 1998, Mercedes Benz introduced the first commercial 76 GHz radar module for passenger vehicles, manufactured by Macom in the USA [20]. The post-prototype era continued with Jaguar, Toyota and BMW employing systems manufactured by Delphi, Bosch, and Denso, respectively, to support adaptive/autonomous cruise control (ACC) and brake assist [21]. In the early 2000s, most manufactures in the automotive industry offered a radar system at least in their flagship models. While the early promises focused on collision avoidance through the development of distance radar, these systems then allowed active comfort features in the integration of ACC and assisted braking [22].

Thus far the commercialisation of automotive radar was only about to take off. Driven by the evolution in hardware manufacturing, integration, and packaging encompassed by the silicon technology, the market volume boomed in the 2010s. The market demand for next generation radar sensors, lead to advanced front-end architecture showcased in Bosch's 5th generation radar sensor which includes a multiple-input multiple-output (MIMO) antenna array, a surface-mounted monolithic microwave integrated circuit

(MMIC), a 76-77 GHz voltage-controlled-oscillator (VCO) alongside a frequency sweep phase-locked loop (PLL), and analogue-to-digital converter (ADC) [2]. This sensor is used for the advanced driver assistance system (ADAS) including applications such as automatic emergency braking, ACC, Bosch driving assist, and road signature. A revolution that was once fuelled by the active safety mandate in the new car assessment program (NCAP) is now projected to achieve full-scale automated driving in the 2020s [23].

2.1.2 Motion Parameter Estimation: The Concept

Consider a transceiver[1] system with one transmitter and one receiver on a planar field transmits one frequency-modulated (FM) radio-wave pulse of known physical characteristics. Suppose this pulse hits an object and bounces back following the same trajectory to the transceiver which is capable of storing the signal in a digital buffer. It is trivial that the returning wave has a different time stamp to the original transmitted one after travelling a certain distance. Fortunately, the science has enabled us to estimate these time stamps due to the change in the original wave characteristics at the time of arrival. Since the travel time-difference is directly related to the distance between the transceiver and the scatterer, a simple signal processing task can accurately estimate the scatterer down-range. The estimated travel time-difference often referred to as round-trip time delay, by means of Fourier representation for instance, can then be expressed as an estimated frequency which is directly proportional to the distance [24].

Now consider a case where the scatterer is moving at a constant velocity which is much smaller than the speed of light c (speed at which radio-waves propagate). Suppose the transceiver transmits two pulses which are then reflected from the same object. Assume that the displacement caused by this moving scatterer does not change the estimated round-trip delay in the time domain by a margin sufficient to change the range-dependant estimated frequency of the two pulses. Thinking of the impinging waves as a series of complex numbers allows us to model the basic characteristics of the signals as frequencies and then more generally as phases (phasor representation for sinusoidal functions [25]). Although, the small displacement caused by the moving scatterer does not change the estimated frequency for both received pulses, the phasor representing the second pulse incurs a constant shift with respect to the first pulse. Assuming the original position of the phasor is

---

[1] A transceiver is a combination of transmitter and a receiver in a single package.

known, the phase difference can be mapped to estimate the velocity of the moving scatterer [26, 27].

The same concept of micro-displacement caused by the motion of the scatterer which enables the estimation of velocity can be implemented to estimate the azimuth of the scattered signal. Suppose there exists a second receiver carefully placed next to the first one. It follows that it receives the scattered signal with a very small-time delay (presumably equal to the that at the first receiver) that does not change the estimated frequency, yet it changes the phase. Assuming the phase is known at the first receiver, the phase difference between the signals at the two receivers can then be mapped to estimate the azimuth of the scatterer, also known as the DOA [28, 29].

If a third receiver was placed in a plane perpendicular to the previous one, the same theory leads to the ability of estimating the elevation of the scatterer, which in essence is another form of DOA albeit in a different plane [30, 31].

To summarise, the range of the scatterer can be estimated by the frequency difference between the transmitted and received pulses. The velocity can be estimated using the phase difference between two consecutive pulses reflected from the moving scatterer. The azimuth can be estimated by the phase difference between pulses received at more than one co-located receivers. [32] provides a very straightforward explanation to these three concepts.

2.1.3 Transmission Waveforms

In the context of automotive radar, various waveforms have been studied and applied. They have diverse specifications and performance metrics. A summary of five popular waveforms is included in Table 2.1 [33]. With radar waveform design, emphasis is usually on the ability and mechanism of extracting range and/or Doppler information and the resolution metrics associated with each. Continuous wave (CW) is the most simple waveform which can also be transmitted in the form of pulses (Pulsed CW). In addition, different forms of modulation can be applied including frequency modulated (FM)-CW, stepped frequency (SF)-CW, orthogonal frequency-division multiplexing (OFDM).

- The CW radar signal of carrier frequency f_0 received from a moving target results in Doppler frequency shift f_d which can be extracted by conjugately mixing the received signal with the transmitted one. Therefore Doppler resolution increases with the duration of signal capture,

TABLE 2.1: Radar waveforms

Waveform Type	**Transmit Waveform $s(t)$**	**Resolution**
CW	$e^{j2\pi f_0 t}$	$\delta f_d = \frac{1}{T}$
Pulsed CW	$\Pi(T_p)e^{j2\pi f_0 t}$	$\delta R = \frac{cT_p}{2}, \delta f_d = \frac{1}{T_p}$
FMCW	$e^{j2\pi(f_0 t + 0.5\mu t^2)}, \mu = \frac{B}{T_c}$	$\delta R = \frac{c}{2B}, \delta f_d = \frac{1}{MT_c}$
SFCW	$e^{j2\pi f_n t}, f_n = f_0 + (n-1)\delta f$	$\delta R = \frac{c}{2B}, \delta f_d = \frac{1}{MT_c}$
OFDM	$\sum_{n=0}^{N-1} I(n)e^{j2\pi(f_0+n\Delta f)t}$	$\delta R = \frac{c}{N\Delta f}, \delta f_d = \frac{1}{MT_N}$

denoted by T. Such signals do not carry range information due to the continuous nature and lack of time stamping [34].

- Pulsed CW radar signals offer range estimation capability since the CW is now transmitted as a rectangular pulse $\Pi(T_p)$ with known time period T_p and repetition intervals. Correlation allows estimating the time stamp of the received pulse which directly corresponds to the range of the target. Shorter pulses lead to better range resolution and worse Doppler resolution.

- FMCW, also known as chirp, allows accurate and simultaneous range and Doppler estimation, hence its popularity in the automotive industry. It offers high range resolution, which is inversely proportional to the modulation bandwidth B, thanks to pulse compression. Unlike pulsed CW radar, frequency modulation allows mapping the time stamping task to the frequency domain. Conjugate mixing then permits extracting this range-dependent frequency information at a low sampling rate. The resolution in Doppler frequency depends on number of pulses M used and their width T_c.

- In SFCW, the frequency varies in a discrete manner with increments of Δf and the range information is extracted via inverse Fourier transform. The maximum range is therefore dictated by Δf.

- OFDM is popular for the coexistence of radar features with communication capability, hence the suitability for vehicle-to-vehicle communication [35]. The cyclic prefix and sub-carrier spacing ensure orthogonality in the time and frequency domains, respectively, which improves spectral efficiency [36]. As well as frequency modulation, the waveform is formed from an N-point arbitrary sequence $I(n)$ and detection is done via frequency domain channel estimation.

2.1.4 Narrowband vs Wideband

In wireless communications, the term narrowband refers to channels where the frequency response is flat over the *coherence time*. On the contrary, wideband channels are ones where the information bandwidth is larger than the *coherence bandwidth*. The latter is related to the delay spread profile of a channel and can only be statistically modelled. Wideband channels can produce higher data rates compared to narrowband ones while requiring more power to do so.

The classification of signals in radar terms is not as distinctive as in wireless communications. It is well known that wideband signals have many advantages over narrowband ones, but such classification criterion is merely comparative. Wideband signals carry higher bandwidths, offer better range resolution, higher signal-to-noise ratio (SNR) within a resolution cell, more secrecy of illumination, and better immunity to active and passive interference/jamming [37]. However, at what point does a narrowband radar signal become wideband/ultra-wideband?

A thorough search through the radar literature leads to no direct answer to the question above. In [38], three criteria for signal-band classification are presented, and are purely based on predefined thresholds recommended by the regulating authorities rather than their signal processing and application-level implications. In reality, in range and Doppler domains a practical classification of these signals is directly related to the Doppler effect imposed by the scattering environment. In other words, reflections from stationary targets can be treated identically from a signal processing perspective regardless of modulation bandwidth. In DOA estimation, narrowband assumptions are independent of the Doppler effect, and therefore the criteria for wideband classification are related to the geometry of the antenna array and its resolution capability.

To summarise, in radar literature, the notion of wideband is associated with signals carrying bandwidths relatively larger than conventional ones for high performance applications. Technical papers working on signal processing schemes for wideband applications usually consider more complex signal models that take into account the effect of micro-Doppler and increased bandwidth on range and DOA profiles. One dilemma remains that high performance techniques with super-resolution capabilities are obliged to wideband assumptions for signals that may otherwise be treated as narrowband using conventional Fourier-based methods for instance.

2.1.5 The Motion Parameter Estimation Problem

In the sequel, focus will be on the narrowband representation and processing of FMCW signals. Without loss of generality, in the context of automotive radar, a chirp is a pulse of a frequency-varying wave modulated linearly around a centre frequency f_0 spanning a pre-defined bandwidth B. Conventionally, the chirp signal is generated in an analogue way via a voltage controlled oscillator (VCO). A frame of multiple identical chirps is traditionally transmitted in order to detect multiple targets followed by range-Doppler estimation. Multiple receiving antennas, often in a form of a linear antenna array, are used for DOA estimation. Once received, the analogue chirp signals are conjugately mixed with the transmitted ones in a process called dechirping. Fortunately, the dechirped signals carry frequencies much lower than the modulation bandwidth. This makes the use of digital data acquisition (DAQ) systems very convenient in low cost applications. The dechirped signals at each antenna of the antenna array are then digitally processed. Accordingly, the three main tasks of motion parameter estimation for automotive radar sensing are: range estimation, relative velocity (Doppler) estimation , and DOA/azimuth estimation.

Range Estimation: A stationary target placed at range R from the radar produces a round-trip delay τ such that

$$\tau = \frac{2R}{c}, \tag{2.1}$$

where c is the propagation speed. Assuming the transmitted chirp is $s(t)$, the received chirp becomes

$$x(t) = as(t-\tau) + w(t), \tag{2.2}$$

where the magnitude of a represents the gains and losses incurred from diffraction (RCS), propagation (path-loss), and receiving (antenna gain), and $w(t)$ is the additive white Gaussian noise (AWGN). With complete knowledge of $s(t)$, conjugately mixing the latter with the delayed version $x(t)$ and filtering out the unwanted mixing products results in the dechirped signal $y(t)$ such that

$$y(t) = x(t)s^*(t) \tag{2.3}$$

It is important to note that dechirping which typically occurs in the analogue domain is an alternative to match filtering due to its inexpensive implementation and the significant reduction in the bandwidth of what is known as the beat signal.

After some mathematical expansion and simplification, y can be written as

$$y(t) \approx a \exp\left\{-j2\pi\left[\frac{2f_0R}{c} + \frac{2\mu R}{c}t\right]\right\} + w(t), \tag{2.4}$$

where $\mu = B/T_c$ denotes the modulation rate with T_c being the modulation period. A simple dimensional analysis of the terms inside the exponential show that $\frac{2f_0R}{c}$ is dimensionless and $\frac{2\mu R}{c}$ is a range dependent frequency. Therefore, any frequency estimation technique applied on y allows estimating the range R of the target. Following the Rayleigh criterion of interferometry [39], the range resolution can then be defined as

$$\delta R = \frac{c}{2B}. \tag{2.5}$$

In practice, the signal y is sampled for digital implementation. So, time t is replaced with n/f_s where $n = 0, 1, \ldots, N-1$ is the sampling index and N is the total number of samples collected at a rate f_s. According to the Nyquist theorem, in order to recover the range without ambiguity, the sampling rate should be at least twice the range dependent frequency. So, the maximum unambiguous range is

$$R_m = \frac{f_s c}{2\mu}. \tag{2.6}$$

Velocity Estimation: When the target is non stationary, and moving with radial velocity v, the round-trip delay of the received signal becomes

$$\tau(t) = \frac{2(R + vt)}{c}, \tag{2.7}$$

where v is positive when the target is moving away from the receiver and negative when it is approaching the receiver. This time dependent delay leads to what is known as the Doppler effect. Multiple chirps periodically transmitted with a repetition interval T are then needed to estimate the Doppler frequency. Denote by $m = 0, 1, \ldots, M-1$ the chirp index (widely known as the slow-time index), with M being the total number of collected chirps. The sampled real time can then be defined as $t = \frac{n}{f_s} + mT$ and n now denotes the fast-time index. To account for these extensions, the received signal y becomes

$$y[m,n] \approx a \exp\left\{-j2\pi\left[\frac{2f_0R}{c} + (f_r + f_d)\frac{n}{f_s} + f_d mT\right]\right\} + w[m,n], \tag{2.8}$$

where $f_r = \frac{2\mu R}{c}$ and $f_d = \frac{2f_0 v}{c}$. From the term $(f_r + f_d)\frac{n}{f_s}$, the original range frequency f_r is now shifted by a Doppler frequency f_d in the fast time. In most cases f_d is much smaller than f_r and is typically discarded in that term, but we keep it here for the sake of generality. From the term $f_d mT$ it is trivial that any frequency estimation technique applied across the slow time allows estimating the velocity of the target. Similarly to range estimation, Rayleigh and Nyquist considerations dictate the resolution and the maximum unambiguous velocity respectively as

$$\delta v = \frac{c}{2f_0 MT} \tag{2.9}$$

and

$$v_m = \frac{c}{4Tf_0}. \tag{2.10}$$

DOA Estimation: The measurement system described previously can be extended to include multiple receiving antennas co-located linearly in a so-called uniform linear array (ULA) [40]. Under certain target assumptions such as point sources and far-field approximation [41], the round-trip delay defined before can now be modified to include the extra delay incurred at each antenna of the antenna array. By letting the first antenna antenna be a reference and the spatial index be $l = 0, 1, \ldots, L-1$ with L being the total number of antennas, the round-trip delay at the l-th antenna due to one target can be written as

$$\tau(t,l) = \frac{2(R + vt) - ld\sin\theta}{c}, \tag{2.11}$$

where d is the adjacent antenna spacing and θ denotes the DOA. For K targets, the three-dimensional (3D) FMCW radar output signal can be written as

$$\begin{aligned} y(l,m,n) \approx \sum_{k=1}^{K} a_k \exp\left\{-j2\pi\left[\frac{2f_0R_k}{c} + (f_{r,k} + f_{d,k})\frac{n}{f_s} + f_{d,k}mT + \frac{f_0 d\sin\theta_k}{c}l\right]\right\} \\ + w(l,m,n), \end{aligned} \tag{2.12}$$

The term $\frac{f_0 d \sin\theta_k}{c} l$ induces a uniform phase shift across L antennas allowing the estimation of θ through frequency estimation in the spatial domain. Note that one should not confuse the said with the need for phase estimation to recover the DOA information. What is explicitly needed here is to estimate the frequency at which the phase changes across the antennas. The DOA resolution can be defined as

$$\delta\theta = \frac{c}{f_0 L d \cos\theta}. \tag{2.13}$$

Typically, d is chosen to be equal to $\lambda/2$, where λ denotes the wavelength, which achieves the maximum unambiguous DOA range $[-90°, 90°]$.

2.1.6 Signal Processing Techniques: The State-of-Art

Discrete Fourier Transform

It is now clear from (2.12) that the range, Doppler and DOA information can be extracted through frequency estimation in the fast-time, slow-time, and antenna domains, respectively. The discrete Fourier transform (DFT) can be applied in all three domains simultaneously. The fast Fourier transform (FFT) [42] is an efficient implementation of the DFT and provides an optimal approach for calculating a 3D periodogram [43]. The low complexity of the FFT-based estimation, $\mathcal{O}(LMN \log LMN)$, makes it an attractive candidate for motion parameter estimation, hence its wide use in the automotive industry.

After applying a 3D FFT to (2.12), the resulting spectrum can be represented as [44]

$$Y[l_f, m_f, n_f] = \sum_{l=0}^{L-1} \sum_{m=0}^{M-1} \sum_{n=0}^{N-1} y[l, m, n] \exp\left\{-j2\pi \left(\frac{l_f l}{L} + \frac{m_f m}{M} + \frac{n_f n}{N}\right)\right\}. \tag{2.14}$$

Accordingly, the indices of the spectrum peak $|Y(l_f, m_f, n_f)|$ attain the range, Doppler and DOA information according to the following relations respectively:

$$l_f = \frac{f_0 L d \sin\theta}{c}, \quad m_f = f_d M T, \quad n_f = \frac{(f_r + f_d) N}{f_s}. \tag{2.15}$$

Conventionally, constant false alarm rate (CFAR) methods to deal with time-varying noise and interference [34] are used in the detection stage. A target is therefore declared present in a particular 3D cell when the following condition is satisfied:

$$|Y[l_f, m_f, n_f]|^2 > \epsilon_T + \sigma_v^2[l_f, m_f, n_f] \quad \forall\, l_f, m_f, n_f, \tag{2.16}$$

where ϵ_T is the CFAR threshold and $\sigma_v^2[l_f, m_f, n_f]$ is the noise variance around the cell. The main drawback of the DFT is that resolution is dictated by the Rayleigh criterion. Sub-grid accuracy may however be achieved post-processing. [45] provides an overview of such frequency refinement techniques and emphasises their sensitivity to the time-domain window used. Interpolation can also be used for subgrid DFT-based estimation by using the two adjacent values around a periodogram peak [46].

Maximum Likelihood

An intuitive approach to determining the unknown parameters R_k, θ_k and v_k is by solving the following maximum likelihood (ML) problem

$$\min_{\boldsymbol{R},\boldsymbol{\theta},\boldsymbol{v},\boldsymbol{a}} \sum_{l=0}^{L-1} \sum_{m=0}^{M-1} \sum_{n=0}^{N-1} \Bigg| y[l,m,n] - \sum_{k=1}^{K} a_k \exp\Bigg\{ -j2\pi \Bigg[\frac{2f_0 R_k}{c} + (f_{r,k} + f_{d,k}) \frac{n}{f_s} \\ + f_{d,k} mT + \frac{f_0 d \sin\theta_k}{c} l \Bigg] \Bigg\} \Bigg|^2, \tag{2.17}$$

where $\boldsymbol{R}$, $\boldsymbol{\theta}$, $\boldsymbol{v}$, and $\boldsymbol{a}$ are the vectors containing R_k, θ_k, v_k and a_k for all targets, respectively. (2.17) is clearly a non-linear least squares (NLS) problem and since $w[l,m,n]$ has Gaussian distribution, it naturally falls under the ML framework [43]. This estimator can offer resolution beyond the Rayleigh limit but is practically very difficult to solve due to the computational complexity that increases with the granularity of the search space. Due to such prohibitive computational cost, alternative method with lower computational cost and super-resolution capability have been developed.

Subspace-based Algorithms

This class of signal processing requires sufficient SNR in large sample spaces in order to exploit the eigenstructure of signals for high resolution parameter estimation. It can be seen as a suboptimal alternative to (2.17) since estimating the sample covariance matrix provides a good ML estimate of the eignvalues and the associated eigenvectors. Two popular algorithms are reviewed here: multiple signal classification (MUSIC) [47] and estimation of signal parameters via rotation invariant technique (ESPRIT) [48].

MUSIC: 1D MUSIC can be applied directly to either of the dimensions in (2.12) for parameter estimation; however this approach requires further signal processing in multi-target scenarios in order to associate the parameters with each other [41]. This has led researchers to develop multi-dimensional versions of MUSIC for joint parameter estimation [49]. Recently, 2D MUSIC was used in [50] for joint Doppler-DOA estimation, in [51] for range-DOA estimation, and in [52] for range-Doppler mapping. In [53] tensor decomposition was implemented for the realisation of 3D MUSIC to jointly estimate range, Doppler and DOA. The main drawback in multi-dimensional MUSIC is the computational complexity which lies in the cost of eigenvalue decomposition (EVD) ($\mathcal{O}(LMN)^3$ for the 3D case). In the following, an application of 1D MUSIC for DOA estimation is presented

1. Firstly, the antenna and fast-time domains are considered and the collected data $y[l,m,n]$ is arranged in a 2D matrix $\mathbf{Y} \in \mathbb{C}^{L\times N}$, the sample covariance matrix $\mathbf{R} \in \mathbb{C}^{M\times M}$ is estimated as

$$\mathbf{R} = \frac{1}{N}\sum_{n=0}^{N-1} \mathbf{y}[n]\mathbf{y}^H[n], \tag{2.18}$$

   where $\{.\}^H$ is the conjugate transpose, and $\mathbf{y}[n]$ is the n-th column of $\mathbf{Y}$.

2. EVD is then derived according to

$$\mathbf{R} \approx \mathbf{Q}\boldsymbol{\Lambda}\mathbf{Q}^H \tag{2.19}$$

   where $\boldsymbol{\Lambda}$ contains the eigenvalues and $\mathbf{Q}$ contains the signal and the noise eigenvectors. $\mathbf{Q}$ can be sorted such that the signal eigenvectors correspond to the largest eigenvalues which allows separating the noise eigenvectors $\mathbf{Q_n}$ from the signal eigenvectors $\mathbf{Q_s}$ assuming the number of targets K that form the signal subspace is known. Accordingly, $\mathbf{Q_n}$ can be written as

$$\mathbf{Q_n} = [\mathbf{Q}[K+1], \mathbf{Q}[K+2], \dots, \mathbf{Q}[M]] \tag{2.20}$$

3. Denote by $\mathbf{a}$ the vector containing the DOA information for the k-th target such that

$$\mathbf{a}(\theta_k) = \left[1, e^{-j2\pi\frac{f_0 d \sin\theta_k}{c}}, \ldots, e^{-j2\pi\frac{f_0 d \sin\theta_k (L-1)}{c}}\right]. \tag{2.21}$$

   The orthogonality property between $\mathbf{a}(\theta_k)$ and $\mathbf{Q_n}$ can be exploited and the DOA pseudospectrum can be calculated as

$$P(\theta) = \frac{1}{\mathbf{a}(\theta)^H \mathbf{Q_n} \mathbf{Q_n}^H \mathbf{a}(\theta)}, \quad \theta \in [-90^\circ, 90^\circ] \tag{2.22}$$

   whose K peaks correspond to the DOAs of the targets.

ESPRIT: This method relies on the shift invariance property in the measurement domain hence its emergence as a suitable technique for DOA estimation in ULAs where all the antennas have the same pattern. Denote by $\mathbf{A} \in \mathbb{C}^{L\times K}$ the antenna array steering matrix and then consider the follow decomposition

$$\mathbf{A}_2 = \mathbf{A}_1 \mathbf{\Psi}, \tag{2.23}$$

where $\mathbf{A}_1$ and $\mathbf{A}_2$ are constructed from the rows of $\mathbf{A}$ of indices $0, 1, \ldots, N-2$ and $1, 2, \ldots, N-1$, respectively; $\mathbf{\Psi}$ is a diagonal matrix containing the complex exponentials of the radial rotations. Similarly, the signal subspace $\mathbf{Q_s}$ can then be decomposed as

$$\mathbf{Q_{s2}} = \mathbf{Q_{s1}} \mathbf{\Phi}, \tag{2.24}$$

where $\mathbf{\Phi}$ and $\mathbf{\Psi}$ have the same eigenvalues. Since $\mathbf{Q_{s1}}$ and $\mathbf{Q_{s2}}$ have full column rank, it follows that the matrix $\mathbf{\Phi}$ is uniquely given by

$$\mathbf{\Phi} = \left(\mathbf{Q_{s1}}^H \mathbf{Q_{s1}}\right)^{-1} \mathbf{Q_{s1}}^H \mathbf{Q_{s2}}. \tag{2.25}$$

The DOA estimates can finally be determined as

$$\boldsymbol{\theta} = \arcsin\left[\arg(\mathrm{eignval}(\mathbf{\Phi}))/(-2\pi f_0 d/c)\right], \tag{2.26}$$

where arg{.} returns the argument of a complex number and eignval{.} returns the eigenvalues.

Compressive Sensing

The compressive sensing (CS) theory was first introduced and developed in [54] and [55]. It stems from the idea that signals may be in reality be sparse in some domain. To illustrate this, a superposition of 6 distinct sinusoids is shown in Figure 2.1. Clearly, the samples occupy the whole time domain whereas only a few non-zeros are present in the frequency spectrum. It follows that sampling may be done below the rates imposed by the well-celebrated Shannon-Nyquist theorem [56] such that the recovery is dictated by the sparsity of the signal rather than the bandwidth [57]. This revelation was followed by a wide adoption of sparse representation for source localisation in sensor arrays, mainly for DOA estimation [58, 59]. Then, motivated by the super-resolution capability and the incorporation of parameter-based optimisation techniques, the CS framework became a popular topic in the field of radar imaging with many exhibits that it can outperform the state-of-art [60, 61, 62, 63]. The automotive industry was thereby fast to conduct extensive research on the applicability of sparse sensing for high resolution motion-parameter estimation and interference reduction [64, 65, 66, 67, 68, 69].

In a sparse representation, the received radar signal is represented as projection on a basis comprising of a linear combination of K basis vectors. In the case of DOA estimation, the length of the measurement domain is L and the N fast-time samples are referred to as snapshots. Recall $\mathbf{Y}$ which can be written in a matrix format as

$$\mathbf{Y} = \mathbf{A}\mathbf{X} + \mathbf{W} \tag{2.27}$$

where $\mathbf{X} \in \mathbb{C}^{K \times N}$ contains the complex amplitudes of the targets, and $\mathbf{W} \in \mathbb{C}^{L \times N}$ is the AWGN. Sparsity is then introduced by generating a DOA search grid of length K_g from all the potential incident angles such that $K_g >> K$. A steering matrix $\mathbf{A_g} \in \mathbf{C}^{L \times K_g}$ is then constructed such that its k_g-th column corresponds to a DOA in the search grid. Accordingly, $\mathbf{Y}$ can be rewritten as

$$\mathbf{Y} = \mathbf{A_g}\mathbf{X_g} + \mathbf{W} \tag{2.28}$$

where $\mathbf{X_g} \in \mathbb{C}^{K_g \times N}$ is a column-sparse matrix whose n-th column only contains K non-zero values corresponding to the DOAs of the targets. So, the latter can be estimated by reconstructing $\mathbf{X}_g$ from $\mathbf{Y}$ and $\mathbf{A_g}$. That is equivalent to estimating a support set $\mathcal{S}$ containing the indices of the non-zero

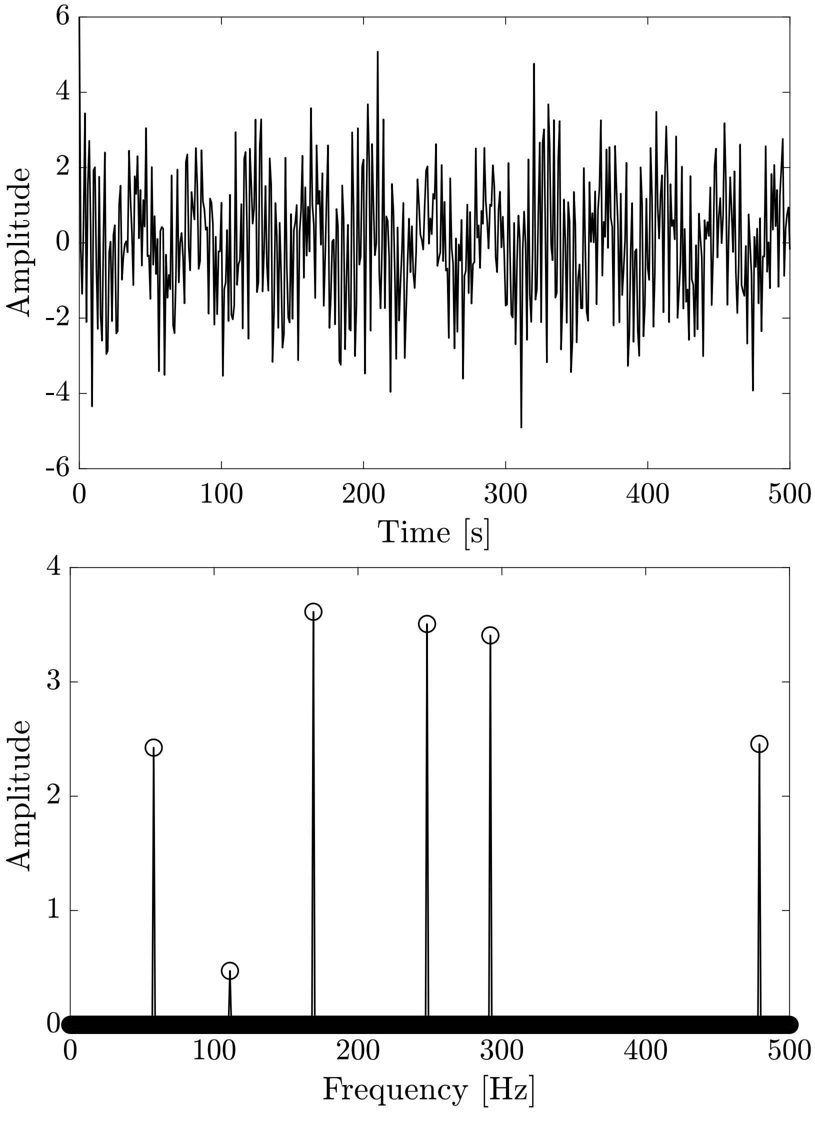

FIGURE 2.1: Samples of 6 sinusoids in time (top) and frequency (bottom) domains.

entries. A common assumption in the narrowband framework is that DOAs of the targets are exactly consistent among all snapshots. In other words, all columns in $\mathbf{X_g}$ share the same support. This problem falls under the so-called multiple measurement vectors (MMV) framework, and may be solved in two ways. A simple approach is to consider each column separately and the problem reduces to a single measurement vector (SMV) one and the final result can be combined through averaging for instance. So, consider the following optimisation

$$\min_{\mathbf{x}_{\mathbf{g},n}} \|\hat{\mathbf{x}}_{\mathbf{g},n}\|_0 \quad \text{subject to} \quad \|\mathbf{y}_n - \mathbf{A_g}\hat{\mathbf{x}}_{\mathbf{g},n}\|_2 \leq \varepsilon, \tag{2.29}$$

where $\mathbf{y}_n$ and $\mathbf{x}_{\mathbf{g},n}$ represent the n-th column of $\mathbf{Y}$ and $\mathbf{X_g}$ respectively, $\hat{\mathbf{x}}_{\mathbf{g},n}$ denotes the estimated version of $\mathbf{x}_{\mathbf{g},n}$, $\|.\|_0$ is the ℓ_0 norm which returns the number of non-zero entries in its argument, and $\|.\|_2$ is the ℓ_2 norm which returns the Euclidean distance, and ε is the allowed error bound. Since (2.29) is difficult to solve due to the NP-hardness of the ℓ_0 norm, a popular relaxation is typically introduced by enforcing sparsity through the ℓ_1 norm which returns the sum of the absolute values of the argument. Therefore, (2.29) becomes

$$\min_{\mathbf{x}_{\mathbf{g},n}} \|\hat{\mathbf{x}}_{\mathbf{g},n}\|_1 \quad \text{subject to} \quad \|\mathbf{y}_n - \mathbf{A_g}\hat{\mathbf{x}}_{\mathbf{g},n}\|_2 \leq \varepsilon, \tag{2.30}$$

where $\|.\|_1$ is the ℓ_1 norm. The above problem is convex and can be solved using the least absolute shrinkage and selection operator (LASSO) technique [70].

A more efficient approach for solving this MMV problem is by employing the concept of group sparsity (GS). To illustrate this, consider the following optimisation problem

$$\min_{\mathbf{X_g}} \|\hat{\mathbf{X}}_\mathbf{g}\|_{2,1} \quad \text{subject to} \quad \|\mathbf{Y} - \mathbf{A_g}\hat{\mathbf{X}}_\mathbf{g}\|_F \leq \varepsilon, \tag{2.31}$$

where $\hat{\mathbf{X}}_\mathbf{g}$ denotes the estimated version of $\mathbf{X_g}$, $\|.\|_{2,1}$ is the $\ell_{2,1}$ norm which returns the ℓ_2 norm across every row of a matrix followed by the ℓ_1 norm across the resulting vector, and $\|.\|_F$ is the Frobenius norm. The problem in (2.31) can be solved using the group LASSO technique [71]. However, as the number of snapshots increases, the computational complexity increases dramatically. To overcome this issue, a projection of $\mathbf{Y}$ to a signal subspace that has a lower dimension can be performed using singular value decomposition (SVD) [58].

2.2 Bistatic Radar

2.2.1 History and Applications

Some of the earliest experiments in radar were in fact of bistatic nature with spatial separation between the transmitter and the receiver[2]. Following early proposals that somewhere in the atmosphere may be of reflective nature to explain the propagation of radiowaves beyond the horizon, in 1924 and 1925, Appleton and Barnett conducted experiments to measure the height of the ionosphere with a set of broadcast transmitter and receivers located 120km apart on the south coast of England [72]. Then in the late 1930s, the development of the Chain Home radar system for detecting incoming aerial raids was motivated by the Daventry Experiment conducted in 1935 by Robert Watson Watt and Arnold Wilkins that proved feasible the radar detection of a Handley Page Heyford aircraft [73, 74]. In 1943, the Germans deployed Klein Heidelberg which was the first proper operational bistatic radar system used in World War II [75]. Further development of bistatic radar was then halted following research in radiowave interference and the development of monostatic radar [76].

In the 1950's, bistatic radar received new interest [77]. Its resurgence was evident in military applications such as semi-active missile seekers (Hawk and Sparrow in the United States and the Bloodhound in the UK) [78], bistatic fence radar (the Distant Early Warning line [79] and Navspasur in the US), detection of low-RCS objects [80]. During the 1970s and the early 1980s, a large-scale research programme was launched in the United States for development and research of bistatic radar systems for a variety of missions including Sanctuary for electronic counter-countermeasure, Bistatic Technology Transition/Tactical Bistatic Radar Demonstration for stealth operation and attack of fixed and moving ground targets, and Bistatic Alerting and Cueing [81].

Driven by the acceleration in computing power and the rise of the global positioning system (GPS), a new era began in the mid 1990s with significant developments in passive bistatic radar (PBR) and bistatic synthetic aperture radar (SAR) with their applications in remote sensing [82, 83, 84, 85, 86, 87, 88, 89], airborne surveillance [90, 91, 92, 93, 94], and stealth detection [95, 96, 97, 98, 99].

---

[2] It was only until World War II when the transmit-receive switch was invented.

Recently, in the wake of the new radio (NR) revolution and the integration of mobile communications with radar sensing, fresh interest was drawn into cooperative/collaborative/coherent bistatic radar (CBR) and PBR for automotive applications [100, 101, 102, 103]. The literature on this topic is rather limited due to its prematurity, so only a few exhibits that encompass the main developments are highlighted next. In [104], one of the early experiments to exploit long term evolution (LTE) signals for detecting moving vehicles in a PBR configuration using base-station transmitters as illuminators of opportunity (IOO)s. Then efforts shifted towards CBR for joint vehicular communication and detection using OFDM and PWCM signals with emphasis on their simplicity of implementation compared to the commonly used FMCW waveforms [105, 106, 107, 108, 109, 110, 111]. The common goal in these experiments is to demonstrate the ability of integrating radar capabilities of motion parameter estimation using existing mobile communication technologies and architectures. In [112], a proof of concept was presented in using satellite signals for automotive sensing.

It is evident from the summarised timeline that the development of the bistatic radar was influenced by different ventures with varying purposes. For this sake, an application-focused overview is presented next.

Bistatic DEW Line Gap-Filler Radar

The enthusiasm around distant early warning (DEW) radar during World War II was somehow generated by two potential advantages associated with a bistatic setup. The first being that targets carry a very large RCS when crossing the bistatic baseline, which is the line between the transmitter and the receiver. This occurs when the scattering angle tends to 0° leading to a forward-scatter cross section which can be many orders of magnitude larger than a typical monostatic (back-scatter) RCS [113]. The other potential advantage stems from the use of CW transmitters which are much simpler than monostatic pulse transmitters, and can therefore be rid of a modulator and can operate at low voltages. This meant that such systems required less maintenance and could be left unattended in areas of extreme weather conditions such as the arctic region or dessert land. Despite the Canadians investing considerable amount of effort into this application of bistatic radar for use in their air-defense line, they faced a problem of crossing birds leading to false detections and unwanted effects [97]. Also, the straight line assumption between the bistatic transmitter and receiver is limited to relatively short distances (due to the curvature of the Earth), so many systems had to be deployed to cover large perimeters. After various experiments in an attempt to resolve the unwanted effects of the bird crossing problem [114], such as lowering the operating frequency, the idea of using bistatic radar for DEW and gap-filling was eventually abandoned. It is important to mention that one limitation with forward-scatter detection is that it is impossible to determine where a target crosses the baseline of the transmitter and receiver pair whereas an equivalent monostatic radar can easily determine where the target crosses the radar fence. Also, a forward-scatter detection carries a zero Doppler frequency rendering it useless for separating moving targets from stationary ones.

Low Airborne Target Surveillance

One interesting property of bistatic radar is the ability to detect high-frequency (HF) signals propagating over-the-horizon (OTH), owing to the refraction paths through ionospheric layers. This allows surveillance of aerial targets such as low-altitude missiles and aircraft, as well as ballistic missiles during their boost phase. HF signals also travel along the curvature of the Earth through diffraction while suffering from higher path-loss and leading to reduced radar-to-target ranges. A bistatic radar would therefore exploit both operating modes for improved detection and surveillance. The 440-L system developed by the US in the 1960s and 1970s (halted in 1974) is a forward-scatter OTH radar that detects the targets' ionospheric signature formed by the disturbances caused by the ionized jet of gas trailing the rocket [115]. This would also allow detecting different types of missiles due to their unique OTH signature.

Planetary Exploration

The main interest in bistatic radar for space exploration originates from the fact that the pathloss limitation associated with the monostatic radar range equation can be overcome if the spacecraft could be used on the shorter of two transmit and receive paths. The idea is that a spacecraft orbiting a particular planet or moon can illuminate the latter with echoes being collected via terrestrial receiving stations. [97] concludes that bistatic radar cannot compete with the capabilities of monostatic SAR systems given the compelling goals and the willingness of funding agencies to provide the necessary resources.

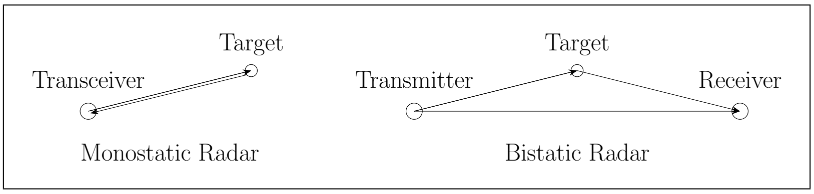

FIGURE 2.2: Monostatic vs bistatic radar setup

Air Surveillance

Typically operating in a passive mode, this class of bistatic radar, used in civilian or military air surveillance, relies on transmitters of opportunity which include terrestrial television (TV) and FM broadcast transmitters, satellite TV broadcasts, and HF radio broadcasts. These transmitters are of non-cooperative nature and the passive radar is a hitch-hiker operating without the knowledge of the transmitter. Multiple receivers could be deployed forming a multistatic measurement system. While most efforts in this area were experimental of nature and often dampened by the lack of interest against the rather accelerating developments in monostatic radar, the Silent Sentry system (developed by Lockheed Martin) [116], the multistatic high-definition (HD)-TV based radar system (developed by the US army) [117], and the FM radio-based bistatic radar system (developed by NATO) [118], represent real evidence of the ongoing interest, advancement, and application of bistatic and multistatic radar in the field of air surveillance.

2.2.2 Bistatic vs Monostatic: Advantages and Disadvantages

A bistatic radar configuration with separately located transmitter and receiver can offer numerous advantages over the monostatic counterpart. However, a comparable analysis is inherently dependant on the application being considered. In this section, a comparison is provided between the two configurations (see Figure 2.2 for a simple sketch of each configuration) where the advantages and disadvantages of each are highlighted. A brief summary of this comparison is provided in Table 2.2.

Due to the ability to combine the transmitter and the receiver in a compact package with both modules sharing a single antenna, the overall system design of a monostatic radar is relatively simple. Such co-location also simplifies calibration procedures, making it easier to maintain accuracy. Monostatic radar systems also require minimal infrastructure which reduces the associated logistical challenges owing to the single-platform integration. As a result, such systems are cost-effective and are suitable for mobile vehicles and platforms. From a performance perspective, owing to their high range resolution and low latency, they can provide tracking and surveillance with high accuracy. They can also be integrated with other sensors such as lidar, sonar, and cameras, for enhanced situational awareness. On the other hand, monostatic radar systems suffers from self-interference since the transmitted energy can leak directly to the receiver through internal coupling and are susceptible to clutter in dense environments. Active radiowave transmission, normally at fixed frequencies, makes these systems vulnerable to electronic jamming and easier to locate making them prone to direct destruction in warfare scenarios. They also typically have fixed antenna positions which limits the detection of low-flying or ground-hogging objects. The co-location of the transmitter and the receiver makes the network less scalable and results in hemispherical coverage which limits the range of the system.

TABLE 2.2: A summary of the advantages and disadvantages of monostatic and bistatic radar

	Monostatic	**Bistatic**
Advantages	• Simplicity of design [76] • Ease of calibration [34] • Low cost system [34] • Ease of deployment[34] • High tracking accuracy [119] • Improved range resolution [120] • Low latency [34] • Integration with other sensors [121]	• Enhanced stealth and LPI [122] • Resistance to ECM [123] • Flexible RCS [97] • Radar network scalability [124] • Improved target discrimination [97] • Reduced Doppler ambiguity [97]
Disadvantages	• Self-interference [125] • Susceptibility to clutter [97] • Limited detection of low-flying targets [97] • Vulnerability to jamming [97] • Limited scalability [126] • Limited range [97]	• Complex geometry and coordination [29] • Increased system cost [127] • Synchronisation challenges [128] • Complex signal processing [129] • Data fusion challenges [130, 131] • Complex coverage planning [127]

Bistatic radar has been a popular choice in military applications given its ability to operate covertly in the so-called low probability of intercept (LPI) systems. This stealth antenna increases their survivability and makes them less prone to jamming and other forms of electronic counter-measures (ECM). Due to their ability of illuminating targets from different angles as well as collecting forward-scatters, they can offer flexible and improved RCS which is also an attractive feature for defence applications. With separated transmitters and receivers, a bistatic radar can be scaled into a large network to achieve increased coverage, improved target separation, and reduced Doppler ambiguity. However, the said advantages are associated with multiple drawbacks in design, deployment, and operation. The bistatic geometry is inherently complex which makes the planning and coordination of the system architecture and coverage more difficult. Signal processing techniques are therefore more complex and require added stages for centralised data fusion. In order to maximise the information being extracted from the received signals, very tight synchronisation between the transmitter and the receiver is usually needed as well as good knowledge of the transmitted waves, which constitute the dilemma of bistatic radar operation. Overall, these challenges can massively increase the budget of using bistatic radar systems making them less attractive for low-cost applications.

2.2.3 The Synchronisation Requirement

In the architecture of a monostatic radar module, a sampling clock is used in the process of digitising the received signals. Time stamping, which is the essence of radar ranging as it is by-product of measuring time delays of reflected received signals, is crucial for proper operation of such systems. Fortunately, transceivers share the same sampling clock so the receiver has exact knowledge of the start of the transmission. However, due to the separation of the transmitter and the receiver in a bistatic system, accessing this information is not as straightforward and a form of communication between the nodes is required for useful measurement of a delay of a reflected signal. For this reason, synchronisation techniques have been studied and developed over the years. In [128], a variety of modern synchronisation techniques are discussed including coaxial links and optical fibre links when the nodes are within close proximity, line of sight (LOS) direct signal measurement, navigation satellites (e.g. GPS) using stable pulse-per-second (PPS) signals [132], and communication satellites using two-way measurements of PPS signals [133].

Timing is achieved in practice using two units: the oscillator and the counter [134]. These units combined form what is known as the clock. In order to synchronise two clocks, they both should be disciplined by the same source. Atomic clocks are known as the ultimate reference for disciplining any other local clocks. They are based on the vibration of atoms (Cesium or Rubidium). GPS satellites carry extremely precise atomic clocks hence their popular use for disciplining clocks in navigation and telecommunications. This is done through accurate positioning of ground receivers whose motion usually affects the level of the synchronisation achieved. Locally, Quartz-crystal oscillators are typically used and their output is compared to more accurate references for stricter timekeeping.

Providing an extensive review of synchronisation techniques and studies is beyond the scope of this work. Developments that are most relevant to bistatic radar applications are provided next. Without loss of generality, radar-based ranging requires sub-nanosecond time synchronisation which is dictated by the resolution requirement of these systems. In [135], a synchronisation scheme was developed using direct-path signals for bistatic SAR systems where the received signal is passed through an envelope detector to synchronise the sampling clock. In [136], synchronisation in a multistatic FMCW-based radar network is realised through a novel over-the-air deramping technique by utilising a reference synchronisation signal broadcasted on a lower frequency channel. In [137], a high-precision time synchronisation scheme is proposed for multistatic radar using a mix of microwave and troposcatter channels. It was shown that clock bias in the order of 2 ns can be achieved. [138] conducted a study determining the effects of L1 civilian signals on GPS timing for a fixed receiver. Nanosecond-accuracy time synchronisation was proved feasible by incorporating a weighting algorithm in the process. In [139], a novel synchronisation protocol was proposed for cooperative radar applications by combining information from all nodes in a shared ledger including coarse estimates of position (through global navigation satellite systems (GNSS)). This presented protocol enables sub-nanosecond level synchronisation between the nodes. [140] demonstrates the use of a fibre-optic White Rabbit network for accurate and stable time and frequency transfer in a netted radar system. Tests demonstrate that peak-to-peak synchronisation accuracy of sub-nanosecond can be achieved. More recently, a commercial off-the-shelf (COTS) oscillators were used in a study to evaluate the synchronisation capability using GPS disciplining in [141]. It was shown that time drift in the order of 4 ns can be achieved.

2.3 Summary

In this Chapter, a review of the literature around automotive and bistatic radar was presented. The basic concepts of radar use for localisation and motion parameter estimation were introduced. The FMCW signal was identified as the state-of-art waveform used for automotive radar applications. Fourier-based signal processing was acknowledged as the popular candidate for parameter estimation due to its efficiency and good performance. For more advanced signal processing techniques, subspace-based methods, namely MUSIC, were often used as the performance reference with sparse-based methods such as LASSO offering improved performance but with less theoretical exhibits due to the modernity of the framework. A gap between the narrowband and wideband problem was identified with little research being done to edge such gap and provide an effective solution to the wideband problem. The bulk of the literature on bistatic radar focused on its military use with very limited interest post cold war given its limitations and the superiority of the monostatic counterpart. However, it became more evident after reviewing the advantages of the bistatic configuration that what appealed to researches 70 years ago is rather timeless, and the versatility it offers can indeed help improve existing automotive radar sensing techniques as will be presented in the remaining Chapters.

Chapter 3

Enhanced Automotive Sensing Using Bistatic Radar with Narrowband Cooperative Roadside Sensors

3.1 Introduction

Radar-based sensing is a key enabling technology for autonomous driving and future intelligent transportation systems [9, 22, 142, 119, 143]. Recently, the automotive industry has benefited significantly from the development of various millimetre wave radar technologies deployed for applications such as adaptive cruise control, lane-change assistance, parking assistance, autonomous emergency brake, and advanced driver assistance systems (ADAS) [144, 145, 33]. Naturally, the focus of automotive radar has been on the monostatic mode, i.e. the radar is equipped with its own transmitters and receivers for effective target detection and estimation, given the simplicity of its implementation and signal processing. On the contrary, a bistatic radar relies on a transmitter typically located far away from the receiver, and requires an additional reference receiver for collecting a direct-path signal needed as a reference for the demodulation task [122, 146]. Without loss of generality, any form of communication between the transmitter and the receiver that allows instantaneous sharing of the modulation parameters of the transmitted waveform, as well as tight time synchronisation, is sufficient for the operation of such radar systems.

In this Chapter, an application of bistatic radar in an automotive scenario that incorporates cooperative roadside sensors is proposed. Consider a smart highway with some stationary roadside sensor transmitting radar

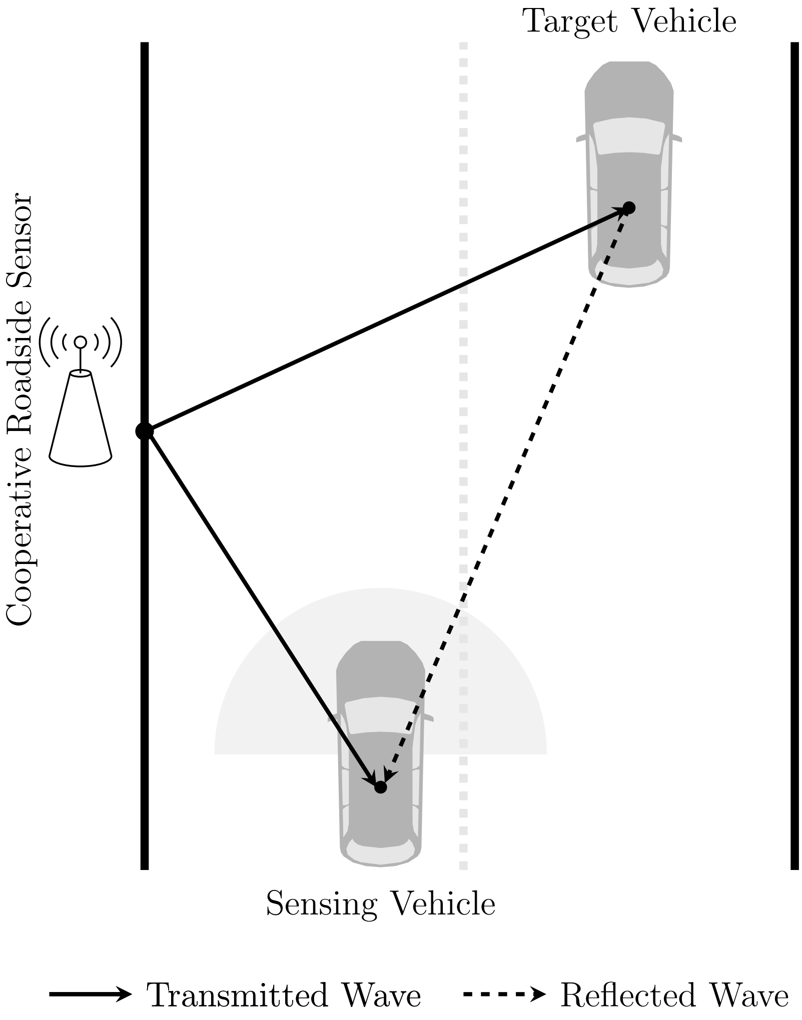

FIGURE 3.1: A schematic of the bistatic automotive localisation scenario.

waveforms, and a connected vehicle passively relying on these signals to locate other vehicles ahead of it in a bistatic manner. The idea is to relieve the vehicle from the transmission task, which inherently reduces power consumption. This also extends the detectable range of the vehicle's front long-range radar when the targets are closer to the roadside sensor than the receiving antenna. Figure 3.1 shows a schematic of such a scenario. Being of a cooperative nature, the roadside sensor transmits a modulated waveform suitable for radar applications – typically FMCW – and informs the sensing vehicle of its transmission routine and modulation parameters via a fifth-generation (5G) link with an agreed protocol. Although sharing such information is straightforward and can be achieved using vehicle-to-infrastructure (V2I) communications [108], meeting the synchronisation requirement can be a critical task. Briefly, this synchronisation task between the searching car and the roadside sensor can be achieved by fixing both local clock units to the same time reference, with an acceptable offset. It is important to mention, however, that in this proposed application, the synchronisation requirement, and the possible prospects to meeting them differ from that in bistatic vehicular applications exploiting 5G NR waveforms between multiple nodes (e.g. [147]). This adds another element of novelty to this work as emerging applications always drove specific synchronisation requirements [148]. Here, the following can be stated: the sensing vehicle can be synchronised by a local time reference present at the roadside sensor (no need for coordinated universal time (UTC) as a discipline); a clear LOS is available between the sensor and the vehicle; the latter can both have time reference units of the same granularity and specifications; the roadside sensor can quantify its clock drift due to its synchronisation to the GNSS atomic clock, and can communicate its drift to the vehicle after the initial synchronisation (as long as the drift does not exceed the latency of the communication link); the minimum accepted clock offset is dictated by the range resolution of bistatic FMCW radar and is independent from GNSS localisation accuracy and the instantaneous motion parameters of the vehicle; the sensing vehicle can have private access to GNSS, adding to DoFs available for the synchronisation task.

In the rest of this Chapter, the geometry of the proposed application alongside its solution is provided in Section 3.2. Then, the bistatic FMCW signal model is derived in Section 3.3. After that, a parameter estimation/processing algorithm based on FFT is proposed in Section 3.4. Finally, computer simulations are presented in Section 3.5, and conclusions are drawn in Section 3.6.

3.2 Solution to the Geometry of the Proposed Scenario[1]

Assume all vehicles are moving with constant forward velocity over the considered period of signal transmission such that the sensing vehicle is approaching the h-th roadside sensor and the target vehicles are driving away

---

[1] This work here is inpsired by Skolnik and Willis's development of the bistatic radar geometry for airborne applications and ballistic missile detection [76, 149]. The third dimension represented by the elevation is not taken into account here but will be considered in future work.

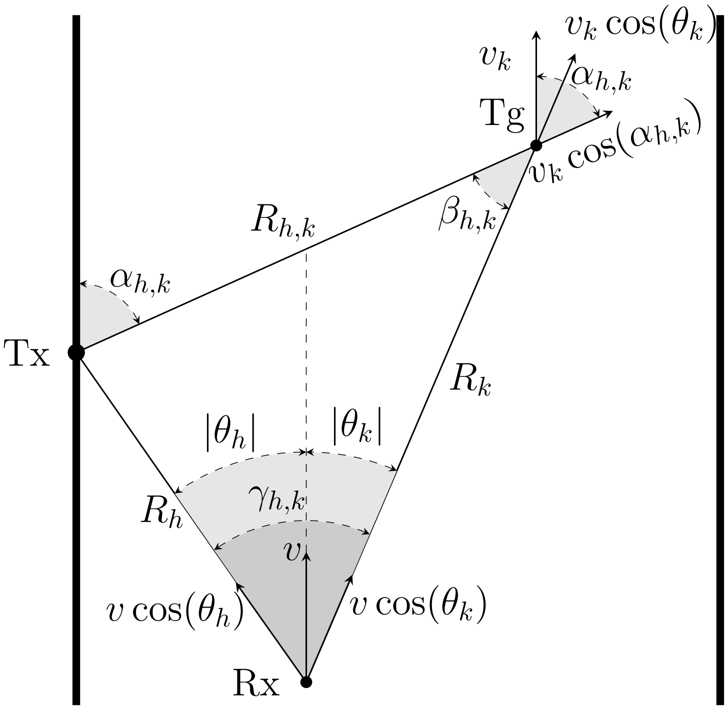

FIGURE 3.2: Geometry of the bistatic automotive localisation scenario.

from it. The aim for the sensing vehicle is to locate the k-th target by estimating its range R_k, forward velocity v_k, and DOA θ_k. Let R_h be the distance between the h-th roadside sensor and the sensing vehicle, which is often known as the bistatic baseline, and $R_{h,k}$ be the distance between the h-th roadside sensor and the k-th target vehicle. Denote by v the forward velocity of the sensing vehicle and θ_h the DOA of the h-th roadside sensor observed at the sensing vehicle. In the sequel, the subscripts k and h denote any parameters or signals corresponding to the k-th target and the h-th roadside sensor, respectively. The subscript h, k denotes any parameters or signals corresponding a combination of the k-th target and h-th roadside sensor.

The derivations presented in the remainder of this Section apply for the geometry provided in Figure 3.2 based on the assumption above that the target vehicle is driving away from the roadside sensor and the sensing vehicle is approaching it. This assumption does not particularly simplify the bistatic geometry in any sense, it rather allows focusing on the proof of concept for this proposed application since other geometries require different radar considerations, which may be considered in future work. Nonetheless, the derivations here are valid regardless of the placement of the sensing vehicle, the roadside sensor, or the target vehicle on either side of the road. So, applying the cosine law to the angle $\gamma_{h,k}$ in Figure 3.2 gives

$$R_{h,k}^2 = R_k^2 + R_h^2 - 2R_k R_h \cos(\gamma_{h,k}), \tag{3.1}$$

where $\gamma_{h,k}$ is an auxiliary angle and can be defined as

$$\gamma_{h,k} = |\theta_h - \theta_k|. \tag{3.2}$$

From Figure 3.1, the signal reflected from the k-th target and received at the sensing vehicle, travels a distance $\acute{R}_{h,k}$, known as the bistatic range, such that

$$\acute{R}_{h,k} = R_{h,k} + R_k. \tag{3.3}$$

Combining (3.1) and (3.3) leads to the following

$$R_k = \frac{\acute{R}_{h,k}^2 - R_h^2}{2\acute{R}_{h,k} - 2R_h \cos(\gamma_{h,k})}. \tag{3.4}$$

The velocity projected on the direct-path signal due to the motion of sensing vehicle can be defined as

$$v_h = v \cos(\theta_h). \tag{3.5}$$

Similarly, the total velocity projected on each path of the target signal can be defined as

$$\begin{aligned} v_{h,k} =& v_k \cos(\alpha_{h,k}) + (v_k - v)\cos(\theta_k) \\ =& v_k \left[\cos(\alpha_{h,k}) + \cos(\theta_k)\right] - v\cos(\theta_k), \end{aligned} \tag{3.6}$$

where $\alpha_{h,k}$ is an auxiliary angle and can be defined as

$$\alpha_{h,k} = \begin{cases} \beta_{h,k} + \theta_k, & \text{for} \quad \theta_h \leq 0^\circ, \\ \beta_{h,k} - \theta_k, & \text{for} \quad \theta_h \geq 0^\circ, \end{cases} \tag{3.7}$$

where $\beta_{h,k}$ is the bistatic angle. By applying the sine law to the bistatic triangle, we get

$$\frac{\sin(\gamma_{h,k})}{R_{h,k}} = \frac{\sin(\beta_{h,k})}{R_h}. \tag{3.8}$$

By combining (3.3), (3.7), and (3.8), we can rewrite $\alpha_{h,k}$ as

$$\alpha_{h,k} = \begin{cases} \arcsin\left(\frac{R_h}{R_{h,k}} \sin(|\theta_h - \theta_k|)\right) + \theta_k, & \text{for} \quad \theta_h \leq 0^\circ, \\ \arcsin\left(\frac{R_h}{R_{h,k}} \sin(|\theta_h - \theta_k|)\right) - \theta_k, & \text{for} \quad \theta_h \geq 0^\circ, \end{cases} \tag{3.9}$$

Using (3.6) and (3.9), v_k can be calculated as

$$v_k = \frac{v_{h,k} + v\cos(\theta_k)}{\cos(\alpha_{h,k}) + \cos(\theta_k)}. \tag{3.10}$$

To solve this geometry problem and estimate the motion parameters of the target, $\acute{R}_{h,k}$, R_h, $V_{h,k}$, v, θ_k, and θ_h should be known. Next, we show how the latter can be unambiguously estimated using radar sensing.

3.3 Bistatic Automotive FMCW Radar Signal Model

Suppose that the h-th roadside sensor transmits a frame of M identical narrowband FMCW chirps, with pulse repetition interval T and transmission duration per pulse equal to T_c. A single sensing vehicle is considered with K point targets present in the visible region of its radar module. A normalised single chirp can be represented in the complex form as

$$s_0(t) = \begin{cases} \exp\{j2\pi(f_0 t + 0.5\mu t^2)\} & t \in [0, T_c), \\ 0 & \text{otherwise}, \end{cases} \tag{3.11}$$

where f_0 denotes the starting frequency, t is the continuous real time, $\mu = \frac{B}{Tc}$ is the modulation rate, and B is the bandwidth. Note that the normalisation step to represent s_0 through dividing the original signal by the transmitted signal amplitude $\sqrt{P_t G_t}$ with P_t and G_t being the transmitted power and antenna gain, respectively, is merely done to simplify the notation. Then, the transmitted normalised frame can be represented as

$$s_M(t) = \sum_{m=0}^{M-1} s_0(t - mT). \tag{3.12}$$

Since the signal $s_M(t)$ is periodic, time t can be decomposed into fast time t_f and slow time mT such that

$$t = t_f + mT, \quad t_f \in [0, T_c). \tag{3.13}$$

Accordingly,

$$s_0(t) = s_0(t_f + mT) = s_0(t_f). \tag{3.14}$$

While $s_M(t)$ is a superposition of M chirps, it is convenient with the proposed decomposition of time to represent the normalised transmitted signal for the m-th chirp at time t_f as

$$s(m, t_f) = s_0(t_f). \tag{3.15}$$

The direct-path signal received at the sensing vehicle from the h-th roadside sensor incurs a time delay

$$\tau_h(m, t_f) = \frac{R_h}{c} - \frac{v_h}{c}(t_f + mT). \tag{3.16}$$

Suppose that the sensing vehicle is equipped with a ULA of L antennas with adjacent sensor spacing d [150]. By following a free-space path-loss model, the direct-path signal received at the l-th antenna of the sensing vehicle corresponds to the h-th roadside sensor and can be expressed as

$$r_h(l, m, t_f) = A_h s_0(t_f - \tau_h(m, t_f)) \exp\{-j2\pi\phi_h(l)\}, \tag{3.17}$$

where

$$A_h = \sqrt{\frac{P_t G_t G_r c^2}{(4\pi)^2 f_0^2 R_h^2}} \tag{3.18}$$

is the received signal amplitude with G_r being the receiver antenna gain, and

$$\phi_h(l) = \frac{f_0 d \sin\theta_h}{c} l \tag{3.19}$$

is the phase delay relative to the 0-th antenna.

Similarly, the signal reflected from the k-th target and received at the sensing vehicle incurs a time delay

$$\tau_{h,k}(m, t_f) = \frac{\acute{R}_{h,k}}{c} + \frac{v_{h,k}}{c}(t_f + mT). \tag{3.20}$$

Then, a bistatic signal reflected from the k-th target and received at the sensing vehicle can be expressed as

$$r_{h,k}(l, m, t_f) = A_{h,k} s_0(t_f - \tau_{h,k}(m, t_f)) \exp\{-j2\pi\phi_k(l)\}, \tag{3.21}$$

where

$$A_{h,k} = \sqrt{\frac{P_t G_t G_r \sigma_{\mathrm{bi}} c^2}{(4\pi)^3 f_0^2 R_k^2 R_{h,k}^2}} \tag{3.22}$$

is the received signal amplitude with σ_{bi} being the bistatic RCS, and

$$\phi_k(l) = \frac{f_0 d \sin\theta_k}{c} l \tag{3.23}$$

is the phase delay relative to the 0-th antenna. We assume, for the sake of simplicity, that σ_{bi} is constant and equal for all considered targets, and the received signal amplitude is deterministic.

The total signal received is a superposition of the direct-path and the bistatic target signals and can be expressed, in the presence of K targets, as

$$y_h(l,m,t_f) = r_h(l,m,t_f) + \sum_{k=1}^{K} r_{h,k}(l,m,t_f) + w_h(l,m,t_f), \tag{3.24}$$

where w_h is AWGN[2]. To extract the embedded information, y_h is cross-correlated with a signal identical to the one in (3.11) generated locally. Here, we assume perfect synchronisation and that the modulation settings are known. The resultant beat signal, also known as the intermediate frequency (IF) signal,

---

[2] Noise is not necessarily white Gaussian in real scenarios and the case with non-white non-Gaussian noise will be considered as part of future research since such considerations would affect the performance of the developed methods.

corresponding to the h-th sensor can be modelled as

$$
\begin{aligned}
&y_h^\circ(l,m,t_f) = r_h(l,m,t_f)s_0^*(t_f) + \sum_{k=1}^{K} r_{h,k}(l,m,t_f)s_0^*(t_f) + w_h(l,m,t_f) \\
&= A_h \exp\{j2\pi[f_0(t_f - \tau_h(m,t_f)) + 0.5\mu(t_f - \tau_h(m,t_f))^2 - \phi_h(l)]\} \\
&\quad \times \exp\{-j2\pi(f_0 t_f + 0.5\mu t_f^2)\} \\
&\quad + \sum_{k=1}^{K} A_{h,k} \exp\{j2\pi[f_0(t_f - \tau_{h,k}(m,t_f)) + 0.5\mu(t_f - \tau_{h,k}(m,t_f))^2 - \phi_k(l)]\} \\
&\quad \times \exp\{-j2\pi(f_0 t_f + 0.5\mu t_f^2)\} + w_h(l,m,t_f) \\
&= A_h \exp\{-j2\pi[f_0\tau_h(m,t_f) - 0.5\mu\tau_h^2(m,t_f) + \mu t_f \tau_h(m,t_f) + \phi_h(l)\} \\
&\quad + \sum_{k=1}^{K} A_{h,k} \exp\{-j2\pi[f_0\tau_{h,k}(m,t_f) - 0.5\mu\tau_{h,k}^2(m,t_f) + \mu t_f \tau_{h,k}(m,t_f) + \phi_k(l)]\} \\
&\quad + w_h(l,m,t_f) \\
&\approx A_h \exp\{-j2\pi[f_0\tau_h(m,t_f) + \mu t_f \tau_h(m,t_f) + \phi_h(l)]\} \\
&\quad + \sum_{k=1}^{K} A_{h,k} \exp\{-j2\pi[f_0\tau_{h,k}(m,t_f) + \mu t_f \tau_{h,k}(m,t_f) + \phi_k(l)]\} + w_h(l,m,t_f).
\end{aligned} \tag{3.25}
$$

By substituting (3.16) and (3.20) in (3.25) we get the dechirped signal as

$$
\begin{aligned}
&y_h^\circ(l,m,t_f) \\
&= A_h \exp\{-j2\pi[f_0(\frac{R_h}{c} + \frac{v_h}{c}(t_f + mT)) + \mu t_f(\frac{R_h}{c} + \frac{v_h}{c}(t_f + mT)) + \phi_h(l)]\} \\
&\quad + \sum_{k=1}^{K} A_{h,k} \exp\{-j2\pi[f_0(\frac{\acute{R}_{h,k}}{c} + \frac{v_{h,k}}{c}(t_f + mT)) + \mu t_f(\frac{\acute{R}_{h,k}}{c} + \frac{v_{h,k}}{c}(t_f + mT)) \\
&\qquad\qquad + \phi_k(l)]\} + w_h(l,m,t_f) \\
&\approx A_h \exp\{-j2\pi(\frac{f_0 R_h}{c} + \frac{\mu R_h}{c} t_f + \frac{f_0 v_h}{c} mT + \phi_h(l))\} \\
&\quad + \sum_{k=1}^{K} A_{h,k} \exp\{-j2\pi(\frac{f_0 \acute{R}_{h,k}}{c} + \frac{\mu \acute{R}_{h,k}}{c} t_f + \frac{f_0 v_{h,k}}{c} mT + \phi_k(l))\} + w_h(l,m,t_f).
\end{aligned} \tag{3.26}
$$

The dechirped signal is sampled at a rate f_s and can be written as a function of antenna index l, slow-time index m and fast-time index n as

$$\begin{aligned} \hat{y}_h[l,m,n] &= q_h \exp\{-j2\pi(\frac{\mu R_h}{c}\frac{n}{f_s} + \frac{f_0 v_h}{c} mT + \frac{f_0 d \sin\theta_h}{c} l)\} \\ &+ \sum_{k=1}^{K} q_{h,k} \exp\{-j2\pi(\frac{\mu \acute{R}_{h,k}}{c}\frac{n}{f_s} + \frac{f_0 v_{h,k}}{c} mT + \frac{f_0 d \sin\theta_k}{c} l)\} + \hat{w}_h[l,m,n], \end{aligned} \tag{3.27}$$

where $q_h = A_h e^{-j2\pi \frac{f_0 R_h}{c}}$, $q_{h,k} = A_{h,k} e^{-j2\pi \frac{f_0 \acute{R}_{h,k}}{c}}$, and $\hat{w}_h$ is AWGN.

Taking into account the Nyquist considerations, the maximum unambiguous bistatic range can be defined as

$$\mathcal{R}_{\text{bi}} = \frac{c f_s}{\mu}. \tag{3.28}$$

Assuming the observation period is equal to the chirp duration, the Rayleigh resolution of the target range can be defined as

$$\delta R_{h,k} = \frac{c}{2B\cos(\beta_{h,k}/2)}. \tag{3.29}$$

Assuming free-space propagation, using the radar range equation with the same radar settings, we can derive the relationship between the maximum detectable target range from a bistatic measurement, denoted by R_{bi}, and that from a monostatic measurement, denoted by R_{mono}, as

$$R_{\text{bi}} = \sqrt{\frac{\sigma_{\text{bi}}}{\sigma_{\text{mono}}} \frac{R_{\text{mono}}^2}{R_t}} \tag{3.30}$$

where σ_{mono} denotes the monostatic RCS, respectively, and R_t is the distance between the roadside sensor and the target. Assuming $\sigma_{\text{bi}} = \sigma_{\text{mono}}$, it is clear that the sensing vehicle can detect a target at much further distances using the proposed bistatic configuration when the target is closer to the roadside sensor. This is illustrated in Figure 3.3 where R_{mono} is set to 100 m, typically achieved by existing automotive monostatic radar for front long-range applications. Also, the roadside sensor can practically have much higher transmission power and antenna gain than the radar module fitted in the sensing vehicle, thereby potentially improving the detection range even further. It is worth mentioning that according to Crispin's equivalence RCS theorem [151], σ_{bi} and σ_{mono} vary over comparable values when $\beta_{h,k} < 180^\circ$, meaning

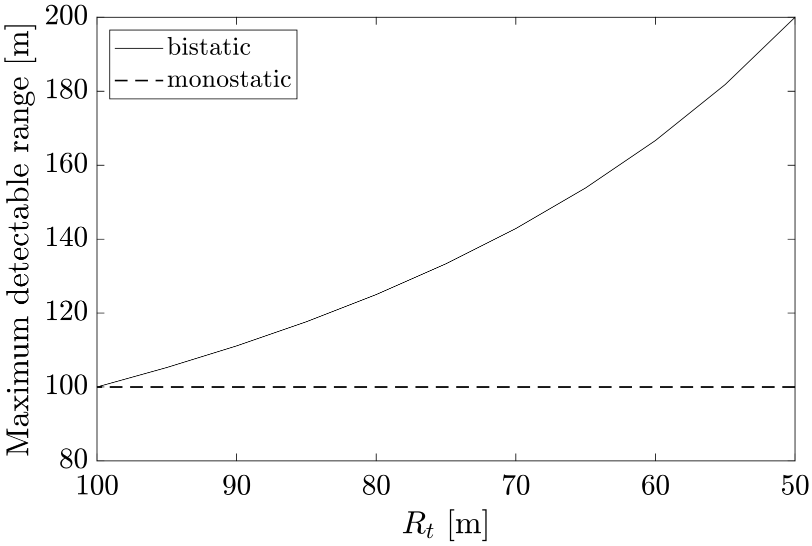

FIGURE 3.3: Maximum detectable range: bistatic vs monostatic (based on (3.30) with $R_{\text{mono}} = 100$ m and $\sigma_{\text{bi}} = \sigma_{\text{mono}}$).

that one could be greater than the other depending on the scattering geometry and conditions.

Let $\mathcal{R}_{\text{mono}}$ be the maximum unambiguous monostatic range. Knowing that $\mathcal{R}_{\text{mono}} = \frac{cf_s}{2\mu}$, we can define the following

$$\mathcal{R}_{\text{bi}} = 2\mathcal{R}_{\text{mono}} - R_t. \tag{3.31}$$

From (3.31), we can see that the maximum unambiguous range of the proposed application is at least that of a monostatic radar and at most twice of it. In theory, this permits relaxing the sampling-clock requirements which can reduce the energy cost. However, setting the sampling frequency to achieve the lower bound would be a more practical approach. From (3.29), we can see that the resolution of the proposed application is poorer than that of a monostatic radar (typically $c/(2B)$). However, the proposed scenario offers other advantages depending on the instantaneous geometry of vehicles. For instance, when two cars have the same monostatic range but different bistatic range, they can still be separated here while monostatic radar fails. In addition, extending this proposal to deploying multiple roadside sensors with well-designed cooperative transmission protocols could improve range resolution beyond the monostatic radar capabilities.

In the dechirp process, it was assumed that perfect synchronisation between the sensing vehicle and the roadside sensor is achieved. However, synchronisation errors may occur in reality, so we define here the minimum requirement of time synchronisation for acceptable errors in parameter estimation. Let the synchronisation error be τ_e (in seconds), assumed constant during one frame. The range bias introduced can then be expressed as

$$R_{bias} = \pm \tau_e c. \tag{3.32}$$

This bias in range measurement can be considered negligible if it is smaller than half of the resolution bound. So, using (3.29), for a given bandwidth B, the maximum accepted clock offset in this proposed application is related to the bistatic angle $\beta_{h,k}$ can be defined as

$$\tau_{e,\max} = \min_{\beta_{h,k}} \left(\frac{1}{4B\cos(\beta_{h,k}/2)} \right). \tag{3.33}$$

3.4 Data Processing and Parameter Estimation

The raw data is structured into a matrix format, and then 2D FFT is applied for range-Doppler and range-DOA processing.

3.4.1 Range-Doppler Estimation

From the sampled data in (3.27) corresponding to the h-th roadside sensor, the slow-time and fast-time domains are considered and can be structured into a 2D matrix $\mathbf{Y}_{\boldsymbol{RV},h} \in \mathbb{C}^{M \times N}$ as

$$\mathbf{Y}_{\boldsymbol{RV},h} = q_h \cdot \mathbf{v}_h \cdot \mathbf{r}_h^T + \sum_{k=1}^{K} q_{h,k} \cdot \mathbf{v}_{h,k} \cdot \mathbf{r}_{h,k}^T + \mathbf{W}_{\boldsymbol{RV},h}, \tag{3.34}$$

where $\mathbf{r}_h$ and $\mathbf{r}_{h,k}$ are $N \times 1$ column vectors

$$\mathbf{r}_h = \left[1, e^{-j2\pi \frac{\mu R_h}{c} \frac{1}{f_s}}, \ldots, e^{-j2\pi \frac{\mu R_h}{c} \frac{N-1}{f_s}} \right]^T, \tag{3.35}$$

$$\mathbf{r}_{h,k} = \left[1, e^{-j2\pi \frac{\mu \acute{R}_{h,k}}{c} \frac{1}{f_s}}, \ldots, e^{-j2\pi \frac{\mu \acute{R}_{h,k}}{c} \frac{N-1}{f_s}} \right]^T, \tag{3.36}$$

representing the range steering vectors, $\mathbf{v}_h$ and $\mathbf{v}_{h,k}$ are $M \times 1$ column vectors

$$\mathbf{v}_h = \left[1, e^{-j2\pi \frac{f_0 v_h}{c} T}, \ldots, e^{-j2\pi \frac{f_0 v_h}{c} (M-1)T} \right]^T, \tag{3.37}$$

$$\mathbf{v}_{h,k} = \left[1, e^{-j2\pi \frac{f_0 v_{h,k}}{c} T}, \ldots, e^{-j2\pi \frac{f_0 v_{h,k}}{c} (M-1)T} \right]^T, \tag{3.38}$$

representing the Doppler steering vectors, and $\mathbf{W}_{\boldsymbol{RV},h}$ is AWGN.

Computing the range-Doppler 2D FFT allows us to estimate the peaks corresponding to (R_h, V_h) and $(\acute{R}_{h,k}, v_{h,k})$. By applying the triangle inequality to Tx-Tg-Rx in Figure 3.2, we can state that $\acute{R}_{h,k} = (R_{h,k} + R_k) < R_h$ (assuming no reflections from objects on the LOS between the sensing vehicle and the roadside sensor). Therefore, the peak with the smallest range corresponds to (R_h, v_h), while the remaining peak corresponds to $(\acute{R}_{h,k}, v_{h,k})$.

3.4.2 Range-DOA Estimation

Next, the antenna and fast-time domains are considered and can be structured into a 2D matrix $\mathbf{Y}_{\boldsymbol{R\theta},h} \in \mathbb{C}^{L\times N}$ as

$$\mathbf{Y}_{\boldsymbol{R\theta},h} = q_h \cdot \mathbf{a}_h \cdot \mathbf{r}_h^T + \sum_{k=1}^{K} q_{h,k} \cdot \mathbf{a}_k \cdot \mathbf{r}_{h,k}^T + \mathbf{W}_{\boldsymbol{R\theta},h}, \tag{3.39}$$

where $\mathbf{a}_h$ and $\mathbf{a}_k$ are $L \times 1$ column vectors

$$\mathbf{a}_h = \left[1, e^{-j2\pi \frac{f_0 d \sin\theta_h}{c}}, \ldots, e^{-j2\pi \frac{f_0 d \sin\theta_h}{c}(L-1)}\right]^T, \tag{3.40}$$

$$\mathbf{a}_k = \left[1, e^{-j2\pi \frac{f_0 d \sin\theta_k}{c}}, \ldots, e^{-j2\pi \frac{f_0 d \sin\theta_k}{c}(L-1)}\right]^T, \tag{3.41}$$

representing the array steering vectors, and $\mathbf{W}_{\boldsymbol{R\theta},h}$ is AWGN.

Computing the range-DOA 2D FFT allows us to estimate the peaks corresponding to (R_h, θ_h) and $(\acute{R}_{h,k}, \theta_k)$ which can be matched directly to the corresponding range parameters previously estimated. The estimated parameters are then stored and processed as shown in Algorithm 1.

3.5 Simulation Results

Computer simulations were conducted to evaluate the success of the proposed application[3]. A single cooperative roadside sensor, sensing vehicle, and target are placed at map coordinates to replicate the road scenario of

---

[3] The developed methods and algorithms can be verified effectively using simulated data as the model is accurate enough for reliable validation, which is also a common practice in the radar community. However it is always advantageous and desirable to test the methods and algorithms using real data. Given the difficulty of obtaining real data, it is left for future work.

Algorithm 1 FFT-based parameter estimation algorithm for the proposed bistatic automotive sensing application.

```
Require: $\mathbf{Y}_{\boldsymbol{RV},h}$, $\mathbf{Y}_{\boldsymbol{R\theta},h}$, $f_0$, $\mu$, $d$, $T$, $M$, $L$, $f_s$, $N$.
Apply 2D FFT to $\mathbf{Y}_{\boldsymbol{RV},h}$; compute a range-Doppler map.
Search for the peaks in the range-Doppler map; estimate $R_h$, $v_h$, $\acute{R}_{h,k}$, and $v_{h,k}$.
Apply 2D FFT to $\mathbf{Y}_{\boldsymbol{R\theta},h}$; compute a range-DOA map.
Search for the peaks in the range-DOA map; estimate $\theta_h$ and $\theta_k$.
Using the estimates of $\theta_h$ and $\theta_k$, estimate $\gamma_{h,k}$ according to (3.2).
Using the estimates of $\gamma_{h,k}$, $R_h$ and $\acute{R}_{h,k}$, estimate $R_k$ according to (3.4).
Using the estimates of $v_h$ and $\theta_h$, estimate $v$ according to (3.5).
Using the estimates of $\acute{R}_{h,k}$, $R_k$, $R_h$, $\theta_h$, and $\gamma_{h,k}$, estimate $\alpha_{h,k}$ according to (3.7).
Using the estimates of $v_{h,k}$, $v$, $\theta_k$, and $\alpha_{h,k}$, estimate $v_k$ according to (3.10).
return Estimates of $R_k$, $v_k$ ,and $\theta_k$ for all $K$ targets.
```

TABLE 3.1: Radar settings used in the simulation of the proposed bistatic automotive application

Parameter	Value	Parameter	Value
P_t	10 dBm	f_0	77 GHz
G_t	23 dBi	B	300 MHz
G_r	16 dBi	T_c	30 μs
σ_{bi}	1 dBsm	T	35 μs
NF	12 dB	f_s	17.07 MHz
M	256	N	512
L	128	d	1.948 mm

Figure 3.1. The radar system settings used are recommended by the International Telecommunication Union (ITU) for automotive applications in [152]. A summary of these settings used as well as the modulation parameters is provided in Table 3.1. In the first simulation, the noise figure (NF) was fixed at 12 dB (recommended in [152] for measuring a monostatic range up to 100 m). The estimated parameters after applying Algorithm 1 are shown in Table 3.2. We can see that at the recommended NF of 12 dB, the motion parameters can be accurately estimated with the proposed bistatic measurement.

Monte Carlo simulations were also conducted to compute the root-mean-squared error (RMSE) performance at different levels of noise. A scenario where the sensing vehicle is equipped with an equivalent monostatic radar is used as the baseline for comparison. NF is varied in a range of 10-30 dB,

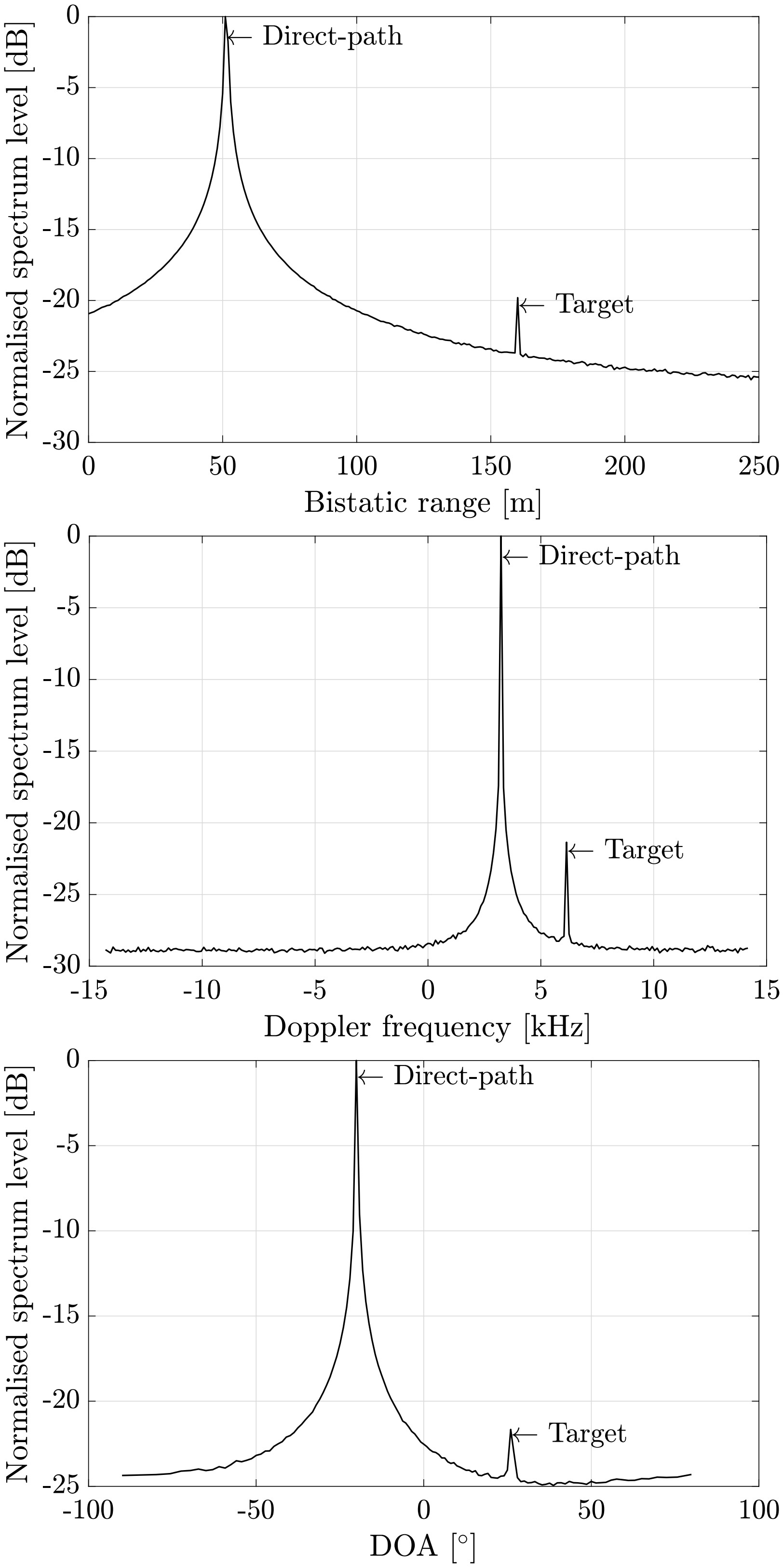

FIGURE 3.4: An example of the range, Doppler, and DOA spectra generated using FFT from bistatic measurements for estimating the parameters in Table 3.2.

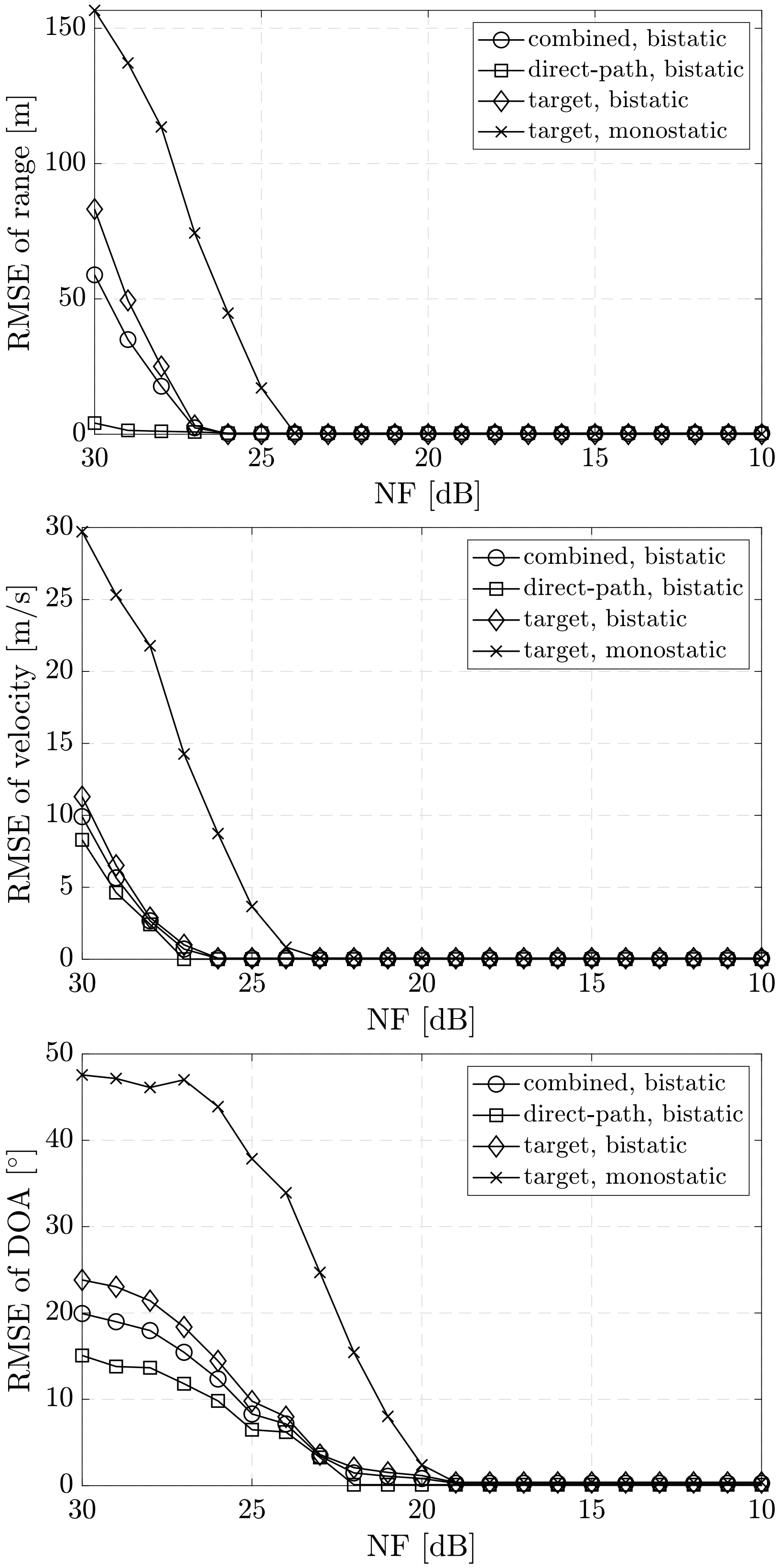

FIGURE 3.5: A comparison of RMSE between the proposed bistatic automotive radar application and the monostatic equivalent against different levels of NF ($\sigma_{\text{bi}} = \sigma_{\text{mono}}$).

TABLE 3.2: True vs estimated parameters from bistatic measurements (NF = 12 dB)

Parameter	R_h [m]	R_k [m]	v [m/s]	v_k [m/s]	θ_h [°]	θ_k [°]
True	51.41	92.24	13.41	25.64	-20	26.31
Estimated	51.01	92.30	13.42	25.57	-20.10	25.94

and 2000 tests are run for each level of noise. Then, the RMSE for the estimated range, velocity and DOA is computed, and the results are shown in Figure. 3.5. These results show that with the proposed bistatic configuration the motion parameters, for both direct-path and target signals, can be accurately estimated as NF approaches the recommended levels. As theoretically expected, the bistatic measurement outperforms the monostatic counterpart when estimating the target signal. By focusing on the estimation performance of the target signals in Figure 3.5, it is clear that bistatic measurements achieve the same level as the monostatic ones but with 3 dB increase in noise levels. Also, while the direct-path signal dominates the FFT spectrum, a simple peak search was sufficient to detect the relatively weaker target signal.

3.6 Summary

In this Chapter, an automotive application for bistatic radar was proposed by employing cooperative roadside sensors. As well as enahancing the detection range of the vehicle with the bistatic mode achieving a theoretical range up to twice that of the monostatic counterpart, this application can also reduce the power cost associated with the constant transmission while in autopilot mode. Moreover, the roadside sensors can offer more flexibility of transmission with increased antennas, higher power, and better orthogonality. With less active transmitters on the smart highway, assuming more user vehicles than roadside sensors, the spectrum may be much cleaner than that with monostic radars actively illuminating the field. Although perfect synchronisation between the transmitting sensor and the receiving car is a critical task, this Chapter focused on the radar signal processing aspect and derived the general geometry of a scenario when the sensing vehicle is approaching the roadside sensor while the target drives away from it. It was shown that the motion parameters can be unambiguously estimated when the sensing vehicle is equipped with an antenna array in the receiving mode.

Computer simulations have shown that the proposed application outperforms the monostatic equivalent in considered scenarios and it can match its performance with 3 dB higher noise levels. It is important to mention that more advanced peak search algorithms and direct-path suppression techniques, such as CFAR [153], could yield a better RMSE at higher noise levels. However, such research direction remains for future work. In the next Chapter, alternative signal processing techniques for improving the estimation quality are explored.

Chapter 4

Sparsity-Based Location and Doppler Estimation

4.1 Introduction

While it is generally accepted that advanced signal processing techniques carry the extra computational cost, this consensus is destined to vanish as processing power retains its increasing trend. As a result, advanced signal processing techniques such as MUSIC [47] and sparsity-based methods under the CS framework [154] have been hot topics in radar-related research in the last few decades [49, 40, 61, 33]. A sparse representation means that the signal can be modelled as a vector of finite/infinite parameters where only a few entries are non-zero; a set containing the indices of the non-zero entries in this sparse vector is known as the support.

When a radar system illuminates a given area of interest, the reflected energy only occupies a small fraction of the detected spectrum. Although conventional radar signal processing does not assume sparsity in its framework, recent work [61] has shown that tools used in the CS area [55] can in fact be exploited for high resolution radar imaging. In [155], the effects of the radar settings on the conditions required for sparse signal recovery in a convex envinronment were studied. It was also shown that correct detection of targets depends on their number and the SNR level of the signals available. For convenience, sparsity is assumed in this thesis (may be achieved in a preprocessing stage such as CFAR) in order to focus on validating the bistatic automotive radar application being presented.

To the best of our knowledge, in the existing literature on motion parameter estimation using sparse recovery techniques, no work has previously been done on jointly estimating range, Doppler, and DOA of a target using sparse representation of bistatic measurements. Here, a sparse representation is derived for the bistatic automotive signal model presented in Section 3.3 for joint location and Doppler estimation[1]. Without loss of generality, the 2D-location is defined as the range and DOA of the target, and Doppler is the effect of the moving object on the path of the propagating wave, which is directly related to the target velocity. The Cramer-Rao bound (CRB) is also derived for this estimation problem for the first time. It provides a lower bound on the variance of an unbiased estimation of the motion parameters [156], which is a performance benchmark commonly used in the radar literature. In the CRB derivation, the noiseless signal is treated as deterministic with its noisy version following a Gaussian distribution. A closed-form representation is provided that allows straightforward implementation with simulation tools.

In the rest of this Chapter, a 3D bistatic automotive FMCW signal model and the CRB are derived in Section 4.2. Then, a multi-target sparsity-based method for simultaneous location and Doppler estimation is proposed in Section 4.3. Finally, simulation results are presented in Section 4.4, and the findings are summarised in Section 4.5.

4.2 3D Bistatic Automotive FMCW Radar Signal Model

Without loss of generality, we assume perfect synchronisation with the modulation settings already known. Further, we assume that the location of the roadside sensor (R_h, θ_h) is known and that the signal r_h has already been removed at the receiver. Note that knowledge of the roadside sensor location allows us to more effectively remove the direct-path signal as explained below:

1. The peak corresponding to the direct-path signal can be unambiguously identified since $\tau_h < \tau_{h,k}$ (triangle inequality in Figure 3.2 with $R_h < (R_{h,k} + R_k)$) and the intensity of the peak is strictly higher than the ones corresponding to bistatic reflections.

---

[1] While this thesis adopts a sparsity-based approach for parameter estimation, the focus remains on devising a signal processing scheme for the proposed bistatic automotive radar application in which it outperforms the currently used FFT-based approach in the industry. The core optimisation method used here, LASSO, is a popular and well understood algorithm. Novel methods for sparsity-based estimation may be considered in future work.

2. The GPS coordinates of the roadside sensor can be accessed by the sensing vehicle through the established NR communication link. With access to its own GPS coordinates, the sensing vehicle can then implement data fusion to better estimate the direct-path signal (Note that the availability of accurate GPS coordinates is not necessary for the feasibility of this application but can help optimise the estimation and the removal of the direct-path signals).

3. Direct-path removal techniques have been studied extensively in the literature, and the feasibility of such task has already been proven [157, 158, 159]. Moreover, having access to two sources of information related to the direct-path signal (through radar processing and NR communications) can intuitively improve the performance of those techniques.

The dechirped and sampled signal in (3.27) can now be simplified to represent the target reflections only. So, it can be written as a function of antenna index l, slow-time index m and fast-time index n as

$$\check{y}_h[l,m,n] = \sum_{k=1}^{K} q_{h,k} e^{-j2\pi(\frac{\mu \acute{R}_{h,k}}{c}\frac{n}{f_s} + \frac{f_0 v_{h,k}}{c} mT + \frac{f_0 d \sin\theta_k}{c} l)} + \hat{w}_h[l,m,n]. \tag{4.1}$$

The results in (4.1) can be structured to form a tensor $\boldsymbol{\mathcal{Y}}_h \in \mathbb{C}^{L\times M\times N}$ such that

$$\boldsymbol{\mathcal{Y}}_h = \sum_{k=1}^{K} q_{h,k}(\mathbf{a}_k \circ \mathbf{v}_{h,k} \circ \mathbf{r}_{h,k}) + \boldsymbol{\mathcal{W}}_h, \tag{4.2}$$

where $\boldsymbol{\mathcal{W}}_h \in \mathbb{C}^{L\times M\times N}$ is the AWGN tensor. Next, the antenna and fast-time domains are stacked together against the slow time, and the tensor $\boldsymbol{\mathcal{Y}}_h$ can be reshaped into a matrix $\mathbf{Y}_h \in \mathbb{C}^{LN\times M}$ such that

$$\mathbf{Y}_h = \sum_{k=1}^{K} q_{h,k}\left(\mathbf{p}_{h,k}\mathbf{v}_{h,k}^T\right) + \mathbf{W}_h, \tag{4.3}$$

where $\mathbf{p}_{h,k} = \mathbf{r}_{h,k} \otimes \mathbf{a}_k$ and $\mathbf{W}_h \in \mathbb{C}^{LN\times M}$ is the AWGN matrix.

Finally, $\mathbf{Y}_h$ can be written in a more compact format as

$$\mathbf{Y}_h = \mathbf{P}_h \mathbf{X}_h \mathbf{V}_h^T + \mathbf{W}_h, \tag{4.4}$$

where $\mathbf{P}_h = [\mathbf{p}_{h,1}, \mathbf{p}_{h,2}, \dots, \mathbf{p}_{h,K}] \in \mathbb{C}^{LN\times K}$ contains the range-DOA information, $\mathbf{V}_h = [\mathbf{v}_{h,1}, \mathbf{v}_{h,2}, \dots, \mathbf{v}_{h,K}] \in \mathbb{C}^{M\times K}$ contains the Doppler information, and $\mathbf{X}_h = \mathrm{diag}\{q_{h,1}, q_{h,2}, \dots, q_{h,K}\} \in \mathbb{C}^{K\times K}$ contains the complex amplitude.

4.2.1 CRB Derivation for 3D Joint Parameter Estimation

Consider the following reformulation of (4.4)

$$\mathbf{y}_h = \text{vec}\{\mathbf{Y}_h\} = \mathbf{A}_h \mathbf{x}_h + \mathbf{w}_h \in \mathbb{C}^{LMN \times 1}, \tag{4.5}$$

where

$$\mathbf{A}_h = [(\mathbf{v}_{h,1} \otimes \mathbf{p}_{h,1}), (\mathbf{v}_{h,2} \otimes \mathbf{p}_{h,2}), \ldots, (\mathbf{v}_{h,K} \otimes \mathbf{p}_{h,K})] \in \mathbb{C}^{LMN \times K}, \tag{4.6}$$

$$\mathbf{x}_h = [q_{h,1}, q_{h,2}, \ldots, q_{h,K}]^T \in \mathbb{C}^{K \times 1}, \tag{4.7}$$

and $\mathbf{w}_h = \text{vec}\{\mathbf{W}_h\}$.

For the simplicity of notation, we assume a single target and roadside sensor, so the subscripts h and k are omitted in the following CRB derivation, and the bistatic range and velocity, and DOA are now denoted as R, v, and θ, respectively. Let $\mathbf{Q_n} \in \mathbb{C}^{LMN \times 1}$ be the noise covariance matrix of $\mathbf{y}$, which can be expressed as

$$\mathbf{Q_n} = \text{E}\{\mathbf{w}\mathbf{w}^H\} = \sigma_n^2 \mathbf{I}, \tag{4.8}$$

where σ_n^2 is the noise power, $\mathbf{I}$ is an $LMN \times LMN$ identity matrix, and $\text{E}\{.\}$ is the expectation computation. The estimation of the motion parameters is denoted as $\mathbf{u}$ such that

$$\mathbf{u} = [R\ \theta\ v]^T. \tag{4.9}$$

Then, the measurement vector follows a Gaussian distribution, i.e. $\mathbf{y} \sim \mathcal{N}(\boldsymbol{\mu}_\mathbf{y}(\mathbf{u}), \sigma_n^2 \mathbf{I})$, where $\boldsymbol{\mu}_\mathbf{y}(\mathbf{u})$ represents the mean value of $\mathbf{y}$ and is defined as

$$\boldsymbol{\mu}_\mathbf{y}(\mathbf{u}) = \boldsymbol{\mu}_\mathbf{y}(\theta, R, v) = A\mathbf{a}(\theta, R, v), \tag{4.10}$$

with the $(mLN + lN + n)$-th entry of $\mathbf{a}(\theta, R, v)$ given by

$$a_{m,l,n}(\theta, R, v) = \exp\left\{-j2\pi\left(\frac{f_0 d \sin\theta}{c} l + \frac{\mu R}{c}\frac{n}{f_s} + \frac{f_0 v}{c} mT\right)\right\}, \tag{4.11}$$

and A is the signal amplitude. Accordingly, the probability density function (PDF) of $\mathbf{y}$ is

$$p(\mathbf{y}, \mathbf{u}) = \frac{1}{\pi^{LMN} \det\{\mathbf{Q_n}\}} e^{-(\mathbf{y} - \boldsymbol{\mu}_\mathbf{y}(\mathbf{u}))\mathbf{Q_n}^{-1}(\mathbf{y} - \boldsymbol{\mu}_\mathbf{y}(\mathbf{u}))^H}, \tag{4.12}$$

where det{.} returns the matrix determinant. The log-likelihood function of **y** is given by

$$\mathcal{L}_{\mathbf{y}}(\mathbf{u}) \triangleq \ln p(\mathbf{y},\mathbf{u}) = -LMN \ln \det\{\pi \mathbf{Q_n}\} - (\mathbf{y} - \boldsymbol{\mu}_y(\mathbf{u}))\mathbf{Q_n}^{-1}(\mathbf{y} - \boldsymbol{\mu}_y(\mathbf{u}))^H. \tag{4.13}$$

Let $\hat{\mathbf{u}}$ be the unbiased estimation for the parameter set **u**. The CRB gives the lower bound of the variance of such estimation, whose covariance matrix is given as

$$\mathbf{C}(\mathbf{u}) \triangleq \mathrm{E}\{(\hat{\mathbf{u}} - \mathbf{u})(\hat{\mathbf{u}} - \mathbf{u})^T\} \tag{4.14}$$

and satisfies the following inequality

$$\mathbf{C}(\mathbf{u}) \geq \mathbf{J}^{-1}, \tag{4.15}$$

where **J** is the Fisher information matrix (FIM) and defined as

$$\mathbf{J} = -\mathrm{E}\left\{\nabla_{\mathbf{u}}\nabla_{\mathbf{u}}^T \mathcal{L}_{\mathbf{y}}(\mathbf{u})\right\}, \tag{4.16}$$

and $\nabla_{\mathbf{u}} = \left[\frac{\partial}{\partial R}\ \frac{\partial}{\partial \theta}\ \frac{\partial}{\partial v}\right]^T$. Then for a Gaussian distribution and a deterministic mean, the i,j-th element of the FIM can be written as [43]

$$J_{i,j} = \frac{\partial^2}{\partial u_i \partial u_j}[\mathcal{L}_{\mathbf{y}}(\mathbf{u})] = 2\Re\left\{\frac{\partial \boldsymbol{\mu}_y^H(\mathbf{u})}{\partial u_i}\mathbf{Q_n}^{-1}\frac{\partial \boldsymbol{\mu}_y(\mathbf{u})}{\partial u_j}\right\}, \tag{4.17}$$

where i and j represent the rows and columns in **J** and u_i represents the i-th parameter in **u**. For jointly estimating the R, θ, and v, the FIM is expressed as

$$\mathbf{J} = \begin{bmatrix} J_{\theta\theta} & J_{\theta R} & J_{\theta v} \\ J_{R\theta} & J_{RR} & J_{Rv} \\ J_{v\theta} & J_{vR} & J_{vv} \end{bmatrix}. \tag{4.18}$$

Next, the FIM element with respect to θ is derived as

$$J_{1,1} = \frac{\partial^2}{\partial \theta^2}[\mathcal{L}_{\mathbf{y}}(\mathbf{u})] = 2\frac{A^2}{\sigma_n^2}\frac{\partial \mathbf{a}^H(\theta,R,v)}{\partial \theta}\frac{\partial \mathbf{a}(\theta,R,v)}{\partial \theta}. \tag{4.19}$$

Firstly, the derivative of $a_{m,l,n}(\theta,R,v)$ with respect to θ can be obtained as

$$\frac{\partial a_{m,l,n}(\theta,R,v)}{\partial \theta} = a_{m,l,n}(\theta,R,v)\left(-j2\pi\frac{f_0 d\cos\theta}{c}l\right). \tag{4.20}$$

Then,

$$\frac{\partial \mathbf{a}(\theta,R,v)}{\partial \theta} = \mathbf{a}(\theta,R,v) \odot (\mathbf{1_M} \otimes (\mathbf{1_N} \otimes \acute{\mathbf{a}}(\theta))), \tag{4.21}$$

where $\acute{\mathbf{a}}(\theta) = [0, -j2\pi\frac{f_0 d\cos\theta}{c}, \dots, -j2\pi\frac{f_0 d\cos\theta}{c}(L-1)]^T, \mathbf{1_M} = [1,1,\dots,1]^T \in \mathbb{R}^{M\times 1}$, and $\mathbf{1_N} = [1,1,\dots,1]^T \in \mathbb{R}^{N\times 1}$. After that, we get $J_{\theta,\theta} = J_{1,1}$.

Similarly, the FIM element with respect to R is derived as

$$J_{2,2} = \frac{\partial^2}{\partial R^2}[\mathcal{L}_{\mathbf{y}}(\mathbf{u})] = 2\frac{A^2}{\sigma_n^2}\frac{\partial \mathbf{a}^H(\theta,R,v)}{\partial R}\frac{\partial \mathbf{a}(\theta,R,v)}{\partial R}. \tag{4.22}$$

For the derivative of $a_{m,l,n}(\theta,R,v)$ with respect to R, we get

$$\frac{\partial a_{m,l,n}(\theta,R,v)}{\partial R} = a_{m,l,n}(\theta,R,v)\left(-j2\pi\frac{\mu}{c}\frac{n}{f_s}\right). \tag{4.23}$$

Then,

$$\frac{\partial \mathbf{a}(\theta,R,v)}{\partial R} = \mathbf{a}(\theta,R,v) \odot (\mathbf{1_M} \otimes (\acute{\mathbf{r}} \otimes \mathbf{1_L})), \tag{4.24}$$

where $\acute{\mathbf{r}} = [0, -j2\pi\frac{\mu}{cf_s}, \dots, -j2\pi\frac{\mu}{cf_s}(N-1)]^T$ and $\mathbf{1_L} = [1,1,\dots,1]^T \in \mathbb{R}^{L\times 1}$. After that, we get $J_{R,R} = J_{2,2}$.

Next, the FIM element with respect to v is derived as

$$J_{3,3} = \frac{\partial^2}{\partial v^2}[\mathcal{L}_{\mathbf{y}}(\mathbf{u})] = 2\frac{A^2}{\sigma_n^2}\frac{\partial \mathbf{a}^H(\theta,R,v)}{\partial v}\frac{\partial \mathbf{a}(\theta,R,v)}{\partial v}. \tag{4.25}$$

For the derivative of $a_{m,l,n}(\theta,R,v)$ with respect to v, we get

$$\frac{\partial a_{m,l,n}(\theta,R,v)}{\partial v} = a_{m,l,n}(\theta,R,v)\left(-j2\pi\frac{f_0 T}{c}m\right). \tag{4.26}$$

Then,

$$\frac{\partial \mathbf{a}(\theta,R,v)}{\partial V} = \mathbf{a}(\theta,R,v) \odot (\acute{\mathbf{v}} \otimes (\mathbf{1_L} \otimes \mathbf{1_L})), \tag{4.27}$$

where $\acute{\mathbf{v}} = [0, -j2\pi\frac{f_0 T}{c}, \dots, -j2\pi\frac{f_0 T}{c}(M-1)]^T$. After that, we get $J_{v,v} = J_{3,3}$.

$J_{\theta,r} = J_{r,\theta}$ and can be obtained from $J_{1,2}$ as

$$J_{\theta,r} = 2\frac{A^2}{\sigma_n^2}\frac{\partial \mathbf{a}^H(\theta,R,v)}{\partial \theta}\frac{\partial \mathbf{a}(\theta,R,v)}{\partial R}. \tag{4.28}$$

$J_{v,r} = J_{r,v}$ and can be obtained from $J_{2,3}$ as

$$J_{v,r} = 2\frac{A^2}{\sigma_n^2}\frac{\partial \mathbf{a}^H(\theta,R,v)}{\partial v}\frac{\partial \mathbf{a}(\theta,R,v)}{\partial R}. \tag{4.29}$$

$J_{\theta,v} = J_{v,\theta}$ and can be obtained from $J_{1,3}$ as

$$J_{\theta,v} = 2\frac{A^2}{\sigma_n^2}\frac{\partial \mathbf{a}^H(\theta,R,v)}{\partial \theta}\frac{\partial \mathbf{a}(\theta,R,v)}{\partial v}. \tag{4.30}$$

Finally, the CRB for joint estimation of bistatic range, velocity, and DOA is computed as

$$\mathrm{CRB}(\mathbf{u}) = \mathrm{diag}\left\{\mathbf{J}^{-1}\right\}. \tag{4.31}$$

The CRB derived above is the benchmark for unbiased parameter estimation and will be used as the framework for performance validation of the sparse-based solution proposed in the next Section.

4.3 Proposed Sparsity-based Simultaneous Multi-target Localisation and Doppler Estimation

4.3.1 3D Sparse Representation

In order to introduce sparsity to the antenna and fast-time domains in (4.5), a range-DOA search grid of length G_p such that $G_p << K$ and g_p-th entry $(R_{h,g_p}, \theta_{g_p})$ is defined to represent all the potential locations of the targets from the h-th bistatic measurement. Then, an overcomplete range-DOA steering matrix $\mathbf{P}_{\mathbf{g},h} \in \mathbb{C}^{LN\times G_p}$ is constructed with its g_p-th column given as $\mathbf{p}_{h,g_p} = \mathbf{r}_{h,g_p} \otimes \mathbf{a}_{g_p}$, where

$$\mathbf{a}_{g_p} = \left[1, e^{-j2\pi\frac{f_0 d \sin\theta_{g_p}}{c}}, \ldots, e^{-j2\pi\frac{f_0 d \sin\theta_{g_p}}{c}(L-1)}\right]^T \tag{4.32}$$

and

$$\mathbf{r}_{h,g_p} = \left[1, e^{-j2\pi\frac{\mu R_{h,g_p}}{c}\frac{1}{f_s}}, \ldots, e^{-j2\pi\frac{\mu R_{h,g_p}}{c}\frac{N-1}{f_s}}\right]^T. \tag{4.33}$$

Similarly, in order to introduce sparsity to the slow-time domain, a bistatic velocity search grid of length G_d such that $G_d << K$ and g_d-th entry v_{h,g_d} is defined to represent all the potential bistatic velocities of the targets from the h-th bistatic measurement. Then an overcomplete Doppler steering matrix $\mathbf{V}_{\mathbf{g},h} \in \mathbb{C}^{M\times G_d}$ is constructed with its g_d-th column given as

$$\mathbf{v}_{h,g_d} = \left[1, e^{-j2\pi\frac{f_0 v_{h,g_d}}{c}T}, \ldots, e^{-j2\pi\frac{f_0 v_{h,g_d}}{c}(M-1)T}\right]^T. \tag{4.34}$$

Finally, (4.5) can be written in a sparse format as

$$\mathbf{y}_h = \mathbf{A}_{\mathbf{g},h}\mathbf{x}_{\mathbf{g},h} + \mathbf{w}_h \in \mathbb{C}^{LMN\times 1}, \tag{4.35}$$

where

$$\mathbf{A}_{\mathbf{g},h} = \left[(\mathbf{v}_{h,1} \otimes \mathbf{p}_{h,1}), (\mathbf{v}_{h,2} \otimes \mathbf{p}_{h,2}), \ldots, (\mathbf{v}_{h,G_d} \otimes \mathbf{p}_{h,G_p})\right] \in \mathbb{C}^{LMN\times G_pG_d} \tag{4.36}$$

and $\mathbf{x}_{\mathbf{g},h} \in \mathbb{C}^{G_pG_d\times 1}$ is a sparse vector whose K non-zero entries corresponding to the complex coefficients of the visible targets.

4.3.2 Joint Bistatic Localisation and Doppler Estimation using the LASSO Technique

Following the representation of the measurement signal in (4.35), the problem of motion parameter estimation is cast as an SMV and the popular ℓ_1 minimisation method can be used to recover the support of $\mathbf{x}_{\mathbf{g},h}$ which is directly related to the location and the bistatic velocity of the target. Therefore, consider the following optimisation problem

$$\min_{\mathbf{x}_{\mathbf{g},h}} \|\hat{\mathbf{x}}_{\mathbf{g},n}\|_1 \quad \text{subject to} \quad \|\mathbf{y}_h - \mathbf{A}_{\mathbf{g},h}\hat{\mathbf{x}}_{\mathbf{g},h}\|_2 \le \varepsilon_1, \tag{4.37}$$

where $\mathbf{x}_{\mathbf{g},h}$ is the reconstructed sparse vector and ε_1 is the reconstruction error. The optimisation problem (4.37) is convex and can be solved using the LASSO technique via any open-source solvers such as CVX.

4.4 Simulation Results

Computer simulations were conducted to demonstrate the RMSE performance of the proposed 3D joint motion parameter estimation solution from 1000 Monte Carlo trials. The radar settings used are shown in Table 4.1. A scenario is considered where a single roadside sensor and sensing vehicle are in operation, and the latter is estimating the bistatic range and velocity, as well as DOA, of a single point-like target simultaneously by solving the optimisation problem (4.37). A search grid is defined such that each domain has 7 potential grid points with a combined length of $G_dG_p = 343$. The granularity is first chosen as 1 (m, m/s, or °) to provide a coarse estimate of the target parameters, and is then reduced to 0.15 for all three domains. So, the total search region for each domain is initially 7 (m, m/s, or ◦), and is then reduced

TABLE 4.1: Radar settings used in producing the RMSE performance against the CRB

Parameter	**Value**	**Parameter**	**Value**
P_t	10 dBm	f_0	77 GHz
G_t	23 dBi	B	300 MHz
G_r	16 dBi	T_c	25 μs
σ_{bi}	0 dBsm	T	30 μs
SNR_o	$-$10–20 dB	f_s	5 MHz
M	9	N	125
L	9	d	1.948 mm

to 1.05 centred around the initial coarse estimate. In each trial, a new realisation of the noise signal is generated and the target parameters are drawn from a uniform distribution bounded by two adjacent grid points. This approach allows producing more accurate RMSE results while avoiding further reduction in the granularity of the search grid which is computationally exhaustive. So, with sufficient number of trials, it is intuitive that the RMSE performance may reach its asymptotic bound. The CRB derived in Section 3.3 is used as the benchmark for performance against varying levels of SNR_o (output SNR) which is defined as the ratio between the power of the received signal and the receiver noise power. The estimation results using 3D FFT and 3D MUSIC are used for comparison. In Figure 4.1, the computed RMSE from each method and the CRB are shown for each parameter.

It can be seen that the LASSO technique clearly outperforms the FFT at all levels of SNR_o, and outperforms MUSIC at SNR_o levels below 10 dB. It is however important to mention that matching the CRB trend requires higher level of granularity in the search grids which is computationally costly and difficult to achieve with the available computing power. The aim of this simulation is to focus on the estimation accuracy of the algorithm with the search grid zooming in to esimate the parameter with the lowest possible error. Clearly, FFT is disadvantaged here as the grid is fixed since it depends on the number of measurements in each domain. However, that highlights the advantage of parameteric search methods. With MUSIC and LASSO sharing the same search grid, it is evident that sparsity-based estimation can outperform subspace-based algorithms.

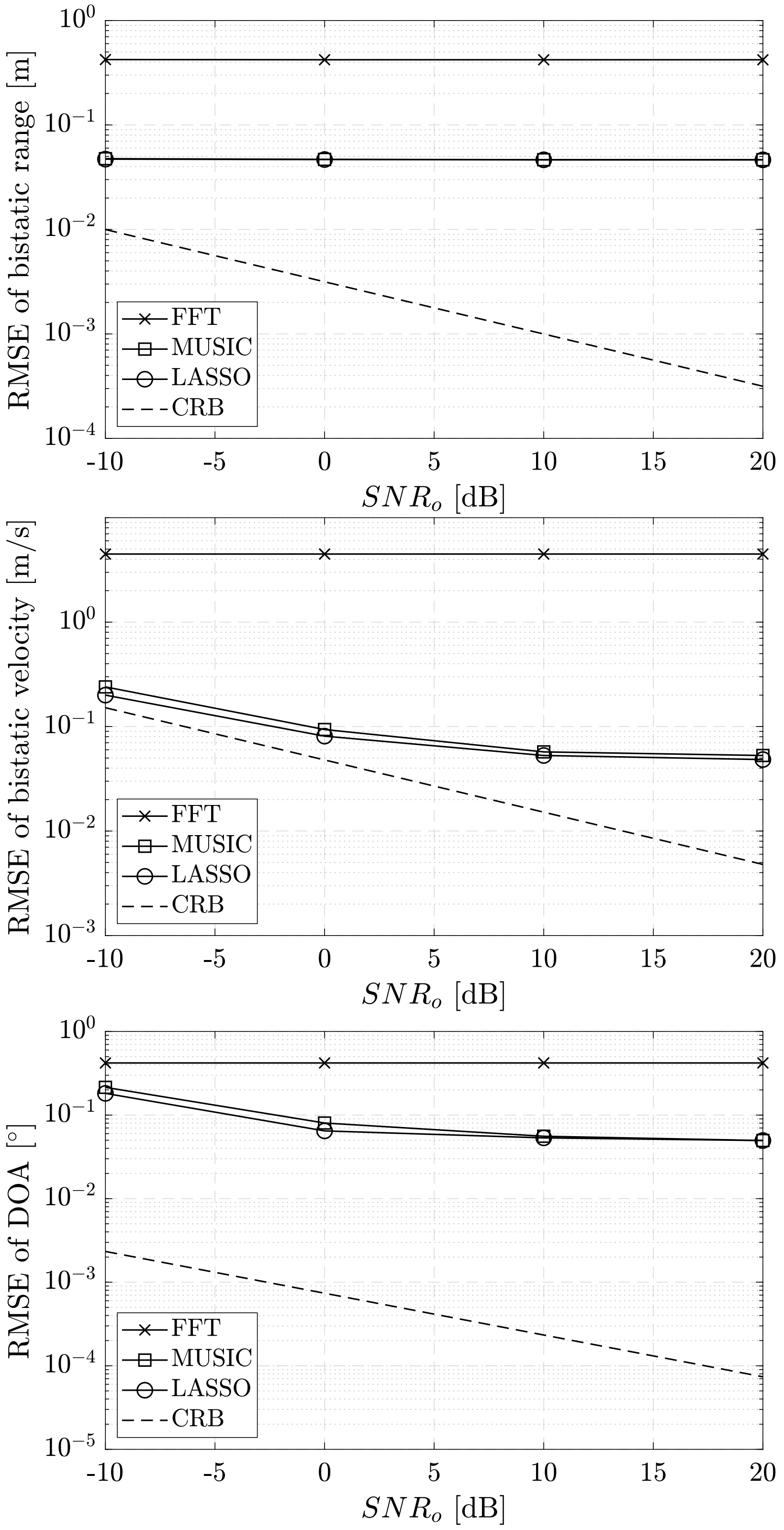

FIGURE 4.1: A comparison of the computed RMSE against the CRB for joint estimation of the motion parameters in the proposed bistatic automotive application using FFT, MUSIC, and LASSO.

4.5 Summary

In this Chapter, a 3D sparse representation for bistatic automotive radar measurement was derived. Unlike the signal model derived in Chapter 3, the contribution of the direct-path signal was neglected here to focus on the performance of parameter estimation from the bistatic signals only with different methods. Then, a sparsity-based solution for joint motion parameter estimation was proposed. The CRB was derived for a Gaussian distributed signal providing a lower bound for the estimation bias. It was proven through computer simulations the feasibility of jointly estimating the bistatic range, velocity, and DOA of the target using the LASSO technique which clearly outperforms FFT and MUSIC (albeit with a smaller margin) at different levels of SNR_o. In the conducted simulations, a single point-like target was considered with a two-stage search to firstly provide a coarse estimate of the parameter and then refine the search to explore the potential of the different methods in achieving an estimation bias in the order of the CRB. In the next Chapter, to fully exploit the advantages of separating the transmitter from the receiver, the problem is extended to the multistatic case where data fusion is achieved by employing the GS concept.

Chapter 5

Multistatic Operation by Exploiting the Concept of Group Sparsity

5.1 Introduction

The interests to bistatic and multistatic radars resurged in the 1990s with more research drawn into statistical MIMO radar, bistatic SAR, remote sensing, and stealthy detection [160, 161, 86, 96, 162]. Bistatic and multistatic radars are also the foundation of passive radar systems as a means of green sensing technology [163, 164]. However, bistatic radar has since then struggled to break into the automotive industry, partly due to the very strict synchronisation requirements (in the order of nanoseconds [149]). Nonetheless, motivated by the drive in the fifth-generation (5G) communications and beyond to meet the requirements of vehicular applications [102], [165], as well as some advances in experimental radar synchronisation [136, 139, 141], automotive bistatic applications have been recently proposed to offer joint communication and radar capability for vehicles transmitting known communication modulation waveforms [166], enhanced detection in smart highway scenarios using cooperative roadside sensors transmitting radar signals [167, 168], and improved radar performance for vehicles exploiting a superposition of their monostatic measurements and bistatic ones from other road users [111]. At the same time, there are potential problems with such applications when employing Fourier techniques for localisation.

In this Chapter, an extension to the bistatic automotive application is proposed where multiple cooperative roadside sensors are considered, resulting in a configuration known as multistatic (see Figure 5.1). The focus here is on

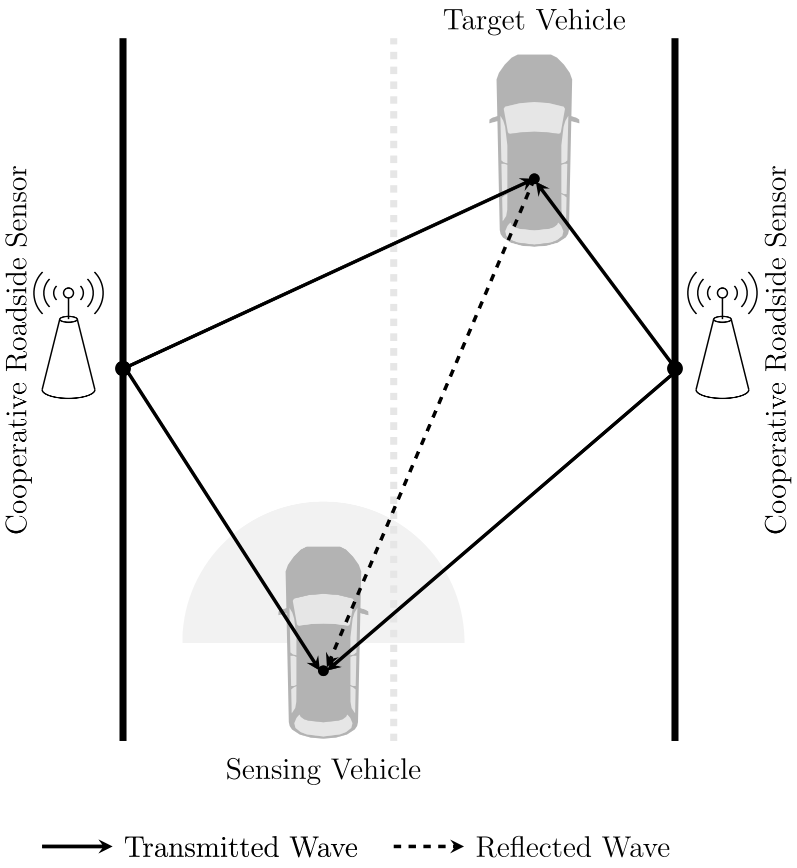

FIGURE 5.1: Multistatic automotive localisation scenario using multiple cooperative roadside sensors.

the 2D localisation problem where the target range and DOA are simultaneously estimated followed by Doppler estimation for multiple targets. This problem is referred to as 3D motion parameter estimation albeit different to that in Chapter 4 where all motion parameters are jointly estimated. Although the high efficiency of 3D FFT and its good performance make it a straightforward candidate for extracting frequency information from an accumulation of signals corrupted by white noise [43], when multiple roadside sensors are in operation, it becomes difficult using FFT to coherently integrate range and Doppler measurements from different transmitter-receiver pairs [169]. To overcome this issue, more advanced signal processing techniques are needed, allowing processing information from multiple bistatic transmitter-receiver pairs on the data level.

Researchers have adopted sparse representation from the CS framework and developed radar signal models for the DOA estimation problem [170, 171, 172, 69] that can naturally be solved by popular techniques such as group LASSO [71, 173], also known as $\ell_{2,1}$ minimisation, and multistatic Bayesian sparse learning [174, 175, 176]. In particular, the structured sparsity problem arises when multiple sources of information share a common support set under the generally accepted narrowband assumption. Therefore, it naturally exists in radar applications, for instance, when multiple pulses, transmitters, or receivers are employed.

In this Chapter, it is shown that the extra degrees of freedom (DoFs) offered by prior information and multiple transmitters can be directly exploited following a sparse representation. The road is mapped as a Cartesian grid and enforce sparsity for simultaneous 2D localisation, followed by Doppler estimation. With this approach, the exhaustive 3D parameter search presented in Chapter 4 is avoided, thereby significantly reducing the computational complexity. In order to pair the estimated location and Doppler parameters for each target, two data association methods are proposed with varying performance and computational complexity. Extensive computer simulations convey the feasibility and superiority of the proposed sparsity-based positioning solutions in multistatic automotive configurations, and prove the success of the proposed data association methods under different settings.

In the rest of this Chapter, a multistatic FMCW radar signal model is derived in Section 5.2. Then, a multi-target location and Doppler estimation solution employing the GS concept in multistatic automotive configuration is proposed in Section 5.3. Finally, simulation results are presented in Section 5.4, and conclusions are drawn in Section 5.5.

5.2 Multistatic FMCW Radar Signal Model

Consider H stationary roadside sensors, each transmitting FMCW chirps. In reality, some form of orthogonality is introduced between the signals from different sensors to allow separating them at the receiver end [177]. Let $(R,\theta)_k := (R_k, \theta_k)$ and $(R,\theta)_h := (R_h, \theta_h)$. Following earlier assumptions, the parameters $(R,\theta)_h$ are known to the sensing vehicle. By exploiting this and using the geometry depicted in Figure 3.2, $\acute{R}_{h,k}$ can be obtained as

$$\acute{R}_{h,k} = \sqrt{R_k^2 + R_h^2 - 2R_k R_h \cos(\theta_h - \theta_k)} + R_k. \tag{5.1}$$

The aim is to estimate $(R,\theta)_k$ and v_k. After applying 3D FFT to (4.2), the spectrum would show K peaks corresponding to $(\acute{R}_{h,k}, \theta_k, v_{h,k})$ for all k. Using

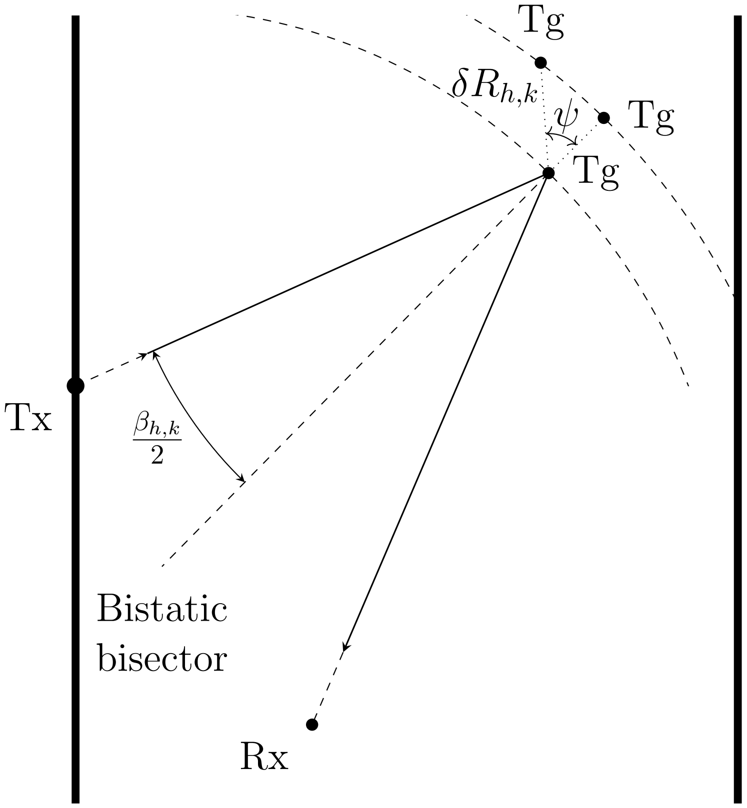

FIGURE 5.2: Range resolution in bistatic radar.

(5.1), R_k can be calculated as

$$R_k = \frac{\acute{R}_{h,k}^2 - R_h^2}{2\acute{R}_{h,k} - 2R_h \cos(\theta_h - \theta_k)}. \tag{5.2}$$

After R_k and θ_k are estimated, assuming known v, v_k can be estimated using (3.10).

The generalised range resolution can be defined as [149]

$$\delta R_{h,k}(\psi) = \frac{c}{2B\cos(\beta_{h,k}/2)\cos\psi}, \tag{5.3}$$

where $\beta_{h,k}$ is the bistatic angle (shown in Figure 3.2) and ψ is the rotation angle from the bistatic bisector as shown in Figure 5.2.

Remark. *In bistatic radar, the range resolution varies in 2D depending on the geometry. Therefore, it can no longer be defined in one specific direction (such as down-range in the monostatic case). In (2.5), the direction of range resolution is dictated by the rotation angle ψ away from the bistatic bisector which is considered as the reference point (see Figure 5.2 for an illustration of three possible placements of targets). Clearly, the down-range resolution is maximum when $\psi = 0°$, and as one* *target rotates away from the bisector* ($\psi > 0^\circ$)*, the resolution is degraded. When* $\psi = 90^\circ$*, the two considered targets lie on the same iso-range contour and can no longer be resolved in the range domain.*

On the other hand, $\beta_{h,k}$ *determines the effect of the bistatic geometry on the overall range resolution regardless of the direction of interest. Clearly, when* $\beta_{h,k} = 0^\circ$*, the bistatic range resolution is maximised and reduces to the monostatic one. It is important to note here that, for a given target, the range resolution varies with the location of the h-th roadside sensor. This highlights the advantage of multistatic configuration in increasing the number of DoFs when signal processing techniques permit fusion at the data level. In the case of Fourier-based estimation, although two targets that cannot be resolved in the range domain may still be resolved in the range-DOA 2D FFT spectra, the conversion in* (5.2) *to calculate the range* R_k *introduces some bias imposed by the estimate of* θ_k*. Similarly, the conversion in* (3.10) *to calculate the velocity* v_k *introduces some bias imposed by the estimates of* R_k *and* θ_k*.*

Some further problems emerge when using Fourier-based estimation in this application. The first problem occurs when some information is known *a priori*, since the FFT fails to integrate such information directly and can only be done in post-processing steps. The second problem naturally arises in the multistatic configuration because the FFT cannot be applied across the domain created by the multiple roadside sensors. In other words, the FFT cannot be applied across the signals received from H roadside sensors in a similar manner to the signals received at L antennas, for instance, since there is no correlation between the H signals. This limits the benefit of integration gain to the domain corresponding to the parameter being estimated [178]. It follows that the fusion of multistatic signals in the FFT domain may only be done post-calculation rather than at the measurement level. Furthermore, suppose there exist H independent FFT spectra from which R_k is estimated. The final estimate after averaging can be expressed as

$$\bar{R}_k = R_k + \bar{\epsilon}, \tag{5.4}$$

such that

$$\bar{\epsilon} = \frac{1}{H}\sum_{h=1}^{H} \epsilon_h, \tag{5.5}$$

where ϵ_h denotes the bias of the calculated range from the h-th source of information. When ϵ_h follows a Gaussian distribution $\mathcal{N}(\bar{\mu}, \sigma_a^2)$ with $\bar{\mu}$ and σ_a^2 being the mean and variance, respectively, then $\bar{\epsilon}$ follows $\mathcal{N}(\bar{\mu}, \sigma_a^2/H)$. In this case, averaging the estimates only reduces the error variance by a factor of H, but does not affect the shape of the PDF. This analysis also applies to the averaging estimates of v_k. For DOA estimation, one may argue that the DOA-FFT spectra can be averaged directly because all H signals share the same frequencies corresponding to θ_k. However, such an approach, often known as incoherent integration, may only reduce the variance of the estimated noise floor, meaning that the average noise power level remains unchanged.

5.3 Proposed Multistatic Location and Doppler Estimation Using GS in Multi-target Automotive Scenarios

5.3.1 Sparse Representation for Multistatic Cartesian 2D Localisation

Recall the signal model defined for the measurement from the h-th roadside sensor in (4.4). With the help of the relation in (5.1), it can be seen that one DoF associated with such representation is the ability to design the steering matrix to incorporate $(R,\theta)_h$ known prior to estimation. Therefore, a 2D polar grid of length G_p is defined to search for range and DOA $(R,\theta)_{g_p} := (R_{g_p}, \theta_{g_p})$ to simultaneously estimate $(R,\theta)_k$. Then, for each roadside sensor, an overcomplete range-DOA steering matrix $\mathbf{P}_{\mathbf{g},h} \in \mathbb{C}^{LN \times G_p}$ is constructed with its g_p-th column given as $\tilde{\mathbf{p}}_{h,g_p} = \tilde{\mathbf{r}}_{h,g_p} \otimes \mathbf{a}_{g_p}$, where

$$\tilde{\mathbf{r}}_{h,g_p} = \begin{bmatrix} 1 \\ e^{-j2\pi\left[\left(\mu\sqrt{R_{g_p}^2 + R_h^2 - 2R_{g_p}R_h\cos(\theta_h - \theta_{g_p})} + R_{g_p}\right)\frac{1}{cf_s}\right]} \\ \vdots \\ e^{-j2\pi\left[\left(\mu\sqrt{R_{g_p}^2 + R_h^2 - 2R_{g_p}R_h\cos(\theta_h - \theta_{g_p})} + R_{g_p}\right)\frac{N-1}{cf_s}\right]} \end{bmatrix}. \tag{5.6}$$

Thus, (4.4) can be written in a standard sparse format as

$$\mathbf{Y}_h^{\mathbf{P}} = \mathbf{P}_{\mathbf{g},h}\mathbf{X}_{\mathbf{g},h}^{\mathbf{P}} + \mathbf{W}_h, \tag{5.7}$$

where $\mathbf{X}_{\mathbf{g},h}^{\mathbf{P}} \in \mathbb{C}^{G_p \times M}$ is a sparse data matrix whose m-th column contains K non-zero entries corresponding to the complex coefficients of target echoes from the h-th transmitted signal. It is assumed that all columns have the exact support set containing the indices of the non-zero entries.

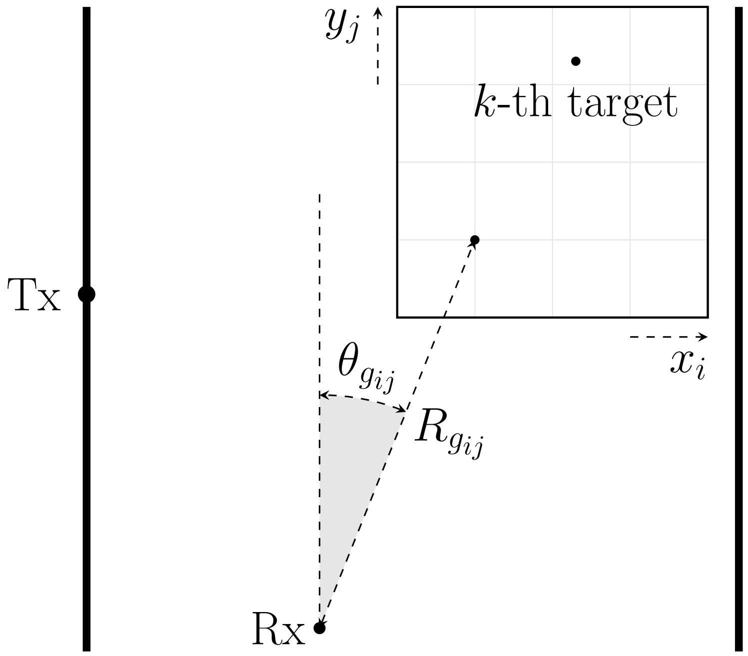

FIGURE 5.3: Proposed 2D rectangular search grid.

This road scenario motivates the idea of constructing a 2D rectangular search grid of size $I \times J$ and coordinates (x_i, y_j) with $i = 1, 2, \ldots, I$ and $j = 1, 2, \ldots, J$ as shown in Figure 5.3. By taking the sensing vehicle as the centre of the Cartesian map, it is clear that y_j is always positive whereas the sign of x_i mirrors θ_{g_p} with the forward line being the reference. Following this, the subscript g_p is now replaced with g_{ij} which corresponds to the ij-th bin in the 2D rectangular grid.

Next, the g_{ij}-th column in $\mathbf{P}_{\mathbf{g},h}$ can be constructed by converting the ij-th Cartesian coordinates (x_i, y_j) into polar coordinates $(R, \theta)_{g_{ij}} := (R_{g_{ij}}, \theta_{g_{ij}})$ as

$$(R, \theta)_{g_{ij}} = \left(\sqrt{x_i^2 + y_j^2}, \arcsin\left(\frac{x_i}{\sqrt{x_i^2 + y_j^2}} \right) \right). \tag{5.8}$$

Accordingly, the Cartesian coordinates of the k-th target can be defined as

$$(x, y)_k = (R_k \sin\theta_k, R_k \cos\theta_k) \tag{5.9}$$

and do not necessarily lie on an exact coordinate of the generated rectangular search grid.

5.3.2 Sparse Representation for Multistatic Doppler Estimation

The raw data in (4.4) is reshaped to get

$$\mathbf{Z}_h = \mathbf{Y}_h^T. \tag{5.10}$$

A velocity grid of length G_d is defined to search for v_{h,g_d} to estimate $v_{h,k}$. Then, an overcomplete Doppler steering matrix $\mathbf{V}_{\mathbf{g},h} \in \mathbb{C}^{M\times G_d}$ is constructed by replacing $v_{h,k}$ with v_{h,g_d} in $\mathbf{V}_h$ such that

$$v_{h,g_d} \in \left[v_{\min,h}, v_{\max,h}\right], \tag{5.11}$$

where

$$v_{\min,h} = \min_{\alpha_{h,g_{ij}},\theta_k} \left\{ v_{\min}[\cos(\alpha_{h,g_{ij}}) + \cos(\theta_k)] - v\cos(\theta_k) \right\},$$

$$v_{\max,h} = \max_{\alpha_{h,g_{ij}},\theta_k} \left\{ v_{\max}[\cos(\alpha_{h,g_{ij}}) + \cos(\theta_k)] - v\cos(\theta_k) \right\},$$

$$\alpha_{h,g_{ij}} = \begin{cases} \arcsin\left(\frac{R_h \sin(|\theta_h - \theta_{g_{ij}}|)}{\sqrt{R_{g_{ij}}^2 + R_h^2 - 2R_{g_{ij}}R_h\cos(\theta_h-\theta_{g_{ij}})}}\right) \\ \qquad +\theta_{g_{ij}}, \quad \text{for} \quad \theta_h \leq 0^\circ, \\ \arcsin\left(\frac{R_h \sin(|\theta_h - \theta_{g_{ij}}|)}{\sqrt{R_{g_{ij}}^2 + R_h^2 - 2R_{g_{ij}}R_h\cos(\theta_h-\theta_{g_{ij}})}}\right) \\ \qquad -\theta_{g_{ij}}, \quad \text{for} \quad \theta_h \geq 0^\circ, \end{cases} \tag{5.12}$$

and $v_{\min}$ and $v_{\max}$ denote the minimum and maximum values of the potential forward velocities of the target, respectively. Accordingly, $\mathbf{Z}_h$ can now be written in a standard sparse format as

$$\mathbf{Z}_h^{\mathbf{D}} = \mathbf{V}_{\mathbf{g},h}\mathbf{X}_{\mathbf{g},h}^{\mathbf{D}} + \mathbf{W}_h^T, \tag{5.13}$$

where $\mathbf{X}_{\mathbf{g},h}^{\mathbf{D}} \in \mathbb{C}^{G_d \times LN}$ is a sparse data matrix whose $(lN+n)$-th column contains K non-zero entries corresponding to the complex coefficients of the visible targets and have the same support set.

5.3.3 Multistatic Localisation and Doppler Estimation Using GS

Firstly, the 2D location denoted by $(x, y)_k$ is to be estimated through reconstructing $\mathbf{X}^{\mathbf{P}}_{\mathbf{g},h}$ from $\mathbf{Y}_h$. All columns in the H matrices $\mathbf{X}^{\mathbf{P}}_{\mathbf{g},h}$ have the same support set corresponding to K locations $(x, y)_k$. So, the concept of GS can be employed across M pulses and H sensors by generating an $LN \times MH$ measurement matrix $\mathbf{B}^{\mathbf{P}}_{\mathbf{g}}$ and a $G_p \times MH$ sparse data matrix $\mathbf{U}^{\mathbf{P}}_{\mathbf{g}}$ as

$$\mathbf{B}^{\mathbf{P}}_{\mathbf{g}} = \left[\mathbf{P}_{\mathbf{g},1}\mathbf{X}^{\mathbf{P}}_{\mathbf{g},1}, \mathbf{P}_{\mathbf{g},2}\mathbf{X}^{\mathbf{P}}_{\mathbf{g},2}, \ldots, \mathbf{P}_{\mathbf{g},H}\mathbf{X}^{\mathbf{P}}_{\mathbf{g},H}\right], \tag{5.14}$$

$$\mathbf{U}^{\mathbf{P}}_{\mathbf{g}} = \left[\mathbf{X}^{\mathbf{P}}_{\mathbf{g},1}, \mathbf{X}^{\mathbf{P}}_{\mathbf{g},2}, \ldots, \mathbf{X}^{\mathbf{P}}_{\mathbf{g},H}\right]. \tag{5.15}$$

Denote row vector $\mathbf{u}^{\mathbf{P}}_{\mathbf{g},g_p}$ as the g_p-th row of the matrix $\mathbf{U}^{\mathbf{P}}_{\mathbf{g}}$. By computing the ℓ_2 norm to each row vector $\mathbf{u}^{\mathbf{P}}_{\mathbf{g},g_p}$, a new column vector is formed as

$$\widetilde{\mathbf{u}}^{\mathbf{P}}_{\mathbf{g}} = \left[\|\mathbf{u}^{\mathbf{P}}_{\mathbf{g},1}\|_2, \|\mathbf{u}^{\mathbf{P}}_{\mathbf{g},2}\|_2, \ldots, \|\mathbf{u}^{\mathbf{P}}_{\mathbf{g},G_p}\|_2\right]^T. \tag{5.16}$$

Then, the GS-based multistatic localisation method is formulated as follows [58, 179]

$$\min_{\mathbf{U}^{\mathbf{P}}_{\mathbf{g}}} \quad \|\widetilde{\mathbf{u}}^{\mathbf{P}}_{\mathbf{g}}\|_1 \quad \text{subject to} \quad \|\mathbf{Y}^{\circ} - \mathbf{B}^{\mathbf{P}}_{\mathbf{g}}\|_F \leq \varepsilon_2, \tag{5.17}$$

where

$$\mathbf{Y}^{\circ} = \left[\mathbf{Y}_1, \mathbf{Y}_2, \ldots, \mathbf{Y}_H\right], \tag{5.18}$$

and ε_2 is the reconstruction error.

Next, after estimating $(x, y)_k$, the bistatic velocity parameter denoted by $v_{h,k}$ is to be estimated through reconstructing $\mathbf{X}^{\mathbf{D}}_{\mathbf{g},h}$ from $\mathbf{Z}_h$. Notice that, while the columns in $\mathbf{X}^{\mathbf{D}}_{\mathbf{g},h}$ share the same support set, the latter varies across H Doppler data matrices. This is dictated by the steering matrix $\mathbf{V}_{\mathbf{g},h}$ that is designed to search for $v_{h,k}$ rather than v_k. Alternatively, the steering matrix could be designed to directly search for v_k. In such a case, all columns in the H data matrices would share the same support set corresponding to all K parameters. Although this approach may offer the advantage of employing the GS concept across H sensors as well as L antennas and N snapshots, it may suffer from ambiguities due to the coupling between velocity, range, and DOA in (3.6) and (3.7). To illustrate this, the search grid would have to be populated K times and, depending on the 2D locations of the targets, the estimated bistatic velocities may migrate to other values which do not necessarily correspond to their true velocities in the search grid. This is due to the fact that there is no mechanism in ℓ_1 norm to ensure either an even or an uneven distribution of sparsity among all K groups of the search grid. Ideally, sparsity can be enforced across all H sensors to estimate R_k, θ_k, and v_k simultaneously. However, this requires handling steering matrices of size $LMN \times G_d G_p$ which is computationally exhaustive.

For the h-th measurement matrix $\mathbf{Z}_h$, the GS concept can be employed across LN snapshots. Therefore, Doppler estimation is performed by solving the following optimisation problem

$$\min_{\mathbf{X}^{\mathbf{D}}_{\mathbf{g},h}} \quad \|\tilde{\mathbf{x}}^{\mathbf{D}}_{\mathbf{g},h}\|_1 \quad \text{subject to} \quad \|\mathbf{Z}_h - \mathbf{V}_{\mathbf{g},h}\mathbf{X}^{\mathbf{D}}_{\mathbf{g},h}\|_F \leq \varepsilon_3, \tag{5.19}$$

where

$$\tilde{\mathbf{x}}^{\mathbf{D}}_{\mathbf{g},h} = \left[\|\mathbf{x}^{\mathbf{D}}_{\mathbf{g},h,1}\|_2, \|\mathbf{x}^{\mathbf{D}}_{\mathbf{g},h,2}\|_2, \ldots, \|\mathbf{x}^{\mathbf{D}}_{\mathbf{g},h,G_d}\|_2\right]^T, \tag{5.20}$$

$\mathbf{x}^{\mathbf{D}}_{\mathbf{g},g_d}$ is the g_d-th column of $\mathbf{X}^{\mathbf{D}}_{\mathbf{g}}$ and ε_3 is the reconstruction error. Both optimisation problems (5.17) and (5.19) are convex and can be solved using existing convex optimisation toolboxes. Finally, the proposed GS-based method for location and Doppler estimation of K targets in this multistatic automotive scenario is summarised in Algorithm 2.

Algorithm 2 A GS-based location and Doppler estimation algorithm for multistatic automotive application.

```
Require: $\mathbf{Y}_h, R_h, \theta_h, v, f_0, \mu, d, T, M, L, f_s, N, H$.
  Obtain and store the raw data $\mathbf{Y}_h$ for all $h$ as in (4.3).
  Generate an $I \times J$ rectangular search grid of length $G_p$ after choosing appropriate values for $(x_1, y_1)$ and $(x_I, y_J)$.
  Convert the Cartesian coordinates $(x_i, y_j)$ to polar coordinates $(R, \theta)_{g_{ij}}$ using (5.8).
  For each roadside sensor, construct a range-DOA steering matrix $\mathbf{P}_{\mathbf{g},h}$ whose $g_{ij}$-th column corresponds to $(x_i, y_j)$.
  Estimate $\mathbf{U}^{\mathbf{P}}_{\mathbf{g}}$ by solving the optimisation problem (5.17).
  Perform a peak search to find the estimated coordinates of $K$ targets.
  Reshape the raw data as in (5.10) to get $\mathbf{Z}_h$.
  After selecting appropriate values of $v_{\min}$ and $v_{\max}$, using $v$ and all $G_p$ values of $(R, \theta)_{g_{ij}}$, calculate $v_{\min,h}$ and $v_{\max,h}$ for all $h$ using (5.12).
  Generate $H$ velocity search grids of length $G_d$ using (5.11).
  For each roadside sensor, construct a Doppler steering matrix $\mathbf{V}_{\mathbf{g},h}$ whose $g_d$-th column corresponds to $v_{h,g_d}$.
  Estimate $\mathbf{X}^{\mathbf{D}}_{\mathbf{g},h}$ by solving the optimisation problem (5.19) for all $h$.
  Perform a peak search to find the estimated bistatic velocity values of $K$ targets.
      return Estimates of $(x, y)_k$ and $v_{h,k}$ for all $K$ targets.
```

5.3.4 Parameter Pairing using Cross-Correlation and ESPRIT

While the values of $(x, y)_k$ and $v_{h,k}$ can be estimated using Algorithm 2, the information regarding the association of the location with the corresponding bistatic velocity for each target remains unknown. Such pairing is essential for establishing a complete profile about the targets and for computing the velocity v_k using (3.10). So, motivated by the cross-correlation (CC)-based pair-matching method for elevation and azimuth in L-shaped antenna arrays [180], a modification is proposed here for matching the location and bistatic velocity pairs. Each 2D location corresponds to a unique angle θ_k, so the parameter association task renders a matching between the DOA and bistatic velocity parameters. This can be done by exploiting the CC matrix $\mathbf{R}_{\boldsymbol{\theta v},h}$ which is defined as

$$\mathbf{R}_{\boldsymbol{\theta v},h} = \mathrm{E}\left\{\mathbf{y}_{\boldsymbol{\theta},h}(n)\mathbf{y}^{H}_{\boldsymbol{v},h}(n)\right\}, \tag{5.21}$$

where the l-th entry of $\mathbf{y}_{\boldsymbol{\theta},h}(n) \in \mathbb{C}^{L\times 1}$ is equal to $\hat{y}_h[l, 0, n]$ in (4.1) and the m-th entry of $\mathbf{y}_{\boldsymbol{v},h}(n) \in \mathbb{C}^{M\times 1}$ is equal to $\hat{y}_h[0, m, n]$. Clearly, $\mathbf{R}_{\boldsymbol{\theta v},h}$ can only be computed when $L = M$. Unlike the case in [180] where both received signals corresponding to the two components of the L-shaped array have the same length, L is smaller than M in the underlying problem. Therefore, only the first L entries of $\mathbf{y}_{\boldsymbol{v},h}(n)$ are considered, from which $\check{\mathbf{y}}_{\boldsymbol{v},h}(n)$ is formed. Accordingly, $\mathbf{R}_{\boldsymbol{\theta v},h}$ becomes an $L \times L$ matrix whose diagonal elements lead to the following formulation

$$\mathbf{d}_{\boldsymbol{\theta v},h} = \left[\sum_{k=1}^{K} q_{h,k}, \sum_{k=1}^{K} q_{h,k}, e^{-j\zeta\omega_{h,k}}, \ldots, \sum_{k=1}^{K} q_{h,k}, e^{-j\zeta(L-1)\omega_{h,k}}\right]^T, \tag{5.22}$$

where $\zeta = 2\pi f_0/c$ and $\omega_{h,k} = d\sin\theta_k - TV_{h,k}$. Denote by $\hat{\mathbf{d}}_{\boldsymbol{\theta v},h}$, $\hat{\theta}_k$, $\hat{v}_{h,k}$, and $\hat{\omega}_{h,k}$ the estimated versions of $\mathbf{d}_{\boldsymbol{\theta v},h}$, θ_k, $v_{h,k}$, and $\omega_{h,k}$ respectively. The implementation for the pairing method can then be summarised as follows.

1. Using the estimated values $\hat{\theta}_k$ and $\hat{v}_{h,k}$, calculate K^2 combinations of $\{d\sin\hat{\theta}_{k_\theta} - T\hat{v}_{h,k_v}\}$, where $k_\theta, k_v = 1, 2, \ldots, K$.

2. Obtain $\hat{\mathbf{d}}_{\boldsymbol{\theta v},h}$ from $\mathbf{y}_{\boldsymbol{\theta},h}$ and $\check{\mathbf{y}}_{\boldsymbol{v},h}$ as

$$\hat{\mathbf{d}}_{\boldsymbol{\theta v},h} = \frac{1}{N}\sum_{n=1}^{N} \mathbf{y}_{\boldsymbol{\theta},h}(n) \odot \check{\mathbf{y}}^{*}_{\boldsymbol{v},h}(n), \tag{5.23}$$

then construct a Hermitian Toeplitz matrix, $\hat{\mathbf{R}}_{\boldsymbol{cc},h}$, whose first column is $\hat{\mathbf{d}}_{\boldsymbol{\theta v},h}$.

3. Apply ESPRIT to $\hat{\mathbf{R}}_{\boldsymbol{cc},h}$ to estimate $\omega_{h,k}$ for K targets.
4. For the k-th target, the correct combination of DOA and velocity parameters is determined by solving the following minimisation problem

$$\min_{k_\theta,k_v} \quad \left| e^{-j\zeta\hat{\omega}_{h,k}} - e^{-j\zeta(d\sin\hat{\theta}_{k_\theta} - T\hat{v}_{h,k_v})} \right| . \tag{5.24}$$

Note that Step 4 above adopts the comments in [181] to expand the unambiguous parameter range of this pair matching method.

5.3.5 Parameter Pairing based on Least Squares

Unlike the previous parameter association method, matching here is done between the estimated 2D locations and the bistatic velocity parameters. To illustrate this, consider the following reformulation of (4.4)

$$\mathbf{y}_h = \mathrm{vec}\{\mathbf{Y}_h\} = \mathbf{A}_h\mathbf{x}_h + \mathbf{w}_h, \tag{5.25}$$

where

$$\mathbf{A}_h = \left[(\mathbf{p}_{h,1}\otimes\mathbf{v}_{h,1}), (\mathbf{p}_{h,2}\otimes\mathbf{v}_{h,2}), \ldots, (\mathbf{p}_{h,K}\otimes\mathbf{v}_{h,K})\right], \tag{5.26}$$

$$\mathbf{x}_h = \left[q_{h,1}, q_{h,2}, \ldots, q_{h,K}\right]^T, \tag{5.27}$$

and $\mathbf{w}_h = \mathrm{vec}\{\mathbf{W}_h\}$. By focusing on $\mathbf{A}_h$, it can be seen that once $\mathbf{p}_{h,k}$ and $\mathbf{v}_{h,k}$ are constructed from the estimated location and bistatic velocity, the task becomes to find the combination that minimises the distance between the matrix $\mathbf{A}_h$ and its reconstruction. Thus, the following least-squares (LS)-based minimisation problem is proposed

$$\min_{\hat{\mathbf{A}}_h} \quad \left\| \mathbf{y}_h - \hat{\mathbf{A}}_h(\hat{\mathbf{A}}_h^H\hat{\mathbf{A}}_h)^{-1}\hat{\mathbf{A}}_h^H\mathbf{y}_h \right\|_2, \tag{5.28}$$

where $\hat{\mathbf{A}}_h$ is the estimate of $\mathbf{A}_h$ and is constructed from the estimated values of location and bistatic velocity. For K targets with different location and bistatic velocity, $K!$ candidates of $\hat{\mathbf{A}}_h$ are considered. The main advantage of this method is that the correct combination is determined for all K targets simultaneously. The minimisation in (5.28) can be interpreted as a maximum likelihood approach due to the AWGN assumption [43].

TABLE 5.1: Radar settings used in the simulation of the multistatic automotive scenario

Parameter	Value	Parameter	Value
P_t	10 dBm	f_s	5 MHz
G_t	23 dBi	T_c	30 μs
G_r	16 dBi	T	35 μs
σ_{bi}	0 dBsm	N	150
B	150 MHz	M	128
f_0	77 GHz	L	8
SNR_i	$100 - 160$ dB	d	1.948 mm

Remark. *So far it has been assumed that all K targets have different locations and bistatic velocities, hence only $K!$ candidates are considered in the LS-based pair-matching method. While the CC-based method allows repetition in both the location and Doppler domains, it is in fact forced to do so by the nature of its minimisation that is repeated K times, and there is no theoretical criterion to eliminate any of the combinations after processing each target. On the other hand, using the LS-based method repetition may only occur in the Doppler domain since the targets will in reality be located at different 2D locations. Therefore, in order to generalise this proposed method, $K!$ can be treated as the lower bound on the number of possible candidates of $\hat{\mathbf{A}}_h$ and, in an extreme case, when some targets share the exact bistatic velocity, up to K^K candidates may need to be considered. In such case, the computational cost may be noted as a disadvantage when using this method.*

5.4 Simulation Results

In order to evaluate the success of the proposed GS-based solution in processing multistatic automotive radar signals and convey its advantage over the state-of-art, computer simulations were run using MATLAB and the CVX package. The radar settings used are shown in Table 5.1. For parameter estimation, the RMSE is used as the performance metric. The MUSIC method is used as the baseline for comparison due to its super-resolution capability and its ability to use the same search grids generated for the GS-based method. The performance metric was measured in two different settings: varying input SNR (SNR_i) and varying number of processed pulses/snapshots. Note that the SNR_i, defined as

$$SNR_i = \frac{P_t G_t}{P_n}, \tag{5.29}$$

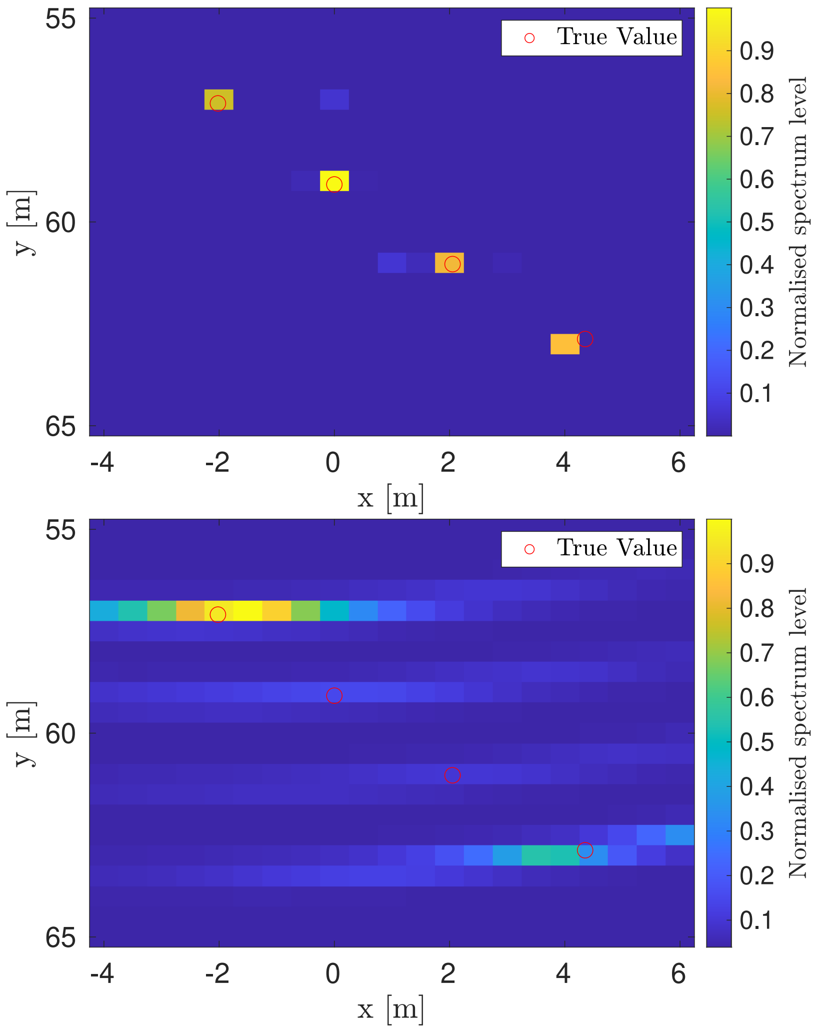

FIGURE 5.4: A comparison of a 2D location map computed using GS (top) and MUSIC (bottom) for 4 point targets at $SNR_i = 150$ dB with 8 processed pulses.

where P_n is the noise power at the receiver, is used here as opposed to the conventional output SNR defined at the receiver. Following this approach is more suitable when the received signal is a superposition of signals from multiple targets with different ranges. To illustrate this, the output SNR can be defined as

$$SNR_o = \frac{P_t G_t G_r \sigma_{\text{bi}} c^2}{(4\pi)^3 f_0^2 R_{Tx}^2 R_{Rx}^2 P_n} = \frac{G_r \sigma_{\text{bi}} c^2}{(4\pi)^3 f_0^2 R_{Tx}^2 R_{Rx}^2} SNR_i, \tag{5.30}$$

where R_{Tx} is the transmitter-to-target range and R_{Rx} is the target-to-receiver range. Suppose a target has $R_{Tx} = R_{Rx} = 50$ m, then using the radar settings in Table 1 with $SNR_i = 150$ dB, the equivalent SNR_o is 16.88 dB. However, for another target with $R_{Tx} = R_{Rx} = 40$ m, then $SNR_o = 20.75$ dB. Therefore, demonstrating the performance metrics against SNR_i is more convenient as

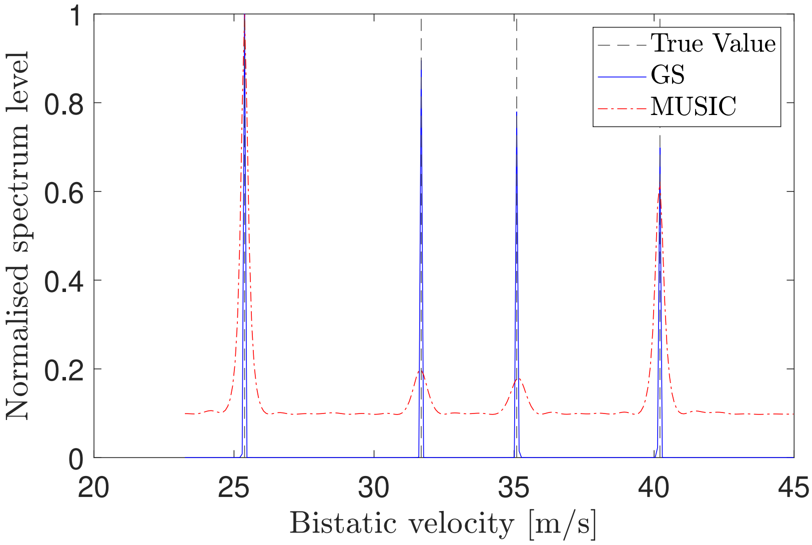

FIGURE 5.5: A comparison of a bistatic velocity spectrum computed for 4 point targets at $SNR_i = 150$ dB with 16 processed snapshots.

targets may have different SNR_0. For parameter association, both proposed methods are compared using the probability defined as the ratio between the number of successful pairings and the total number of trials. The performance metric was measured in three different settings: varying SNR_i, varying estimation error, and varying number of targets.

Consider a scenario where two roadside sensors are employed ($H = 2$), one on each side of a smart highway (see Figure 5.1). For location estimation, the rectangular search grid is generated such that $(x_1, y_1) = (-4, 55)$ and $(x_I, y_J) = (6, 65)$ with $I = J = 21$. For Doppler estimation, $v_{\min} = 25$ and $v_{\max} = 35$ are considered with $G_d = 128$. The known polar coordinates of the roadside sensors are $[(30.00, -7.66), (30.33, 11.41)]$ and the velocity of the sensing vehicle is $v = 25$.

For the sake of clarity, the methods being compared are described as follows.

- GS-Joint estimates the 2D location $(x, k)_k$ from all H received signals simultaneously in line with Algorithm 2.

- GS-Average estimates the bistatic velocity $v_{h,k}$ from each h-th received signal separately in line with Algorithm 2. Assuming perfect parameter association, the target velocity v_k is then calculated followed by averaging.

- MUSIC-Average estimates 2D location $(x, k)_k$ and bistatic velocity $v_{h,k}$ from each of the H received signals separately using MUSIC. Its implementation follows the same steps as Algorithm 2 with Step 5 being replaced by estimating the location-MUSIC spectrum using $\mathbf{P}_{\mathbf{g},h}$, and Step 11 being replaced by estimating the Doppler-MUSIC spectrum using $\mathbf{V}_{\mathbf{g},h}$. Assuming perfect parameter association, the target velocity v_k is then calculated followed by averaging.

- Pair-CC-ESPRIT pairs the location and bistatic velocity parameters in line with the method in Section 5.3.4.

- Pair-LS pairs the location and bistatic velocity parameters in line with the method in Section 5.3.5.

In Figure 5.4 the result of 2D localisation is shown for a scenario with four evenly spaced targets at $SNR_i = 150$ dB with 8 processed pulses. It can be seen that the MUSIC-based method fails to detect two of the targets with the location of the detected ones clearly smeared. On the contrary, the GS-based method results in sharp detected peaks. In Figure 5.5 the estimated bistatic velocity spectrum from 16 processed snapshots for this scenario is shown. The GS-based method clearly yields a better result. The running time for the MUSIC-based method is 1.56 seconds and that of the proposed method is 40.17 seconds. The computer used is powered by an 11th Gen Intel(R) Core(TM) i5-1145G7 chip (2.60 GHz base frequency) and carries 8.00 GB of RAM[1].

5.4.1 Comparison of RMSE for Parameter Estimation

1000 Monte Carlo trials are carried out to compute the RMSE performance. In each trial, a different realisation of the noise signal $\mathbf{W}_h$ is generated. One point-like target is placed in the visible region of the sensing vehicle ($K = 1$), and its parameters $(x, y)_k$ and $v_{h,k}$ are drawn from a uniform distribution bounded by two adjacent grid points from their corresponding search grids.

Firstly, the numbers of pulses and snapshots processed for location and Doppler estimation are chosen as 8 and 16, respectively, and SNR_i is varied. The results are shown in Figure 5.6. It is evident that GS-Joint outperforms MUSIC-Average at all levels of SNR_i in both location and Doppler estimation.

---

[1] Note that the time consumed by the proposed method could be significantly reduced if with a dedicated GS-based algorithm instead of the existing convex optimisation toolbox, which will be considered in future work

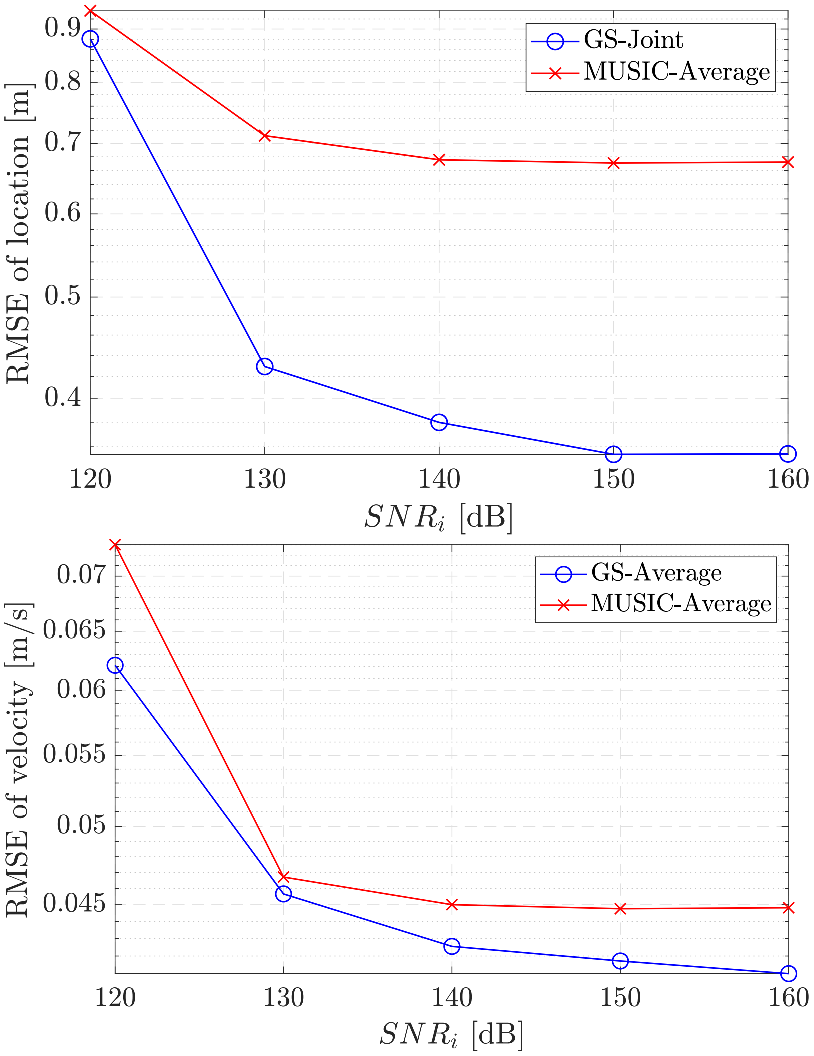

FIGURE 5.6: A comparison of RMSE for location (top) and velocity (bottom) estimation between GS and MUSIC against different levels of SNR_i.

Next, the number of processed pulses for location estimation is varied between 2 and 8, and the number of processed snapshots for Doppler estimation is varied between 4 and 16, with SNR_i being fixed at 150 dB. The results are shown in Figure 5.7. As the number of pulses/snapshots increases, the estimation performance of the proposed method is improved. For all parameters being evaluated, the GS-based method outperforms MUSIC.

5.4.2 Comparison of the Probability for Parameter Association

In each trial, the estimated target location and velocity to be used in the pairing methods is randomly selected from a Gaussian distribution with the

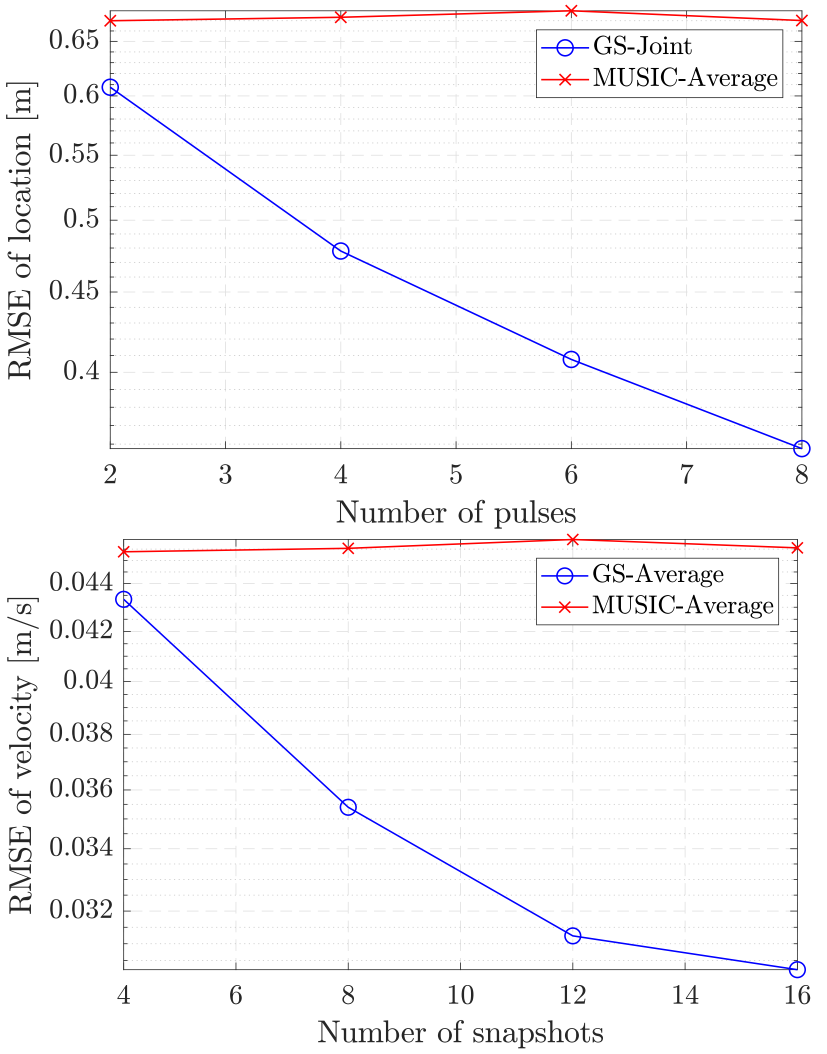

FIGURE 5.7: A comparison of RMSE for location (top) and velocity (bottom) estimation between GS and MUSIC as the number of processed pulses/snapshots increases ($SNR_i = 150$ dB).

mean being the true value and the standard deviation σ_e ranging from 0 to 0.5. A different realisation of $\mathbf{W}_h$ is generated in each trial and data from only one roadside sensor is considered.

Firstly, two targets are considered with varied SNR_i. The results are shown in Figure 5.8. Pair-LS clearly outperforms Pair-CC-ESPRIT with the latter performing similarly only when SNR_i is above 150 dB and σ_e is below 0.1.

Next, the number of targets is varied and the SNR_i is fixed at 160 dB. The results are shown in Figure 5.9. Again, Pair-LS clearly outperforms Pair-CC-ESPRIT with the latter performing similarly only when $K = 2$ and $\sigma_e \leq 0.1$.

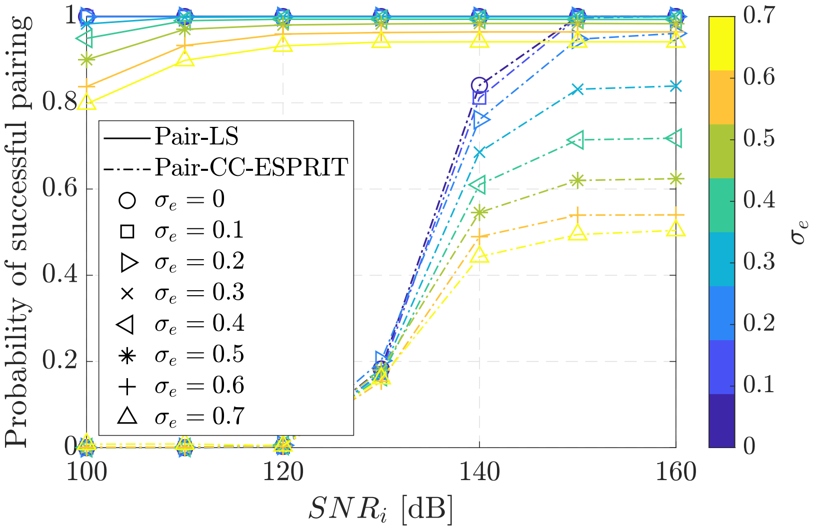

FIGURE 5.8: A comparison of the probability of successful pairing between Pair-LS and Pair-CC-ESPRIT against different levels of SNR_i ($K = 2$).

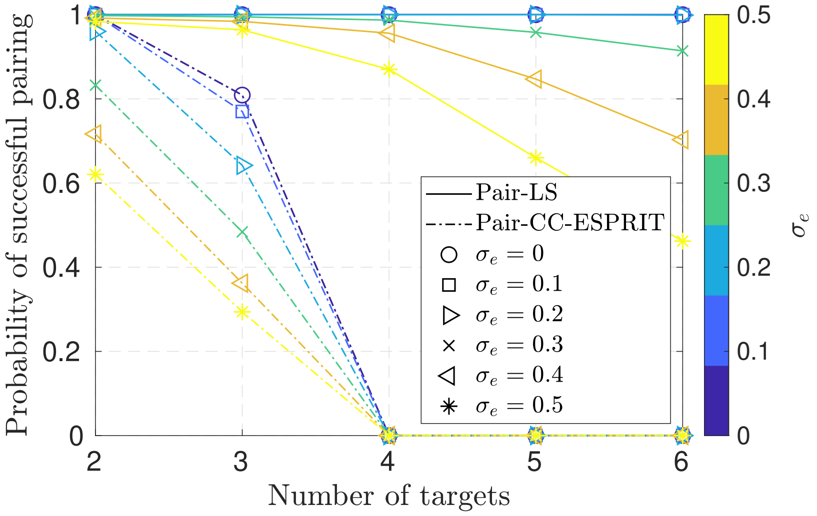

FIGURE 5.9: A comparison of the probability of successful pairing between Pair-LS and Pair-CC-ESPRIT as the number of targets increases ($SNR_i = 160$ dB).

5.5 Summary

In this Chapter, a sparsity-based approach for multistatic automotive localisation was derived. The need for fusing information from multiple sources at the data level was emphasised. The current state-of-art estimation techniques used in the automotive radar industry fail to fulfil such requirements. By employing the GS concept, a method for target location and Doppler estimation was proposed which increases the DoFs and allows information fusion at the data level. Since the natural solution for this application leads to decoupled localisation followed by Doppler estimation, two methods for parameter association were proposed: one relies on the CC between the antenna and pulse domains to match the DOA and bistatic velocity parameters; and the other relies on the whole signal to pair the location and bistatic velocity parameters for all targets simultaneously in an LS-based approach. Computer simulations were conducted to evaluate the performance and verify the effectiveness of the proposed methods. It was shown that GS-based parameter estimation clearly outperforms MUSIC under different settings. The pairing methods also showed evident success in data association under different settings. Bearing the computational cost associated with GS-based optimisation and the LS-based parameter association approach, their attractive performance encourages more research in such advanced signal processing techniques. Bearing the computational cost associated with GS-based optimisation, it is well suited for the wideband problem where multiple frequencies are combined through structured sparsity. So, this research area is explored in the next Chapter.

Chapter 6

Wideband Bistatic Automotive Radar

6.1 Introduction

Wideband signals can theoretically improve the performance of radar systems particularly for parameter estimation but processing such signals carries a huge computational cost mainly due to the increased data size [182]. Nevertheless, signal processing techniques are often developed under narrowband assumptions for feasible and practical implementation. When such assumptions are broken, more complex solutions are often required [120].

The motivation behind extending the automotive bistatic radar application to the wideband framework is driven by both the advantages and challenges of wideband radar. Such advantages are well documented in the literature [183, 184, 185], and include increased detection accuracy and resolution, improved target identification and feature extraction, higher probability of detection, added immunity and secretiveness, as well as reduced dead zones. On the other hand, processing wideband signals requires complex and novel techniques for detection, ranging, and direction finding, and significantly increases the memory and computing load. Furthermore, the increased accuracy and resolution comes at a cost of increased captured clutter and degraded coherence of detection especially in the presence of moving targets. Fortunately, any attempts at tackling these challenging is incredibly rewarding as it unlocks masses of potential for automotive radar applications.

In this Chapter, the current understanding of wideband automotive radar is furthered by deriving a rigorous wideband FMCW signal model based on the proposed bistatic automotive application. The unwanted artefacts associated with this problem are identified to explicitly highlight the areas where conventional narrowband estimation techniques fail. Some artefacts that are often neglected in the wideband radar literature are considered. In order to devise a new criterion under which narrowband assumptions are no longer valid, upper bounds on bandwidth are derived for each measurement domain. Then, a general approach for resolving the unwanted artefacts is proposed by decoupling the range, Doppler, and DOA estimation tasks. The proposed solution can be applied to different parametric approaches and regarded as a systematic method where either subspace or GS-based algorithms can be used. However, after proving in the previous Chapters that sparsity-based methods can outperform subspace-based estimation techniques, a three-stage method is proposed by employing the GS concept for decoupled wideband range, Doppler, and DOA estimation. It is shown that the unambiguous data association can be achieved without a noticeable increase in the computational cost.

In the rest of this Chapter, a wideband bistatic FMCW signal model is derived in Section 6.2 where the unwanted wideband artefacts are analysed and bandwidth bounds are derived for wideband FMCW radar. After that, an approach for resolving the unwanted artefacts through decoupled estimation is proposed in Section 6.3 followed by a three-stage GS-based algorithm for wideband range, Doppler and DOA estimation. Finally, simulation results are presented in Section 6.4 and a summary is given in Section 6.5.

6.2 Wideband Bistatic FMCW Signal Model

Suppose the roadside sensor is transmitting wideband chirps and the direct-path signals are removed. By recalling (3.21), the signal received from the k-th target at the l-th antenna can be written as

$$r_{h,k}(l,m,t_f) = A_{h,k}\exp\{j2\pi\varphi_{h,k}(m,t_f)\}\exp\{-j2\pi\Theta_{h,k}(l,m,t_f)\}, \tag{6.1}$$

where

$$\varphi_{h,k}(m,t_f) = f_0(t_f - \tau_{h,k}(m,t_f)) + 0.5\mu(t_f - \tau_{h,k}(m,t_f))^2 \tag{6.2}$$

is the phase of the received signal at the 0-th antenna and

$$\Theta_{h,k}(l,m,t_f) = \frac{f_{h,k}(m,t_f)d\sin\theta_k}{c}l \tag{6.3}$$

is the phase delay relative to the 0-th antenna with $f_{h,k}(m,t_f)$ being the instantaneous frequency of the received signal. It can then be extracted as

$$\begin{aligned} f_{h,k}(m,t_f) &= \frac{d\varphi_{h,k}(m,t_f)}{dt_f} \\ &= f_0\left(1-\frac{d\tau_{h,k}(m,t_f)}{dt_f}\right) + \mu(t_f-\tau_{h,k}(m,t_f))\left(1-\frac{d\tau_{h,k}(m,t_f)}{dt_f}\right) \\ &\approx f_0 - \frac{f_0 v_{h,k}}{c} - \frac{\mu \acute{R}_{h,k}}{c} + \mu t_f. \end{aligned} \tag{6.4}$$

By plugging (6.4) in (6.3) and following the same dechirp process as in (3.25) and (3.26), the sampled dechirped radar signal can then be written as

$$\begin{aligned} & y_h^{\S}(l,m,n) \\ &= \sum_{k=1}^{K} q_{h,k} \exp\{-j2\pi(\overbrace{(f^r_{h,k}+f^d_{h,k})\frac{n}{f_s}}^{1} + f^d_{h,k}mT + \overbrace{\frac{\mu v_{h,k}T}{c}\frac{n}{f_s}m}^{2})\} \\ &\quad \times \exp\{-j2\pi(\underbrace{(f_0-f^r_{h,k}-f^d_{h,k})\frac{d\sin\theta_k}{c}}_{3} l + \underbrace{\frac{\mu d\sin\theta_k}{c}\frac{n}{f_s}}_{4} l)\} + w_h^{\S}[l,m,n], \end{aligned} \tag{6.5}$$

where $f^r_{h,k} = \frac{\mu \acute{R}_{h,k}}{c}$ is the range dependant frequency, $f^d_{h,k} = \frac{f_0 v_{h,k}}{c}$ is the Doppler frequency, and $w_h^{\S}[l,m,n]$ is AWGN.

Consider the following matrices containing the range, Doppler, and DOA information, respectively, as

$$\mathbf{R}^{\S}_{h,k} = \begin{bmatrix} 1 & 1 & \cdots & 1 \\ 1 & e^{-j2\pi(f^r_{h,k}+f^d_{h,k}+\frac{\mu v_{h,k}T}{c})(\frac{1}{f_s})} & \cdots & e^{-j2\pi(f^r_{h,k}+f^d_{h,k}+\frac{\mu v_{h,k}T(M-1)}{c})(\frac{1}{f_s})} \\ \vdots & \vdots & \ddots & \vdots \\ 1 & e^{-j2\pi(f^r_{h,k}+f^d_{h,k}+\frac{\mu v_{h,k}T}{c})(\frac{N-1}{f_s})} & \cdots & e^{-j2\pi(f^r_{h,k}+f^d_{h,k}+\frac{\mu v_{h,k}T(M-1)}{c})(\frac{N-1}{f_s})} \end{bmatrix}, \tag{6.6}$$

$$\mathbf{V}^{\S}_{h,k} = \begin{bmatrix} 1 & 1 & \cdots & 1 \\ 1 & e^{-j2\pi(f^d_{h,k}+\frac{\mu v_{h,k}T}{cf_s})} & \cdots & e^{-j2\pi(f^d_{h,k}+\frac{\mu v_{h,k}T}{cf_s}(N-1))} \\ \vdots & \vdots & \ddots & \vdots \\ 1 & e^{-j2\pi(f^d_{h,k}+\frac{\mu v_{h,k}T}{cf_s})(M-1)} & \cdots & e^{-j2\pi(f^d_{h,k}+\frac{\mu v_{h,k}T}{cf_s}(N-1))(M-1)} \end{bmatrix}, \tag{6.7}$$

and

$$\mathbf{A}^{\S}_{h,k}=\begin{bmatrix}1 & 1 & \cdots & 1\\ 1 & e^{-j2\pi(\frac{f^a_{h,k}d\sin\theta_k}{c}+\frac{\mu d\sin\theta_k}{cf_s})} & \cdots & e^{-j2\pi(\frac{f^a_{h,k}d\sin\theta_k}{c}+\frac{\mu d\sin\theta_k}{cf_s}(N-1))}\\ \vdots & \vdots & \ddots & \vdots\\ 1 & e^{-j2\pi(\frac{f^a_{h,k}d\sin\theta_k}{c}+\frac{\mu d\sin\theta_k}{cf_s})(L-1)} & \cdots & e^{-j2\pi(\frac{f^a_{h,k}d\sin\theta_k}{c}+\frac{\mu d\sin\theta_k}{cf_s}(N-1))(L-1)}\end{bmatrix}, \tag{6.8}$$

where $f^a_{h,k}=f_0-f^r_{h,k}-f^d_{h,k}$. Firstly, consider the fast time against the slow time in (6.5). The received signal from the m-th chirp can be written as

$$\mathbf{Z}^{\S}_{\mathbf{r},h}[m]=\mathbf{R}^{\S}_{h}[m]\mathbf{x}^{\S}_{\mathbf{r},h}[m]+\mathbf{w}^{\S}_{\mathbf{r},h}[m]\quad\in\mathbb{C}^{N\times 1}, \tag{6.9}$$

where $\mathbf{R}^{\S}_{h}[m]=[\mathbf{R}^{\S}_{h,1}[m],\mathbf{R}^{\S}_{h,2}[m],\ldots,\mathbf{R}^{\S}_{h,K}[m]]\in\mathbb{C}^{N\times K}$,

$$\mathbf{x}^{\S}_{\mathbf{r},h}[m]=[e^{-j2\pi f^d_{h,1}m}q_{h,1},e^{-j2\pi f^d_{h,2}m}q_{h,2}\ldots,e^{-j2\pi f^d_{h,K}m}q_{h,K}], \tag{6.10}$$

and $\mathbf{w}^{\S}_{\mathbf{r},h}[m]\in\mathbb{C}^{N\times 1}$ is AWGN.

Then, consider the slow time against the fast time. The received signal from the n-th snapshot can be written as

$$\mathbf{Z}^{\S}_{\mathbf{v},h}[n]=\mathbf{V}^{\S}_{h}[n]\mathbf{x}^{\S}_{\mathbf{v},h}[n]+\mathbf{w}^{\S}_{\mathbf{v},h}[n]\quad\in\mathbb{C}^{M\times 1}, \tag{6.11}$$

where $\mathbf{V}^{\S}_{h}[n]=[\mathbf{V}^{\S}_{h,1}[n],\mathbf{V}^{\S}_{h,2}[n],\ldots,\mathbf{V}^{\S}_{h,K}[n]]\in\mathbb{C}^{M\times K}$,

$$\mathbf{x}^{\S}_{\mathbf{v},h}[n]=[e^{-j2\pi(f^r_{h,1}+f^d_{h,1})\frac{n}{f_S}}q_{h,1},e^{-j2\pi(f^r_{h,2}+f^d_{h,2})\frac{n}{f_S}}q_{h,2}\ldots,e^{-j2\pi(f^r_{h,K}+f^d_{h,K})\frac{n}{f_S}}q_{h,K}], \tag{6.12}$$

and $\mathbf{w}^{\S}_{\mathbf{v},h}[n]\in\mathbb{C}^{M\times 1}$ is AWGN.

Finally, consider the antenna domain against the fast time. The received signal for the n-th snapshot can be written as

$$\mathbf{Z}^{\S}_{\mathbf{a},h}[n]=\mathbf{A}^{\S}_{h}[n]\mathbf{x}^{\S}_{\mathbf{a},h}[n]+\mathbf{w}^{\S}_{\mathbf{a},h}[n]\quad\in\mathbb{C}^{L\times 1}, \tag{6.13}$$

where $\mathbf{A}^{\S}_{h}[n]=[\mathbf{A}^{\S}_{h,1}[n],\mathbf{A}^{\S}_{h,2}[n],\ldots,\mathbf{A}^{\S}_{h,K}[n]]\in\mathbb{C}^{L\times K}$, $\mathbf{x}^{\S}_{\mathbf{a},h}[n]=\mathbf{x}^{\S}_{\mathbf{v},h}[n]$, and $\mathbf{w}^{\S}_{\mathbf{a},h}[n]\in\mathbb{C}^{L\times 1}$ is AWGN.

6.2.1 Analysis of the Unwanted Wideband Artefacts

The artefacts associated with the signal model in (6.5) are next discussed.

1. The fast-time domain in reality contains Doppler information as well as range information which is shown in the summation of both frequencies in term {1}. This artefact is not particularly caused by the increase in bandwidth of the transmitted signal but may cause some bias in the range estimate when the frequency and velocity are large enough. The effect of this Doppler shift on range estimation becomes critical once it exceeds the resolution in fast-time which can be defined for Rayleigh estimation as $\delta f^r = \frac{1}{T_c}$.

   In practice, the bias caused by this Doppler shift on the range estimate can be corrected following Doppler estimation.

2. In term {2} in (6.5), the artefact is concluded by a coupling between the fast-time and slow-time domains. This degrades the orthogonality between the two domains and is responsible for the well-known *range walk* phenomenon [186, 187, 188]. In other words, between multiple transmitted chirps, the tracked target travels a distance larger than the conventional range-FFT bin. Consequently, the spikes in a range-Doppler map would look smeared translating to estimation error and degradation in resolution and SNR. Also referred to as range migration, this problem was studied extensively in the literature in various schemes. The Keystone algorithm is a popular method for solving range migration and it emerged in SAR imaging [189], and an application of it to automotive wideband radar can be found in [190]. It is shown that no prior knowledge of the Doppler frequencies or the number of scatterers is required. Basically, one-dimensional interpolation is applied in the domain of interest and the cross-coupling term {4} is removed. The disadvantage of Keystone transforms is that they require a very large sample size and in many occasions oversampling to overcome interpolation errors and to avoid ghost targets [191]. Another method for solving migration problems is the Back-Focusing method, tested in [192] using real radar data and compared to the Keystone method. It is not affected by interpolation and provides a better performance at a cost of higher computational complexity. Also, there is no proof that it can be used in multi-target scenarios. Recently, [193] proposed an FFT-based approach to solve the effect of the migration in range-Doppler mapping of wideband radar. This works by first locating the smeared peaks in the range-Doppler FFT map, and then the velocities are recorded and compensated for migration. Using the tuned

velocities, the smeared energy in multiple range cells is removed (the peaks are sharpened), and then Sinc interpolation is finally applied to correct the amplitude of the sharpened peaks. The main drawback of this method is that it assumes that all targets are visible in the original range-Doppler map. However, targets of varying intensities are affected differently by migration and can in many cases become undetected if the smearing power surpasses the noise floor.

3. The term {3} in (6.5) represents a shift in the frequency inside the phase progression term across the antenna domain used for DOA estimation. This frequency shift caused by the trip delay and Doppler effect, with the range dependant frequency having the more significant effect, is independent of time. To the best of our knowledge, this artefact has not been previously identified. While this frequency shift, typically $\sim$ 50-100 MHz for automotive applications, may seem insignificant compared to f_0, it is key for high resolution radar imagery to understand such artefact and devise solutions for better estimation performance.

4. The term {4} in (6.5) represents the wideband problem in DOA estimation where the DOA dependant phase shift in the fast time is no longer negligible as the bandwidth increases. This term then deviates the target from its true bearing as the observation period increases and requires compensation for accurate DOA estimation. The two mainstreams for solving this problem include the incoherent signal subspace method (ISSM) [194, 195] and the coherent signal subspace method (CSSM) [196, 197]. These two methods convert the wideband problem into a narrowband one while harnessing the benefits of the increasing bandwidth. ISSM decomposes the output of the antenna array into multiple sub-arrays and applies a form of filter bank and therefore solve the DOA problem for each channel separately. Although no initial estimate of DOA is required (which usually hinders convergence), channels with poor SNR can severely degrade the overall accuracy after averaging as the total signal power is not exploited here. CSSM on the other hand, converts the covariance matrices of all the signal subspace into a signal subspace of essentially one frequency via focusing matrices, and then conventional narrowband DOA estimation is applied. [198] shows that CSSM outperforms ISSM as the focused matrices preserve the SNR of the sub-bands; however the computational complexity of forming these matrices is very large and, they require an initial

estimate of the true DOAs which can affect the performance [199].

Similar to the multiple-snapshot case of DOA estimation under the CS framework, the wideband case can be treated as a structured sparsity problem [59]. The steering matrix becomes a block diagonal matrix with each block corresponding to a different frequency. This approach leads to significant improvement in performance with some added computational cost. More recently, [50] proposed solving the wideband DOA estimation problem by applying a matched filter (a phase compensation step) to each grid point in the DOA region before estimating the signal subspace of the signal. This work was applied to joint Doppler-DOA estimation and claimed the ability of applying the algorithm to range-Doppler/DOA processing. The computational complexity is still very large in this proposed method even after efficient implementation of parallel processing and accelerated EVD. Also, extending this method to range processing means that the matched filter applied to the DOA domain will inevitably reduce the resolution and accuracy of the estimated range.

6.2.2 Bandwidth Bounds for Wideband FMCW Radar

Under narrowband signal assumptions, the terms {2} and {4} in (6.5) are normally neglected. Knowing they are dependant on the bandwidth B, it is useful to derive upper bounds that define the bandwidth above which the narrowband assumptions may fail. In the following derivations, joint parameter estimation is assumed in line with the implementation of the signal model in Chapter 4. For simplicity of notation, the subscripts h and k are omitted.

Fast-time Domain

In the fast-time domain, the frequency progression across the N samples allows estimating the bistatic range parameter R. By taking the coupling terms {2} and {4} in (6.5) into account and ignoring the Doppler shift inside term {1}, the fast-time progression term becomes

$$\rho(l,m,n) = \left(\frac{\mu R}{c} + \frac{\mu v T}{c}m + \frac{\mu d \sin\theta}{c}l\right)\frac{n}{f_s} = \frac{\mu}{c}(R + vmT + d\sin\theta l)\frac{n}{f_s} \tag{6.14}$$

Then, the maximum bias in the estimated range can be defined as

$$R_{\text{bias,max}} = v_{\max}(M-1)T + \max_{d,\theta}\{d|\sin\theta|\}(L-1), \tag{6.15}$$

where v_{max} is the maximum bistatic velocity and $\max\{d|\sin\theta|\}$ can defined, by taking into account the Nyquist requirements in a ULA, as

$$\max_{d,\theta}\{d|\sin\theta|\} = \frac{c}{2f_0}. \tag{6.16}$$

The maximum bias can now be expressed

$$R_{\text{bias,max}} = v_{\text{max}}(M-1)T + \frac{c(L-1)}{2f_0}. \tag{6.17}$$

The range bias may be neglected when

$$R_{\text{bias,max}} < \delta R_{\text{max}}/2, \tag{6.18}$$

where δR_{max} is the maximum bistatic range resolution which can be defined using the Rayleigh criterion as

$$\delta R_{\text{max}} = \frac{c}{B} - \frac{v_{\text{max}} f_0 T_c}{B}. \tag{6.19}$$

By substituting (6.17) and (6.19) in (6.18), the bandwidth upper bound can be defined as

$$\beta_r = \frac{f_0(c - f_0 v_{\text{max}} T_c)}{2v_{\text{max}}(M-1)f_0 T + c(L-1)}. \tag{6.20}$$

According to the Nyquist theorem, $v_{\text{max}} = \frac{c}{2Tf_0}$ and β_r reduces to

$$\beta_r = \frac{f_0(1 - \frac{T_c}{2T})}{L+M-2}. \tag{6.21}$$

Slow-time Domain

In the slow-time domain, the phase progression across the M chirps allows estimating the bistatic velocity parameter v. By taking the coupling term {2} in (6.5) into account, the slow-time progression term becomes

$$\nu(m,n) = (\frac{f_0 v T}{c} + \frac{\mu v T}{c}\frac{n}{f_s})m = \frac{f_0 T}{c}(v + \frac{\mu v}{f_0}\frac{n}{f_s})m. \tag{6.22}$$

Then, the maximum bias in the estimated bistatic velocity can be defined as

$$v_{\text{bias,max}} = \frac{B v_{\text{max}}}{f_0}. \tag{6.23}$$

The bistatic velocity bias may be neglected when

$$v_{\text{bias,max}} < \delta v_{\max}/2, \tag{6.24}$$

where $\delta v_{\max}$ is the maximum bistatic velocity resolution which can be defined using the Rayleigh criterion as

$$\delta v_{\max} = \frac{c}{f_0 MT}. \tag{6.25}$$

By substituting (6.23) and (6.25) in (6.24), the bandwidth upper bound can be defined as

$$\beta_v = \frac{c}{2v_{\max}MT} = \frac{f_0}{M}. \tag{6.26}$$

Antenna Domain

In the antenna domain, the phase progression across L antennas allows estimating the DOA parameter θ. By taking the coupling term {4} in (6.5) into account and ignoring the effect of the shift in the centre frequency in term {3}, the antenna progression term becomes

$$\begin{aligned} o(l,n) &= (\frac{f_0 d \sin\theta}{c} + \frac{\mu d \sin\theta}{c}\frac{n}{f_s})l \\ &= \frac{f_0 d}{c}(\sin\theta + \frac{\mu\sin\theta}{f_0}\frac{n}{f_s})l. \end{aligned} \tag{6.27}$$

Then, the bias in the estimated DOA can be defined as

$$\theta_{\text{bias}}(\theta) = \arcsin(\frac{B\sin\theta}{f_0}). \tag{6.28}$$

The DOA bias may be neglected when

$$\theta_{\text{bias}}(\theta) < \delta\theta(\theta)/2, \tag{6.29}$$

where $\delta\theta(\theta)$ is the DOA resolution which can be defined using the Rayleigh criterion as

$$\delta\theta(\theta) = \frac{2}{L\cos\theta}. \tag{6.30}$$

The minimal distance between $\theta_{\text{bias}}(\theta)$ and $\delta\theta(\theta)$ is when $\theta = 45°$. So, by substituting (6.28) and (6.30) in (6.29), the bandwidth upper bound can be defined when $\theta = 45°$ as

$$\beta_\theta = \sqrt{2} f_0 \sin(\frac{2\sqrt{2}}{L}). \tag{6.31}$$

6.3 Wideband Motion Parameter Estimation using GS

6.3.1 Resolving the Unwanted Artefacts through Decoupled Estimation

When jointly estimating the range, Doppler, and DOA parameters, the artefacts in terms {1} and {3} are naturally solved. However, the size of the measurement signal increases dramatically in the wideband case and applying a 3D parametric search becomes impractical. Also, with joint estimation, filtering out the coupling terms {2} and {4} requires applying a phase compensation for every entry in the Doppler and DOA search grids which is computationally exhaustive. Therefore, to reduce the computational complexity and resolve the unwanted artefacts, a decoupled estimation method is proposed as illustrated in the following steps:

1. Since the slow-time progression term only contains Doppler information, it is convenient to first estimate the bistatic velocity from (6.11) through a 1D search grid. Therefore, Doppler steering matrices are constructed using $\mathbf{V}^{\S}_{h,k}$ for the selected snapshots, which directly solves the coupling problem and incorporates the term {2} in (6.5) as extra information about the target without the need of compensating for it through matched filtering. The same steering matrices can also be used for the signals from multiple antennas knowing that there is no coupling between the slow-time and antenna domains.

2. In the second stage, a 1D bistatic range search grid is defined then bistatic range estimation is done for each estimated bistatic velocity. Without prior knowledge of the DOAs of the targets, only the signals from the first antenna are used (i.e. (6.9)) to avoid the effects of the DOA dependant coupling term {4}. So, for K targets, range estimation is repeated K times. In each iteration, the k-th estimated bistatic velocity is used to construct the range steering matrices for the selected chirps using $\mathbf{R}^{\S}_{h,k}$. In each iteration, the range spectrum might show multiple

peaks corresponding to other targets. This is due to the fact that while the steering matrices are designed to remove the effect of coupling and focus the peak for the k-th target being processed, they do not necessarily suppress the energy from other targets. To resolve this problem, an approach is proposed using the CLEAN technique [200] and processing the targets in a descending order of intensity. To illustrate this, the target with the largest amplitude in the Doppler estimation stage is first processed. With the steering matrices constructed using the estimated bistatic velocity for this target, the largest peak in the estimated range spectrum is chosen and correct parameter pairing is realised. Then, the signal corresponding to this target is reconstructed from the estimated bistatic range and velocity and removed from the original signal before processing the next target.

3. Finally, for DOA estimation, a 1D search grid is defined. For each estimated range-Doppler pair, DOA steering matrices are constructed for the selected snapshots using $\mathbf{A}^{\S}_{h,k}$. In order to choose the correct peak in the DOA spectrum corresponding to the target being processed, a maximum-likelihood approach can be implemented without significantly increasing the computational cost. It follows that the combination of the estimated range, Doppler, and DOA parameters that minimises the distance between the raw signal (containing the energy from all targets) and that constructed from it for the k-th target is the correct one, which concludes the pairing process.

6.3.2 A Three-stage Wideband GS-based Range, Doppler, and DOA Estimation

For Doppler estimation, recall the reshaped signal in (6.11). To introduce sparsity in the Doppler domain, a search grid is defined of length G_v with all the potential bistatic velocities to estimate $v_{h,k}$. Accordingly, a Doppler steering matrix is constructed for the n-th snapshot by replacing $v_{h,k}$ with v_{h,g_v} in $\mathbf{V}^{\S}_{h}[n]$ to get $\mathbf{V}^{\S}_{\mathbf{g},h}[n] \in \mathbb{C}^{M\times G_v}$. Following such representation, $\mathbf{Z}^{\S}_{\mathbf{v},h}[n]$ can now be written in a sparse format for the n-th snapshot as

$$\mathbf{Z}^{\S}_{\mathbf{v},h}[n] = \mathbf{V}^{\S}_{\mathbf{g},h}[n]\mathbf{x}^{\S}_{\mathbf{gv},h}[n] + \mathbf{w}^{\S}_{\mathbf{v},h}[n], \tag{6.32}$$

where $\mathbf{x}^{\S}_{\mathbf{gv},h}[n] \in \mathbb{C}^{G_v\times 1}$ is a sparse data vector containing K non-zero entries corresponding to the complex coefficients of the targets. So, the concept of GS can be employed across N snapshots by generating an $M \times N$ measurement matrix $\mathbf{B}^{\S}_{\mathbf{v},h}$ and a $G_v \times N$ sparse data matrix $\mathbf{U}^{\S}_{\mathbf{v},h}$ as

$$\mathbf{B}^{\S}_{\mathbf{v},h} = \left[\mathbf{V}^{\S}_{\mathbf{g},h}[0]\mathbf{x}^{\S}_{\mathbf{gv},h}[0], \mathbf{V}^{\S}_{\mathbf{g},h}[1]\mathbf{x}^{\S}_{\mathbf{gv},h}[1], \dots, \mathbf{V}^{\S}_{\mathbf{g},h}[N-1]\mathbf{x}^{\S}_{\mathbf{gv},h}[N-1]\right], \quad (6.33)$$

and

$$\mathbf{U}^{\S}_{\mathbf{v},h} = \left[\mathbf{x}^{\S}_{\mathbf{gv},h}[0], \mathbf{x}^{\S}_{\mathbf{gv},h}[1], \dots, \mathbf{x}^{\S}_{\mathbf{gv},h}[N-1]\right]. \quad (6.34)$$

Then, Doppler estimation is done by solving the following optimisation problem

$$\min_{\mathbf{U}^{\S}_{\mathbf{v},h}} \quad \|\mathbf{U}^{\S}_{\mathbf{v},h}\|_{2,1} \quad \text{subject to} \quad \|\mathbf{Z}^{\S}_{\mathbf{v},h} - \mathbf{B}^{\S}_{\mathbf{v},h}\|_F \leq \varepsilon_4, \quad (6.35)$$

where

$$\mathbf{Z}^{\S}_{\mathbf{v},h} = [\mathbf{Z}^{\S}_{\mathbf{v},h}[0], \mathbf{Z}^{\S}_{\mathbf{v},h}[1], \dots, \mathbf{Z}^{\S}_{\mathbf{v},h}[N-1]] \quad (6.36)$$

and ε_4 is the reconstruction error.

For range estimation, recall the reshaped signal in (6.9). To introduce sparsity in the range domain, a search grid is defined of length G_r with all the potential bistatic range parameters to estimate $\acute{R}_{h,k}$. Accordingly, a range steering matrix is constructed for the m-th chirp by replacing $\acute{R}_{h,k}$ with R_{h,g_r} in $\mathbf{R}^{\S}_{h}[m]$ to get $\mathbf{R}^{\S}_{\mathbf{g},h}[m] \in \mathbb{C}^{N \times G_r}$. Following such representation, $\mathbf{Z}^{\S}_{\mathbf{r},h}[m]$ can now be written in a sparse format for the m-th chirp as

$$\mathbf{Z}^{\S}_{\mathbf{r},h}[m] = \mathbf{R}^{\S}_{\mathbf{g},h}[m]\mathbf{x}^{\S}_{\mathbf{gr},h}[m] + \mathbf{w}^{\S}_{\mathbf{r},h}[m], \quad (6.37)$$

where $\mathbf{x}^{\S}_{\mathbf{gr},h}[m] \in \mathbb{C}^{G_r \times 1}$ is a sparse data vector containing K non-zero entries corresponding to the complex coefficients of the targets. So, the concept of GS can be employed across M chirps by generating an $N \times M$ measurement matrix $\mathbf{B}^{\S}_{\mathbf{r},h}$ and a $G_r \times M$ sparse data matrix $\mathbf{U}^{\S}_{\mathbf{r},h}$ as

$$\mathbf{B}^{\S}_{\mathbf{r},h} = \left[\mathbf{R}^{\S}_{\mathbf{g},h}[0]\mathbf{x}^{\S}_{\mathbf{gr},h}[0], \mathbf{R}^{\S}_{\mathbf{g},h}[1]\mathbf{x}^{\S}_{\mathbf{gr},h}[1], \dots, \mathbf{R}^{\S}_{\mathbf{g},h}[M-1]\mathbf{x}^{\S}_{\mathbf{gr},h}[M-1]\right], \quad (6.38)$$

and

$$\mathbf{U}^{\S}_{\mathbf{r},h} = \left[\mathbf{x}^{\S}_{\mathbf{gr},h}[0], \mathbf{x}^{\S}_{\mathbf{gr},h}[1], \dots, \mathbf{x}^{\S}_{\mathbf{gr},h}[M-1]\right]. \quad (6.39)$$

Then, range estimation is done by solving the following optimisation problem

$$\min_{\mathbf{U}^{\S}_{\mathbf{r},h}} \quad \|\mathbf{U}^{\S}_{\mathbf{r},h}\|_{2,1} \quad \text{subject to} \quad \|\mathbf{Z}^{\S}_{\mathbf{r},h} - \mathbf{B}^{\S}_{\mathbf{r},h}\|_F \leq \varepsilon_5, \quad (6.40)$$

where

$$\mathbf{Z}^{\S}_{\mathbf{r},h} = [\mathbf{Z}^{\S}_{\mathbf{r},h}[0], \mathbf{Z}^{\S}_{\mathbf{r},h}[1], \ldots, \mathbf{Z}^{\S}_{\mathbf{r},h}[M-1]] \tag{6.41}$$

and ε_5 is the reconstruction error.

For DOA estimation, recall the reshaped signal in (6.13). To introduce sparsity in the DOA domain, a search grid is defined of length G_a with all the potential DOAs to estimate θ_k. Accordingly, a DOA steering matrix is constructed for the n-th snapshot by replacing θ_k with θ_{g_a} in $\mathbf{A}^{\S}_{h}[n]$ to get $\mathbf{A}^{\S}_{\mathbf{g},h}[n] \in \mathbf{C}^{L \times G_a}$. Following such representation, $\mathbf{Z}^{\S}_{\mathbf{a},h}[n]$ can now be written in a sparse format for the n-th snapshot as

$$\mathbf{Z}^{\S}_{\mathbf{a},h}[n] = \mathbf{A}^{\S}_{\mathbf{g},h}[n]\mathbf{x}^{\S}_{\mathbf{ga},h}[n] + \mathbf{w}^{\S}_{\mathbf{a},h}[n], \tag{6.42}$$

where $\mathbf{x}^{\S}_{\mathbf{ga},h}[n] \in \mathbb{C}^{G_a \times 1}$ is a sparse data vector containing K non-zero entries corresponding to the complex coefficients of the targets. So, the concept of GS can be employed across N snapshots by generating an $L \times N$ measurement matrix $\mathbf{B}^{\S}_{\mathbf{a},h}$ and a $G_a \times N$ sparse data matrix $\mathbf{U}^{\S}_{\mathbf{a},h}$ as

$$\mathbf{B}^{\S}_{\mathbf{a},h} = \left[\mathbf{A}^{\S}_{\mathbf{g},h}[0]\mathbf{x}^{\S}_{\mathbf{ga},h}[0], \mathbf{A}^{\S}_{\mathbf{g},h}[1]\mathbf{x}^{\S}_{\mathbf{ga},h}[1], \ldots, \mathbf{A}^{\S}_{\mathbf{g},h}[N-1]\mathbf{x}^{\S}_{\mathbf{ga},h}[N-1]\right], \tag{6.43}$$

and

$$\mathbf{U}^{\S}_{\mathbf{a},h} = \left[\mathbf{x}^{\S}_{\mathbf{ga},h}[0], \mathbf{x}^{\S}_{\mathbf{ga},h}[1], \ldots, \mathbf{x}^{\S}_{\mathbf{ga},h}[N-1]\right]. \tag{6.44}$$

Then, DOA estimation is done by solving the following optimisation problem

$$\min_{\mathbf{U}^{\S}_{\mathbf{a},h}} \quad \|\mathbf{U}^{\S}_{\mathbf{a},h}\|_{2,1} \quad \text{subject to} \quad \|\mathbf{Z}^{\S}_{\mathbf{a},h} - \mathbf{B}^{\S}_{\mathbf{a},h}\|_F \leq \varepsilon_6, \tag{6.45}$$

where

$$\mathbf{Z}^{\S}_{\mathbf{a},h} = [\mathbf{Z}^{\S}_{\mathbf{a},h}[0], \mathbf{Z}^{\S}_{\mathbf{a},h}[1], \ldots, \mathbf{Z}^{\S}_{\mathbf{a},h}[N-1]] \tag{6.46}$$

and ε_6 is the reconstruction error.

When processing targets individually for DOA estimation, it is possible to choose correct peak in the estimated spectrum by adopting a maximum-likelihood approach. Suppose while processing the k-th target that the estimated DOA spectrum contains I peaks (I is used here instead of K to account for ghost targets). By considering the antenna and fast-time domains only, the contribution of the k-th target can be constructed for the i-th DOA candidate as

$$\mathbf{C}_{h,i}^{\S^{(k)}}[n] = \begin{bmatrix} e^{-j2\pi(f_{h,k}^{r}+f_{h,k}^{d})\frac{n}{f_s}} \\ e^{-j2\pi[(\frac{f_{h,k}^{a} d\sin\theta_i}{c}+\frac{\mu d\sin\theta_i}{c}\frac{n}{f_s})+(f_{h,k}^{r}+f_{h,k}^{d})\frac{n}{f_s}]} \\ \vdots \\ e^{-j2\pi[(\frac{f_{h,k}^{a} d\sin\theta_i}{c}+\frac{\mu d\sin\theta_i}{c}\frac{n}{f_s})(L-1)+(f_{h,k}^{r}+f_{h,k}^{d})\frac{n}{f_s}]}. \end{bmatrix} \tag{6.47}$$

Then, a minimisation function is porposed for choosing the correct DOA candidate as

$$\theta_i = \arg\min(\|\mathbf{z}_{\mathbf{a},h}^{\S} - \mathbf{c}_{h,i}^{\S^{(k)}}(\mathbf{c}_{h,i}^{\S^{(k)^H}}\mathbf{c}_{h,i}^{\S^{(k)}})^{-1}\mathbf{c}_{h,i}^{\S^{(k)^H}}\mathbf{z}_{\mathbf{a},h}^{\S}\|_2), \tag{6.48}$$

where $\mathbf{z}_{\mathbf{a},h}^{\S} = \mathrm{vec}\{\mathbf{Z}_{\mathbf{a},h}^{\S}\}$ and $\mathbf{c}_{h,i}^{\S^{(k)}} = \mathrm{vec}\{\mathbf{C}_{h,i}^{\S^{(k)}}\}$ with

$$\mathbf{C}_{h,i}^{\S^{(k)}} = [\mathbf{C}_{h,i}^{\S^{(k)}}[1], \mathbf{C}_{h,i}^{\S^{(k)}}[2], \ldots, \mathbf{C}_{h,i}^{\S^{(k)}}[N-1]]. \tag{6.49}$$

Finally, the proposed method for range, Doppler, and DOA estimation using wideband bistatic measurements is summarised in Algorithm 3.

6.4 Simulation Results

Computer simulations were conducted to verify the success of the proposed GS-based wideband solution. The radar settings used are summarised in Table 6.1[1]. The search grids are generated such that $G_r = 64$, $G_v = 128$, and $G_a = 256$. The step size of the search grid is chosen as 0.06 m for range estimation, 0.06 m/s for velocity estimation, and 0.12° for DOA estimation. Three targets are considered and their parameters are uniformly spaced in the search field. Firstly, $\acute{R}_{h,k}$, $v_{h,k}$, and θ_k are fixed on exact grid points from their corresponding search grids.

A single trial is performed to visualise outcomes of each stage of the proposed in Algorithm 3. For the sake of comparison, in the parameter estimation stage for each domain, the same optimisation steps are performed using steering matrices that do not take into account the artefacts of the wideband signal model. This approach is referred to as the conventional one. The chosen target parameters are shown in Table 6.2. For Doppler and DOA estimation, two snapshots are used, and two chirps are used for range estimation.

---

[1] The values of the parameters used are within the range recommended by the ITU in [152] for wideband applications

Algorithm 3 A GS-based range, Doppler, and DOA estimation algorithm in automotive applications using wideband bistatic measurements.

```
Require: $\mathbf{Z}^{\S}_{\mathbf{r},h}, \mathbf{Z}^{\S}_{\mathbf{v},h}, \mathbf{Z}^{\S}_{\mathbf{a},h}, f_0, \mu, d, T, M, L, f_s, N$.
Generate a bistatic velocity search grid of length $G_v$ whose $g_v$-th entry $v_{h,g_v}$ spans the potential values of interest
Construct a steering matrix $\mathbf{V}^{\S}_{\mathbf{g},h}[n]$ using $v_{h,g_v}$.
Perform Doppler estimation by solving (6.35) and store all $K$ bistatic velocities in the descending order of intensities as $\boldsymbol{\nu} = [\hat{v}_{h,1}, \hat{v}_{h,2}, \ldots, \hat{v}_{h,K}]$.
Generate a bistatic range search grid of length $G_r$ whose $g_r$-th entry $\acute{R}_{h,g_r}$ spans the potential values of interest.
for $k \leftarrow 1$ to $K$ do
    Construct a steering matrix $\hat{\mathbf{R}}^{\S}_{\mathbf{g},h}[m]$ using the $k$-th entry of $\boldsymbol{\nu}$ and $\acute{R}_{h,g_r}$.
    Perform range estimation by solving (6.40) using $\mathbf{Z}^{\S^{(k)}}_{\mathbf{r},h}$, which represents $\mathbf{Z}^{\S}_{\mathbf{r},h}$ for the $k$-th iteration.
    Choose the range parameter $\hat{R}_{h,k}$ with the largest intensity in the estimated spectrum.
    Construct a steering vector $\hat{\mathbf{R}}^{\S}_{h,k}[m]$ using the estimated bistatic range and velocity pair $(\hat{R}_{h,k}, \hat{v}_{h,k})$.
    Remove the contribution of the target being processed to get $\mathbf{Z}^{\S^{(k+1)}}_{\mathbf{r},h}[m] \leftarrow \left(\mathbf{Z}^{\S^{(k)}}_{\mathbf{r},h}[m] - \hat{\mathbf{R}}^{\S}_{h,k}[m](\hat{\mathbf{R}}^{\S^H}_{h,k}[m]\hat{\mathbf{R}}^{\S}_{h,k}[m])^{-1}\hat{\mathbf{R}}^{\S^H}_{h,k}[m]\mathbf{Z}^{\S^{(k)}}_{\mathbf{r},h}[m]\right)$.
end for
Store the estimated bistatic range and velocity pairs as $\boldsymbol{rv} = [(\hat{R}_{h,1}, \hat{v}_{h,1}), (\hat{R}_{h,2}, \hat{v}_{h,2}), \ldots, (\hat{R}_{h,K}, \hat{v}_{h,K})]$.
Generate a DOA search grid of length $G_a$ whose $g_a$-th entry $\theta_{g_a}$ spans the potential values of interest.
for $k \leftarrow 1$ to $K$ do
    Construct a steering matrix $\hat{\mathbf{A}}^{\S}_{\mathbf{g},h}[n]$ using the $k$-th pair in $\boldsymbol{rv}$ and $\theta_{g_a}$.
    Perform DOA estimation by solving (6.45) using $\mathbf{Z}^{\S}_{\mathbf{a},h}$.
    Store the estimated DOAs in $\boldsymbol{a} = [\hat{\theta}_1, \hat{\theta}_2, \ldots, \hat{\theta}_I]$, where $I$ is the number of detected peaks in the DOA spectrum.
    Construct the contribution of the $k$-th target using $(\hat{R}_{h,k}, \hat{v}_{h,k})$ and all $I$ DOA candidates in $\boldsymbol{a}$ as in (6.47).
    Choose the correct DOA for the $k$-th target by solving the problem in (6.48).
end for
return Estimates of $\acute{R}_{h,k}$, $v_{h,k}$, and $\theta_k$ for all $K$ targets.
```

TABLE 6.1: Radar settings used in the simulation of the wideband bistatic automotive scenario

Parameter	**Value**	**Parameter**	**Value**
P_t	10 dBm	f_s	17.66 MHz
G_t	23 dBi	T_c	29 μs
G_r	16 dBi	T	30.438 μs
σ_{bi}	0 dBsm	N	512
B	1.5 GHz	M	128
f_0	77 GHz	L	16
SNR_i	160 dB	d	1.948 mm

For Doppler estimation, the results are shown in Figure 6.1. It can be seen the proposed method accurately estimates the bistatic velocity for all targets while the conventional approach fails to do so. The effect of the coupling on performance is very clear with the energy being smeared across multiple grid points.

For range estimation, the results for every target are shown in Figure 6.2. It can also be seen that the bistatic range for all three targets is accurately estimated and the success of the Clean-like approach is visible in each spectrum. On the contrary, the conventional approach fails to accurately estimate the range parameters and the energy is smeared across multiple grid points similarly to the Doppler domain.

For DOA estimation, the results are shown for every target in Figure 6.3. The proposed method accurately estimates the DOA for all targets while the conventional method shows a slight drift from the true value. The P-test values shown next to each detected peaks represent the normalised values of the argument of the optimisation problem in (6.48). As theoretically expected, the true DOA minimises the proposed pairing function. Monte Carlo trials are also conducted to verify the success of the proposed solution by computing the RMSE as the performance metric. This time, the parameters are chosen from a uniform distribution bounded by two adjacent grid points from their corresponding search grid. The results are shown in Table 6.3, and it can be seen that the motion parameters can be accurately estimated, and unambiguously paired at the range and DOA estimation stages of the proposed algorithm.

TABLE 6.2: Chosen target parameters in the single trial for wideband estimation

Parameter	Range [m]	Velocity [m/s]	DOA [°]	Amplitude
Target 1	31.82	80.95	7.41	5.4×10^{-7}
Target 2	34.34	81.96	12.94	5.1×10^{-7}
Target 3	36.23	82.98	22.47	4.8×10^{-7}

TABLE 6.3: RMSE computed using the proposed wideband solution from 1000 trials at $SNR_i = 160$ dB

Parameter	Range [m]	Velocity [m/s]	DOA [°]
RMSE	0.0380	0.0867	0.251

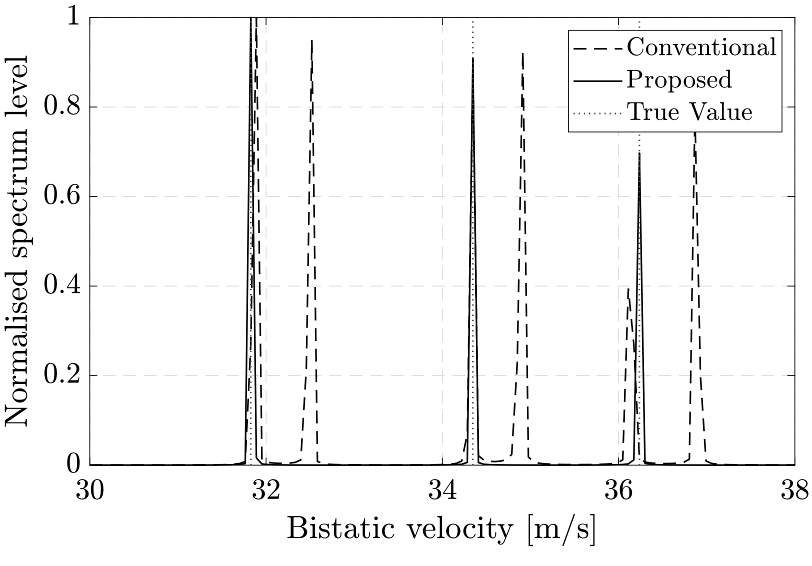

FIGURE 6.1: A comparison of the estimated velocity spectrum between the proposed method and the conventional one using wideband bistatic measurements.

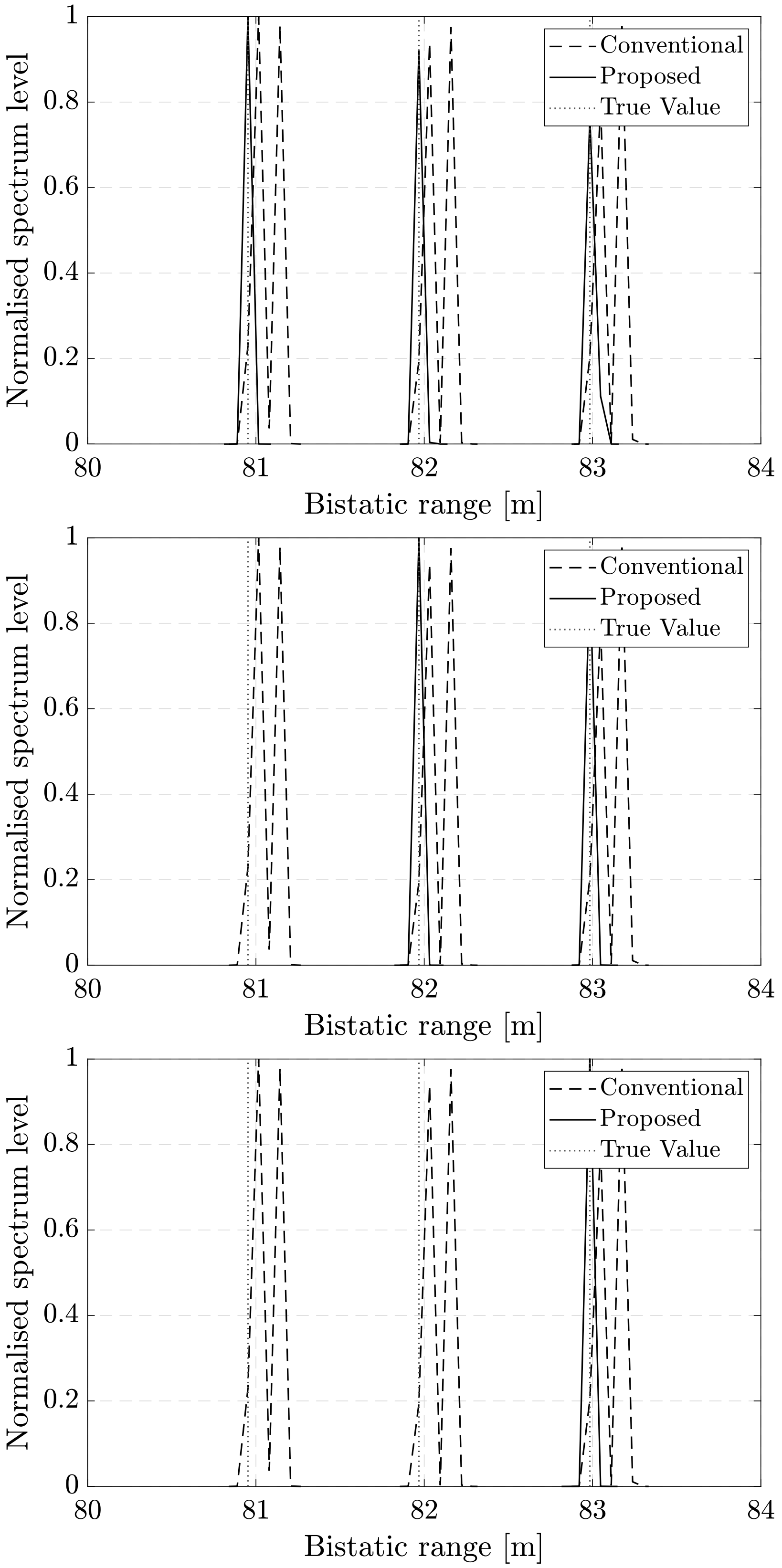

FIGURE 6.2: A comparison of the estimated range spectrum between the proposed method and the conventional one using wideband bistatic measurements. The three targets are estimated in the descending order of intensities as shown from top to bottom.

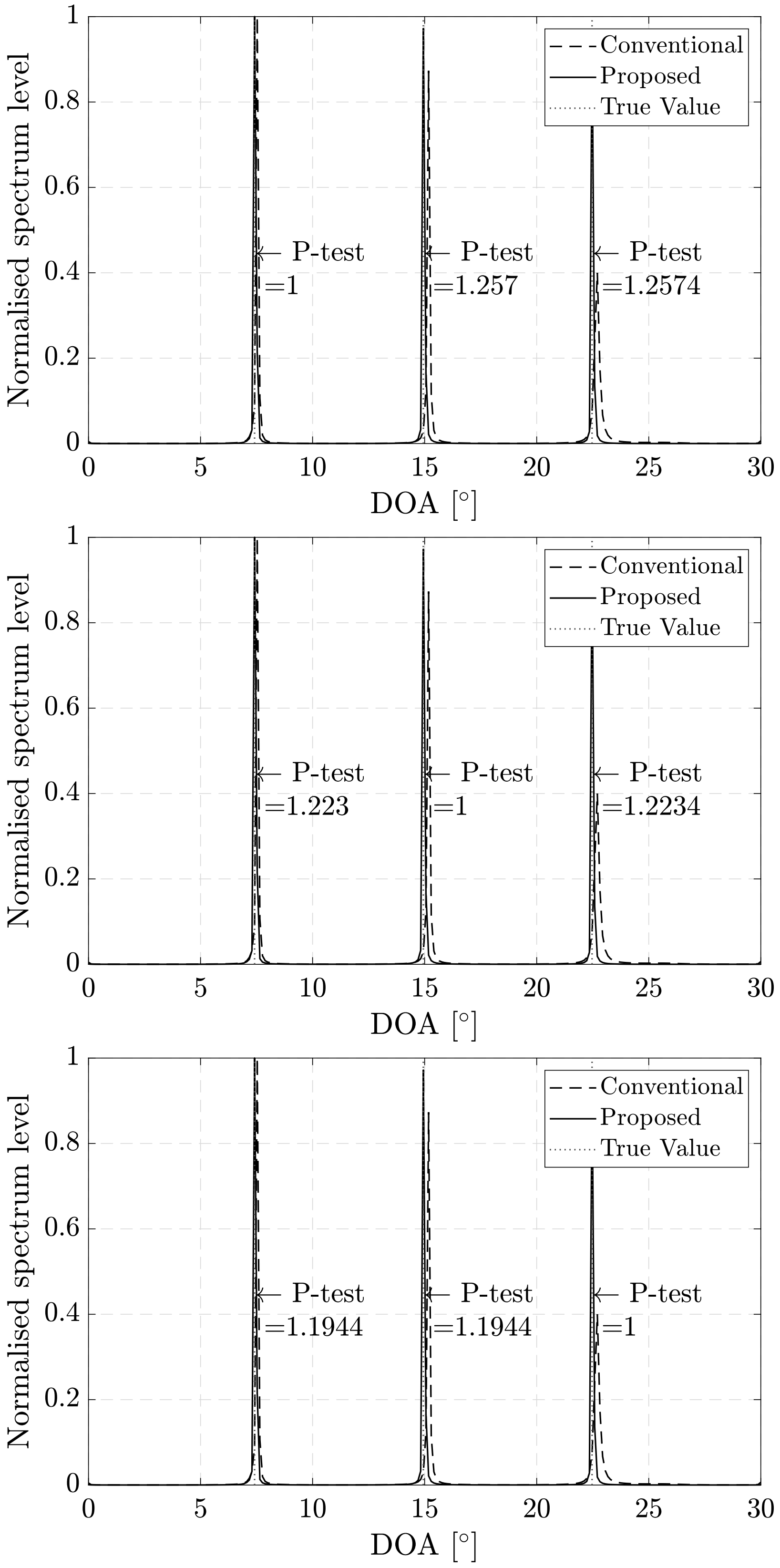

FIGURE 6.3: A comparison of the estimated DOA spectrum between the proposed method and the conventional one using wideband bistatic measurements. The spectrum corresponding to each target is shown with P-test being the value of the argument of the pairing optimisation function in (6.48).

6.5 Summary

In this chapter, the wideband case was considered for bistatic automotive radar sensing. A rigorous signal model was derived that takes into account the artefacts often neglected in the literature. A parametric analysis was presented to highlight the differences from the simplified narrowband model. Bandwidth bounds were derived to provide a criterion under which the narrowband assumptions are no longer valid and the rigorous model providing a more realistic representation of the radar signal should be used. After that, a general systematic approach was proposed to process wideband signals in decoupled measurement domains for bistatic automotive motion parameter estimation. This solution could be implemented with any parametric methods and it does not solve the wideband problem by converting it to a set of narrowband ones, it rather uses the wideband artefacts to solve the pairing problem associated with decoupled 1D estimation. Then, a GS-based algorithm was proposed for parameter estimation and unambiguous data association. Computer simulations proved the success of the proposed approach and the performance was evaluated at low noise levels as a preliminary study for this wideband problem. In future work, the proposed solution will be evaluated with higher levels of noise and increased number of targets. Its performance will be compared against the Keystone method which is often used alongside the FFT for wideband estimation.

Chapter 7

Conclusions

In this thesis, motivated by the drive towards collaborative radar and vehicle-to-infrastructure communication in the wake of the revolution in mobile communications, a novel application of bistatic radar for automotive sensing was proposed. The idea can be envisioned in a smart highway designed with infrastructure suited for radar operation where cooperative roadside sensors are carefully distributed on the side of the road and are transmitting radio-waves modulated to suit the already existing radar modules present in the road vehicles. The latter can then switch to a receiving mode and be relieved from the transmission task. Communication between the roadside sensors and the sensing vehicles can be established via pre-agreed protocols over a NR link.

In Chapter 3, the main advantage of such an application was demonstrated by showing that enhanced detection and parameter estimation performance can be achieved using the proposed bistatic configuration when compared to the monostatic counterpart. Despite the complex geometry associated with bistatic measurements, it was shown that the motion parameters of the targets, including the range, velocity, and the DOA, can be unambiguously estimated. In particular, a method based on the FFT was developed for multi-target motion parameter estimation. The synchronisation requirements for useful operation of this radar configuration were also derived. By using the radar settings recommended for vehicular applications, computer simulations were conducted using the MATLAB software to validate the theories behind this application and provide a proof of concept. A theoretical increase in detected range from bistatic measurements up to twice that from monostatic measurements was proven. Also, simulation results show that the bistatic radar can achieve the same level of performance with 3 dB less power.

In Chapter 4, a sparse representation for the signal model was derived and a method was proposed for joint localisation and Doppler estimation using convex optimisation. The sparse data was reconstructed via the LASSO technique which was implemented in MATLAB using the CVX toolbox. In order to provide a benchmark for the performance of parameter estimation, the CRB for this problem was derived. It was shown through extensive simulations that it is feasible to jointly estimate the bistatic range, velocity, and DOA under varying levels of noise, using the LASSO technique. As expected, the latter outperformed FFT with a large margin due to its ability to refine the search grid with higher granularity to achieve better estimation accuracy. FFT has a fixed grid limited by the number of measurements which highlights its main disadvantage despite its unwavering efficiency. LASSO also outperforms MUSIC albeit with a smaller margin.

In Chapter 5, the problem was extended to the multistatic case with multiple cooperative roadside sensors. It was conveyed that advanced signal processing techniques are needed to fully benefit from having multiple sources of information about the target. In fact, with the state-of-art signal processing techniques, such as Fourier-based estimation, the fusion of this information can only be done at post-processing stages. So, a method for location and Doppler estimation was proposed by adopting the GS concept for jointly processing signals from multistatic measurements offering an improved performance and increased DoFs. After avoiding an exhaustive 3D parametric search, two methods for data association were proposed and tested through computer simulations under varying settings. Computer simulations also showed that the proposed GS-based method can outperform the state-of-art, namely MUSIC which was used as the benchmark for parameter estimation performance.

In Chapter 6, a case where the roadside sensors are transmitting wideband signals was considered. A rigorous signal model was derived and the unwanted artefacts normally neglected in the narrowband case were identified and analysed. Bandwidth bounds were proposed as a criterion under which narrowband assumptions are no longer valid. It was shown that the artefacts can be resolved without forcing the problem into a narrowband one and using existing techniques. More profoundly, a general solution to the bistatic wideband problem was proposed by incorporating the artefacts as extra sources of information about the targets, and processing the data after decoupling the measurement domains. Unlike current popular approaches for parameter estimation from wideband signals, the proposed approach rids the need for filtering out or compensating for the effect of the unwanted artefacts. Then, a GS-based algorithm was proposed for decoupled range, Doppler, and DOA estimation alongside an unambiguous data association solution for multi-target scenarios. The proposed solutions were evaluated using computer simulations under high SNR levels confirming the feasibility of the approach and showing significant reduction in the effect of the unwanted wideband artefacts as a preliminary study.

7.1 Future Work

The research conducted in this thesis has undoubtedly expanded the literature in the areas encompassed by each Chapter. Moreover, it has introduced new areas of research which may be considered in future work by any interested researchers. Next, we briefly list a few of these directions:

1. The approach proposed in Chapter 6 for processing wideband signals is well suited for sparsity-based estimation. By adopting the GS concept, it can be easily seen that the steering matrices in each measurement domain lead to a common support between all the sparse vectors. So, the wideband problem can be extended to the multistatic case where Doppler estimation is performed first in line with the solution presented in Chapter 5, and then 2D localisation can be performed by combining stages two and three in the solution presented in Chapter 6. However, this approach can increase the computational cost, so means of reducing the added complexity can be explored.

2. The preliminary results of Chapter 6 are very promising. The proposed solution can be evaluated further under different operational settings and compared against popular wideband solutions such the Keystone transform.

3. The CRB has not been previously derived for the wideband bistatic automotive problem. So, by following the CRB derivation in Chapter 4, and using the wideband signal model derived in Chapter 6, the CRB can be derived for joint estimation, or for decoupled estimation by only considering the diagonal elements of the FIM.

4. It would interesting to evaluate the performance for parameter estimation when both bistatic and monostatic measurements are available.

Fortunately, similar to the multistatic case in Chapter 5, both measurements would share the same support set for location estimation and GS can be applied for improved performance.

5. For practical operation of the bistatic automotive radar, some protocols are required for handoff as the sensing vehicle switches from one roadside sensor to another along the route. A well designed scheme for smooth operation is required and interference due to signals from other roadside sensors should be minimised.

6. So far, only computer simulations were used as a means of theoretical validation for the proposed methods. It is important, however, to validate the performance with real radar data which may then attract more interest into this area of research and promote efforts for conducting real-world experiments that mimic the envisioned application.

7. The interference and clutter problems are very popular in the radar community. Particularly with automotive applications that impose higher safety requirements, it is important to ensure that a developed method is guaranteed to work in the presence of these artefacts. In future work, the effect of both problems on the probability of signal recovery from sparse measurements will be studied. Also, methods for reducing interference should and the effect of clutter should be explored.

8. The white Gaussian assumption is common within the radar community. It is, however, important to study the effect of non-white non-Gaussian noise on the performance of sparsity-based signal recovery.

Bibliography

[1] Continental Automotive | Radars — continental-automotive.com. [Online]. Available: https://www.continental-automotive.com/en/components/radars.html

[2] Front radar sensor — bosch-mobility.com. [Online]. Available: https://www.bosch-mobility.com/en/solutions/sensors/front-radar-sensor/

[3] Imaging Radar — zf.com. [Online]. Available: https://www.zf.com/products/en/cars/products_64255.html

[4] A. Merlo, "Automotive radar for the prevention of collisions," *IEEE Transactions on Industrial Electronics and Control Instrumentation*, vol. IECI-11, no. 1, pp. 1–6, 1964.

[5] W. Harokopus, "Application of radar to automobile control and sensing," in *Proceedings of the 1971 IEEE GMTT International Microwave Symposium Digest*, 1971, pp. 168–169.

[6] E. Baghdady, "Automobile radar," in *Proceedings of the 1971 IEEE GMTT International Microwave Symposium Digest*, 1971, pp. 170–171.

[7] J. Stevens and L. Nagy, "Diplex Doppler radar for automotive obstacle detection," *IEEE Transactions on Vehicular Technology*, vol. 23, no. 2, pp. 34–44, 1974.

[8] F. Holmstrom, J. Hopkins, M. Hazel, A. Newfell, and E. White, "Microwave design optimization of the tsc automobile crash sensor," in *Proceedings of the 1972 IEEE GMTT International Microwave Symposium*, 1972, pp. 142–144.

[9] D. Grimes and T. Jones, "Automotive radar: A brief review," *Proceedings of the IEEE*, vol. 62, no. 6, pp. 804–822, 1974.

[10] L. Nagy and J. Lyon, "An ultrashort pulse radar sensor for vehicular precollision obstacle detection," *IEEE Transactions on Vehicular Technology*, vol. 24, no. 4, pp. 41–45, 1975.

[11] G. Kaplan and F. Sterzer, "Dual-mode automobile collision avoidance radar," in *Proceedings of the 1975 IEEE-MTT-S International Microwave Symposium*, 1975, pp. 335–337.

[12] E. Belohoubek, J. Cusack, J. Risko, and J. Rosen, "Microcomputer controlled radar and display system for cars," *SAE Transactions*, pp. 1275–1284, 1977.

[13] E. Belohoubek, "Radar control for automotive collision mitigation and headway spacing," *IEEE Transactions on Vehicular Technology*, vol. 31, no. 2, pp. 89–99, 1982.

[14] M. Kiyoto, T. Kondoh, K. Ban, and K. Shirahata, "Radar sensor for automobiles," in *Proceedings of the 1974 IEEE International Solid-State Circuits Conference. Digest of Technical Papers*, vol. XVII, 1974, pp. 74–75.

[15] T. Tamama, A. Iwabe, K. Ban, M. Tsudo, S. Mitsui, K. Baba, M. Kiyoto, H. Endo, and N. Fujiki, "RADAR sensor for automotive collision prevention," in *Proceedings of the 1978 IEEE-MTT-S International Microwave Symposium Digest*, 1978, pp. 168–170.

[16] G. Hahlganss and L. Hahn, "Headway radar using pulse techniques," in *Proceedings of the 1976 International Conference on Automobile Electronics*, 1976, pp. 132–135.

[17] H. Zur and H. Oehlen, "Radar anticollision warning system for road vehicles," *Electrical Communication*, vol. 52, no. 2, 1977.

[18] G. Neininger, "FM/CW radar with high resolution in range and Doppler; Application for anti-collision radar for vehicles," in *Proceedings of the 1977 IEE International Radar Conference*, 1977, pp. 526–534.

[19] E. H. Düll and H. J. Peters, "Collision avoidance system for automobiles," *SAE Transactions*, pp. 1250–1260, 1978.

[20] I. Gresham, N. Jain, T. Budka, A. Alexanian, N. Kinayman, B. Ziegner, S. Brown, and P. Staecker, "A compact manufacturable 76-77-GHz radar module for commercial ACC applications," *IEEE Transactions on Microwave Theory and Techniques*, vol. 49, no. 1, pp. 44–58, 2001.

[21] J. Wenger, "Automotive radar–Status and perspectives," in *Proceedings of the IEEE Compound Semiconductor Integrated Circuit Symposium, 2005. CSIC '05.*, 2005, p. 4.

[22] J. Hasch, E. Topak, R. Schnabel, T. Zwick, R. Weigel, and C. Waldschmidt, "Millimeter-wave technology for automotive radar sensors in the 77 GHz frequency band," *IEEE Transactions on Microwave Theory and Techniques*, vol. 60, no. 3, pp. 845–860, 03 2012.

[23] "Radar for automotive : automated driving applications strengthens market dynamics — yolegroup.com."

[24] O. Edvardsson, "An fmcw radar for accurate level measurements," in *Proceedings of the 1979 9th European Microwave Conference*, 1979, pp. 712–715.

[25] A. Phadke and J. S. Thorp, "History and applications of phasor measurements," in *Proceedings of 2006 the IEEE PES Power Systems Conference and Exposition*, 2006, pp. 331–335.

[26] E. Barlow, "Doppler radar," *Proceedings of the IRE*, vol. 37, no. 4, pp. 340–355, 1949.

[27] F. B. Berger, "The Nature of Doppler Velocity Measurement," *IRE Transactions on Aeronautical and Navigational Electronics*, vol. ANE-4, no. 3, pp. 103–112, 1957.

[28] H. Friis, C. Feldman, and W. Sharpless, "The determination of the direction of arrival of short radio waves," *Proceedings of the Institute of Radio Engineers*, vol. 22, no. 1, pp. 47–78, 1934.

[29] M. I. Skolnik, *Radar handbook*. McGraw-Hill Education, 2008.

[30] S. Park and N. Ahmed, "Optimum array filters for two-dimensional sensor arrays," *IEEE Transactions on Geoscience and Remote Sensing*, vol. GE-25, no. 6, pp. 879–884, 1987.

[31] Q.-Y. Yin, R. Newcomb, and L.-H. Zou, "Estimating two-dimensional directions of arrival of narrow band sources," in *Proceedings of the IEEE TENCON'90: 1990 IEEE Region 10 Conference on Computer and Communication Systems. Conference Proceedings*, 1990, pp. 389–393 vol.1.

[32] S. Rao. Introduction to mmwave sensing: FMCW radars. [Online]. Available: https://www.ti.com/sensors/mmwave-radar/overview.html

[33] S. M. Patole, M. Torlak, D. Wang, and M. Ali, "Automotive radars: A review of signal processing techniques," *IEEE Signal Processing Magazine*, vol. 34, no. 2, pp. 22–35, 2017.

[34] M. A. Richards, J. Scheer, W. A. Holm, and W. L. Melvin, "Principles of modern radar," 2010.

[35] B. J. Donnet and I. D. Longstaff, "Combining mimo radar with ofdm communications," in *Proceedings of the 2006 European Radar Conference*, 2006, pp. 37–40.

[36] C. Sturm, E. Pancera, T. Zwick, and W. Wiesbeck, "A novel approach to ofdm radar processing," in *Proceedings of the 2009 IEEE Radar Conference*, 2009, pp. 1–4.

[37] Y. D. Shirman, S. P. Leshchenko, and V. M. Orlenko, "Wideband radar (advantages and problems)," in *Proceedings of the 2004 Second International Workshop Ultrawideband and Ultrashort Impulse Signals*, 2004, pp. 71–76.

[38] F. Sabath, E. L. Mokole, and S. N. Samaddar, "Definition and classification of ultra-wideband signals and devices," *URSI Radio Science Bulletin*, vol. 2005, no. 313, pp. 12–26, 2005.

[39] M. Born, E. Wolf, A. B. Bhatia, P. C. Clemmow, D. Gabor, A. R. Stokes, A. M. Taylor, P. A. Wayman, and W. L. Wilcock, *Principles of Optics: Electromagnetic Theory of Propagation, Interference and Diffraction of Light*, 7th ed. Cambridge University Press, 1999.

[40] H. Krim and M. Viberg, "Two decades of array signal processing research: the parametric approach," *IEEE Signal Processing Magazine*, vol. 13, no. 4, pp. 67–94, 07 1996.

[41] H. L. Van Trees, *Detection, estimation, and modulation theory*. Wiley, 2001.

[42] H. J. Nussbaumer and H. J. Nussbaumer, *The fast Fourier transform*. Springer, 1981.

[43] P. Stoica, R. L. Moses *et al.*, *Spectral analysis of signals*. Pearson Prentice Hall Upper Saddle River, NJ, 2005, vol. 452.

[44] I. Bilik, O. Longman, S. Villeval, and J. Tabrikian, "The rise of radar for autonomous vehicles: Signal processing solutions and future research directions," *IEEE Signal Processing Magazine*, vol. 36, no. 5, pp. 20–31, 2019.

[45] E. Jacobsen and P. Kootsookos, "Fast, accurate frequency estimators [dsp tips & tricks]," *IEEE Signal Processing Magazine*, vol. 24, no. 3, pp. 123–125, 2007.

[46] F. Engels, P. Heidenreich, A. M. Zoubir, F. K. Jondral, and M. Wintermantel, "Advances in automotive radar: A framework on computationally efficient high-resolution frequency estimation," *IEEE Signal Processing Magazine*, vol. 34, no. 2, pp. 36–46, 2017.

[47] R. Schmidt, "Multiple emitter location and signal parameter estimation," *IEEE Transactions on Antennas and Propagation*, vol. 34, pp. 276–280, 03 1986.

[48] R. Roy and T. Kailath, "ESPRIT-estimation of signal parameters via rotational invariance techniques," *IEEE Transactions on Acoustics, Speech, and Signal Processing*, vol. 37, no. 7, pp. 984–995, 07 1989.

[49] J. Odendaal, E. Barnard, and C. Pistorius, "Two-dimensional superresolution radar imaging using the MUSIC algorithm," *IEEE Transactions on Antennas and Propagation*, vol. 42, no. 10, pp. 1386–1391, 1994.

[50] S. Xu, B. J. Kooij, and A. Yarovoy, "Joint Doppler and DOA estimation using (Ultra-)Wideband FMCW signals," *Signal Processing*, vol. 168, p. 107259, 2020.

[51] F. Belfiori, W. van Rossum, and P. Hoogeboom, "Application of 2D MUSIC algorithm to range-azimuth FMCW radar data," in *Proceedings of the 2012 9th European Radar Conference*, 2012, pp. 242–245.

[52] S. Hamidi, M. Nezhad-Ahmadi, and S. Safavi-Naeini, "SAR Imaging for a 79GHz FMCW Radar Based on MUSIC Method," in *Proceedings of the 2018 18th International Symposium on Antenna Technology and Applied Electromagnetics (ANTEM)*, 2018, pp. 1–2.

[53] S. Xu and A. Yarovoy, "Joint Parameters Estimation Using 3D Tensor MUSIC in the Presence of Phase Residual," in *Proceedings of the 2018 International Conference on Radar (RADAR)*, 2018, pp. 1–4.

[54] E. J. Candes and M. B. Wakin, "An introduction to compressive sampling," *IEEE Signal Processing Magazine*, vol. 25, no. 2, pp. 21–30, 2008.

[55] D. Donoho, "Compressed sensing," *IEEE Transactions on Information Theory*, vol. 52, no. 4, pp. 1289–1306, 2006.

[56] C. E. Shannon, "Communication in the presence of noise," *Proceedings of the IRE*, vol. 37, no. 1, pp. 10–21, 1949.

[57] S. Qaisar, R. M. Bilal, W. Iqbal, M. Naureen, and S. Lee, "Compressive sensing: From theory to applications, a survey," *Journal of Communications and networks*, vol. 15, no. 5, pp. 443–456, 2013.

[58] D. Malioutov, M. Cetin, and A. S. Willsky, "A sparse signal reconstruction perspective for source localization with sensor arrays," *IEEE transactions on signal processing*, vol. 53, no. 8, pp. 3010–3022, 2005.

[59] Q. Shen, W. Liu, W. Cui, and S. Wu, "Underdetermined DOA estimation under the compressive sensing framework: A review," *IEEE Access*, vol. 4, pp. 8865–8878, 2016.

[60] R. Baraniuk and P. Steeghs, "Compressive radar imaging," in *Proceedings of the 2007 IEEE Radar Conference*, 2007, pp. 128–133.

[61] M. A. Herman and T. Strohmer, "High-resolution radar via compressed sensing," *IEEE Transactions on Signal Processing*, vol. 57, no. 6, pp. 2275–2284, 2009.

[62] J. H. Ender, "On compressive sensing applied to radar," *Signal Processing*, vol. 90, no. 5, pp. 1402 – 1414, 2010, Special Section on Statistical Signal and Array Processing.

[63] L. Zhao, L. Wang, L. Yang, A. M. Zoubir, and G. Bi, "The race to improve radar imagery: An overview of recent progress in statistical sparsity-based techniques," *IEEE Signal Processing Magazine*, vol. 33, no. 6, pp. 85–102, 2016.

[64] S. Lutz, D. Ellenrieder, T. Walter, and R. Weigel, "On fast chirp modulations and compressed sensing for automotive radar applications," in *Proceedings of the 2014 15th International Radar Symposium (IRS)*, 2014, pp. 1–6.

[65] J. Bechter, F. Roos, M. Rahman, and C. Waldschmidt, "Automotive radar interference mitigation using a sparse sampling approach," in *Proceedings of the 2017 European Radar Conference (EURAD)*, 2017, pp. 90–93.

[66] A. Correas-Serrano and M. A. González-Huici, "Experimental evaluation of compressive sensing for DOA estimation in automotive radar," in *Proceedings of the 2018 19th International Radar Symposium (IRS)*, 2018, pp. 1–10.

[67] F. Roos, P. Hügler, L. L. T. Torres, C. Knill, J. Schlichenmaier, C. Vasanelli, N. Appenrodt, J. Dickmann, and C. Waldschmidt, "Compressed sensing based single snapshot DOA estimation for sparse mimo radar arrays," in *Proceedings of the 2019 12th German Microwave Conference (GeMiC)*, 2019, pp. 75–78.

[68] S. Gishkori, L. Daniel, M. Gashinova, and B. Mulgrew, "Imaging for a forward scanning automotive synthetic aperture radar," *IEEE Transactions on Aerospace and Electronic Systems*, vol. 55, no. 3, pp. 1420–1434, 2019.

[69] S. Sun and Y. D. Zhang, "4d automotive radar sensing for autonomous vehicles: A sparsity-oriented approach," *IEEE Journal of Selected Topics in Signal Processing*, vol. 15, no. 4, pp. 879–891, 2021.

[70] R. Tibshirani, "Regression shrinkage and selection via the lasso," *Journal of the Royal Statistical Society Series B: Statistical Methodology*, vol. 58, no. 1, pp. 267–288, 1996.

[71] M. Yuan and Y. Lin, "Model selection and estimation in regression with grouped variables," *Journal of the Royal Statistical Society Series B: Statistical Methodology*, vol. 68, no. 1, pp. 49–67, 2006.

[72] E. V. Appleton and M. Barnett, "On some direct evidence for downward atmospheric reflection of electric rays," *Proceedings of the Royal Society of London. Series A, Containing Papers of a Mathematical and Physical Character*, vol. 109, no. 752, pp. 621–641, 1925.

[73] R. A. Watson-Watt, *Three Steps to Victory: A Personal Account by Radar's Greatest Pioneer*. London: Odhams Press, 1957.

[74] R. V. Jones, *Most secret war*. Penguin UK, 2009.

[75] H. Griffiths and N. Willis, "Klein Heidelberg—The first modern bistatic radar system," *IEEE Transactions on Aerospace and Electronic Systems*, vol. 46, no. 4, pp. 1571–1588, 2010.

[76] M. I. Skolnik, "An analysis of bistatic radar," *IRE Transactions on Aerospace and Navigational Electronics*, vol. 8, no. 1, pp. 19–27, 1961.

[77] K. Siegel, "Bistatic radars and forward scattering," in *Proceedings of the National Conference on Aeronautical Electronics*, 1958, pp. 286–290.

[78] A. Ivanov, "Improved radar designs outwit complex threats," *Microwaves*, vol. 15, p. 54, 1976.

[79] J. Glaser, "Fifty years of bistatic and multistatic radar," in *IEE Proceedings F (Communications, Radar and Signal Processing)*, vol. 133, no. 7. IET, 1986, pp. 596–603.

[80] S. Pinnell, "Stealth aircraft," *Letters to the Editor, Aviation Week and Space Technology*, vol. 114, no. 18, p. 82, 1981.

[81] J. I. Glaser, "Bistatic radars hold promise for future systems," *MSN*, vol. 14, no. 11, pp. 119–136, 1984.

[82] A. Moccia, N. Chiacchio, and A. Capone, "Spaceborne bistatic synthetic aperture radar for remote sensing applications," *International Journal of Remote Sensing*, vol. 21, no. 18, pp. 3395–3414, 2000.

[83] I. Walterscheid, J. Ender, A. Brenner, and O. Loffeld, "Bistatic sar processing and experiments," *IEEE Transactions on Geoscience and Remote Sensing*, vol. 44, no. 10, pp. 2710–2717, 2006.

[84] A. Arnold-Bos, A. Khenchaf, and A. Martin, "Bistatic Radar Imaging of the Marine Environment—Part I: Theoretical Background," *IEEE Transactions on Geoscience and Remote Sensing*, vol. 45, no. 11, pp. 3372–3383, 2007.

[85] A. Arnold-Bos, A. Khenchaf, and A. Martin, "Bistatic Radar Imaging of the Marine Environment—Part II: Theoretical Background," *IEEE Transactions on Geoscience and Remote Sensing*, vol. 45, no. 11, pp. 3384–3396, 2007.

[86] J. Thomas, C. Baker, and H. Griffiths, "Hf passive bistatic radar potential and applications for remote sensing," in *Proceedings of the 2008 Conference on New Trends for Environmental Monitoring Using Passive Systems*. IEEE, 2008, pp. 1–5.

[87] R. Wang, Y. Deng, Z. Zhang, Y. Shao, J. Hou, G. Liu, and X. Wu, "Double-Channel Bistatic SAR System With Spaceborne Illuminator for 2-D and 3-D SAR Remote Sensing," *IEEE Transactions on Geoscience and Remote Sensing*, vol. 51, no. 8, pp. 4496–4507, 2013.

[88] V. U. Zavorotny, S. Gleason, E. Cardellach, and A. Camps, "Tutorial on Remote Sensing Using GNSS Bistatic Radar of Opportunity," *IEEE Geoscience and Remote Sensing Magazine*, vol. 2, no. 4, pp. 8–45, 2014.

[89] A. G. Voronovich and V. U. Zavorotny, "Bistatic radar equation for signals of opportunity revisited," *IEEE Transactions on Geoscience and Remote Sensing*, vol. 56, no. 4, pp. 1959–1968, 2018.

[90] P. Howland, "Target tracking using television-based bistatic radar," *IEE Proceedings-Radar, Sonar and Navigation*, vol. 146, no. 3, pp. 166–174, 1999.

[91] J. Brown, K. Woodbridge, A. Stove, and S. Watts, "Air target detection using airborne passive bistatic radar," *Electronics letters*, vol. 46, no. 20, pp. 1396–1397, 2010.

[92] J. Brown, K. Woodbridge, H. Griffiths, A. Stove, and S. Watts, "Passive bistatic radar experiments from an airborne platform," *IEEE Aerospace and Electronic Systems Magazine*, vol. 27, no. 11, pp. 50–55, 2012.

[93] H. C. Zeng, P. B. Wang, J. Chen, W. Liu, L. L. Ge, and W. Yang, "A novel general imaging formation algorithm for GNSS-based bistatic sar," *Sensors*, vol. 16, no. 3, p. 294, 2016.

[94] H. C. Zeng, J. Chen, P. B. Wang, W. Yang, and W. Liu, "2-D coherent integration processing and detecting of aircrafts using GNSS-based passive radar," *Remote Sensing*, vol. 10, no. 7, 2018.

[95] P. Ufimtsev, "Comments on diffraction principles and limitations of rcs reduction techniques," *Proceedings of the IEEE*, vol. 84, no. 12, pp. 1830–1851, 1996.

[96] L. Gürel, H. Bağcı, J.-C. Castelli, A. Cheraly, and F. Tardivel, "Validation through comparison: Measurement and calculation of the bistatic radar cross section of a stealth target," *Radio science*, vol. 38, no. 3, 2003.

[97] N. J. Willis and H. D. Griffiths, *Advances in bistatic radar*. SciTech Publishing, 2007, vol. 2.

[98] H. Griffiths, "New directions in bistatic radar," in *Proceedings of the 2008 IEEE Radar Conference*. IEEE, 2008, pp. 1–6.

[99] I. Suberviola, I. Mayordomo, and J. Mendizabal, "Experimental results of air target detection with a gps forward-scattering radar," *IEEE Geoscience and Remote Sensing Letters*, vol. 9, no. 1, pp. 47–51, 2012.

[100] B. Paul, A. R. Chiriyath, and D. W. Bliss, "Survey of rf communications and sensing convergence research," *IEEE Access*, vol. 5, pp. 252–270, 2017.

[101] N. Cao, Y. Chen, X. Gu, and W. Feng, "Joint bi-static radar and communications designs for intelligent transportation," *IEEE Transactions on Vehicular Technology*, vol. 69, no. 11, pp. 13 060–13 071, 2020.

[102] H. Wymeersch, G. Seco-Granados, G. Destino, D. Dardari, and F. Tufvesson, "5G mmWave Positioning for Vehicular Networks," *IEEE Wireless Communications*, vol. 24, no. 6, pp. 80–86, 2017.

[103] H. Wymeersch, D. Shrestha, C. M. de Lima, V. Yajnanarayana, B. Richerzhagen, M. F. Keskin, K. Schindhelm, A. Ramirez, A. Wolfgang, M. F. de Guzman, K. Haneda, T. Svensson, R. Baldemair, and S. Parkvall, "Integration of Communication and Sensing in 6G: a Joint Industrial and Academic Perspective," in *Proceedings of the 2021 IEEE*

32nd Annual International Symposium on Personal, Indoor and Mobile Radio Communications (PIMRC), 2021, pp. 1–7.

[104] A. A. Salah, R. Raja Abdullah, A. Ismail, F. Hashim, and N. H. Abdul Aziz, "Experimental study of LTE signals as illuminators of opportunity for passive bistatic radar applications," *Electronics Letters*, vol. 50, no. 7, pp. 545–547, 2014.

[105] S. H. Dokhanchi, M. B. Shankar, T. Stifter, and B. Ottersten, "OFDM-based automotive joint radar-communication system," in *Proceedings of the 2018 IEEE Radar Conference (RadarConf18)*. IEEE, 2018, pp. 0902–0907.

[106] S. H. Dokhanchi, B. S. Mysore, K. V. Mishra, and B. Ottersten, "A mmWave automotive joint radar-communications system," *IEEE Transactions on Aerospace and Electronic Systems*, vol. 55, no. 3, pp. 1241–1260, 2019.

[107] S. H. Dokhanchi, M. B. Shankar, K. V. Mishra, T. Stifter, and B. Ottersten, "Performance analysis of mmwave bi-static PMCW-based automotive joint radar-communications system," in *Proceedings of the 2019 IEEE Radar Conference (RadarConf)*. IEEE, 2019, pp. 1–6.

[108] R. S. Thoma, C. Andrich, G. Del Galdo, M. Dobereiner, M. A. Hein, M. Kaske, G. Schafer, S. Schieler, C. Schneider, A. Schwind *et al.*, "Cooperative passive coherent location: A promising 5g service to support road safety," *IEEE Communications Magazine*, vol. 57, no. 9, pp. 86–92, 2019.

[109] S. Schieler, C. Schneider, C. Andrich, M. Döbereiner, J. Luo, A. Schwind, R. S. Thomä, and G. Del Galdo, "OFDM waveform for distributed radar sensing in automotive scenarios," *International Journal of Microwave and Wireless Technologies*, vol. 12, no. 8, pp. 716–722, 2020.

[110] M. Gottinger, M. Hoffmann, M. Christmann, M. Schütz, F. Kirsch, P. Gulden, and M. Vossiek, "Coherent Automotive Radar Networks: The Next Generation of Radar-Based Imaging and Mapping," *IEEE Journal of Microwaves*, vol. 1, no. 1, pp. 149–163, 2021.

[111] X. Zhang, F. Wang, and H. Li, "An efficient method for cooperative multi-target localization in automotive radar," *IEEE Signal Processing Letters*, vol. 29, pp. 16–20, 2021.

[112] G. P. Blasone, F. Colone, and P. Lombardo, "Passive radar concept for automotive applications," in *Proceedings of the 2022 IEEE Radar Conference (RadarConf22)*. IEEE, 2022, pp. 1–5.

[113] J. J. Crispin, *Methods of radar cross-section analysis*. New York: Elsevier, 1968.

[114] P. Blacksmith and R. Mack, “On measuring the radar cross sections of ducks and chickens,” *Proceedings of the IEEE*, vol. 53, no. 8, pp. 1125–1125, 1965.

[115] T. Greenwood, “Reconnaissance, surveillance and arms control: Introduction,” *Adelphi Papers*, vol. 12, no. 88, pp. 1–4, 1972.

[116] J. Baniak, G. Baker, A. M. Cunningham, and L. Martin, “Silent sentry passive surveillance,” *Aviation week and space technology*, vol. 7, pp. 134–139, 1999.

[117] A. G. Westra, “Radar versus stealth: Passive radar and the future of us military power,” *Joint Force Quarterly: JFQ*, no. 55, p. 136, 2009.

[118] K. E. Olsen and W. Asen, “Bridging the gap between civilian and military passive radar,” *IEEE Aerospace and Electronic Systems Magazine*, vol. 32, no. 2, pp. 4–12, 2017.

[119] S. Sun, A. P. Petropulu, and H. V. Poor, “MIMO radar for advanced driver-assistance systems and autonomous driving: Advantages and challenges,” *IEEE Signal Processing Magazine*, vol. 37, no. 4, pp. 98–117, 07 2020.

[120] I. Immoreev and P. Fedotov, “Ultra wideband radar systems: advantages and disadvantages,” in *Proceedings of the 2002 IEEE Conference on Ultra Wideband Systems and Technologies*, 2002, pp. 201–205.

[121] J. Steinbaeck, C. Steger, G. Holweg, and N. Druml, “Next generation radar sensors in automotive sensor fusion systems,” in *Proceedings of the 2017 Sensor Data Fusion: Trends, Solutions, Applications (SDF)*. IEEE, 2017, pp. 1–6.

[124] Z. Geng, “Evolution of netted radar systems,” *IEEE Access*, vol. 8, pp. 124 961–124 977, 2020.

[125] H. Griffiths, “Bistatic and multistatic radar,” in *Proceedings of the IEE Military Radar Seminar*, 2004.

[126] K. Kulpa, “Continuous wave radars–monostatic, multistatic and network,” in *Advances in Sensing with security applications*. Springer, 2006, pp. 215–242.

[127] B. Wang, J. Chen, W. Liu, and L. T. Yang, “Minimum cost placement of bistatic radar sensors for belt barrier coverage,” *IEEE Transactions on Computers*, vol. 65, no. 2, pp. 577–588, 2015.

[128] M. Weib, “Synchronisation of bistatic radar systems,” in *Proceedings of the 2004 IEEE International Geoscience and Remote Sensing Symposium*, 2004, pp. 1750–1753.

[129] M. Malanowski, *Signal processing for passive bistatic radar*. Artech House, 2019.

[130] G. Soysal and M. Efe, "Data fusion in a multistatic radar network using covariance intersection and particle filtering," in *Proceedings of the 14th International Conference on Information Fusion*. IEEE, 2011, pp. 1–7.

[131] C. Xiaomao, Y. Jianxin, G. Ziping, R. Yunhua, and W. Xianrong, "Data fusion of target characteristic in multistatic passive radar," *Journal of Systems Engineering and Electronics*, vol. 32, no. 4, pp. 811–821, 2021.

[132] W. Lewandowski and C. Thomas, "Gps time transfer," *Proceedings of the IEEE*, vol. 79, no. 7, pp. 991–1000, 1991.

[133] D. Kirchner, "Two-way time transfer via communication satellites," *Proceedings of the IEEE*, vol. 79, no. 7, pp. 983–990, 1991.

[134] D. W. Allan, N. Ashby, and C. C. Hodge, *The science of timekeeping*. Hewlett-Packard, 1997.

[135] W. Q. Wang, C. Ding, and X. Liang, "Time and phase synchronisation via direct-path signal for bistatic synthetic aperture radar systems," *IET Radar, Sonar & Navigation*, vol. 2, no. 1, pp. 1–11, 2008.

[136] M. Ash, M. Ritchie, K. Chetty, and P. V. Brennan, "A new multistatic fmcw radar architecture by over-the-air deramping," *IEEE Sensors Journal*, vol. 15, no. 12, pp. 7045–7053, 2015.

[137] J. Liuv and X. Chen, "Time synchronisation for multi-static radar via microwave and troposcatter," *The Journal of Engineering*, vol. 2018, no. 1, pp. 39–41, 2018.

[138] W. Liu, H. Yuan, and J. Ge, "Local-area nanosecond-accuracy time synchronisation based on gps l1 observations," *IET Radar, Sonar & Navigation*, vol. 13, no. 5, pp. 824–829, 2019.

[139] O. Bar-Shalom, N. Dvorecki, L. Banin, and Y. Amizur, "Accurate Time Synchronization for Automotive Cooperative Radar (CoRD) Applications," in *Proceedings of the 2020 IEEE International Radar Conference (RADAR)*, 2020, pp. 500–505.

[140] S. Lewis and M. Inggs, "Synchronization of Coherent Netted Radar Using White Rabbit Compared With One-Way Multichannel GPSDOs," *IEEE Transactions on Aerospace and Electronic Systems*, vol. 57, no. 3, pp. 1413–1422, 2021.

[141] P. J. Beasley and M. A. Ritchie, "Multistatic radar synchronisation using COTS GPS disciplined oscillators," in *Proceedings of the International Conference on Radar Systems*, 2022, pp. 429–434.

[142] S. Kuutti, S. Fallah, K. Katsaros, M. Dianati, F. Mccullough, and A. Mouzakitis, "A survey of the state-of-the-art localization techniques and their potentials for autonomous vehicle applications," *IEEE Internet of Things Journal*, vol. 5, no. 2, pp. 829–846, 04 2018.

[143] F. Engels, P. Heidenreich, M. Wintermantel, L. Stäcker, M. Al Kadi, and A. M. Zoubir, "Automotive radar signal processing: Research directions and practical challenges," *IEEE Journal of Selected Topics in Signal Processing*, vol. 15, no. 4, pp. 865–878, 03 2021.

[144] A. Eskandarian, *Handbook of Intelligent Vehicles*. Springer Nature, 2012.

[145] J. Dickmann, J. Klappstein, M. Hahn, N. Appenrodt, H. L. Bloecher, K. Werber, and A. Sailer, "Automotive radar the key technology for autonomous driving: From detection and ranging to environmental understanding," in *Proceedings of the IEEE Radar Conference*, 05 2016, pp. 1–6.

[122] M. Cherniakov, *Bistatic Radar: Emerging Technology.* New York, USA: Wiley, 2008, pp. 247–313.

[146] H. D. Griffiths and C. J. Baker, *An introduction to passive radar*. Artech House, 2017.

[147] O. Kanhere, S. Goyal, M. Beluri, and T. S. Rappaport, "Target localization using bistatic and multistatic radar with 5G NR waveform," in *Proceedings of the 2021 IEEE 93rd Vehicular Technology Conference*. IEEE, 2021, pp. 1–7.

[148] J. C. Lin, "Synchronization requirements for 5G: An overview of standards and specifications for cellular networks," *IEEE Vehicular Technology Magazine*, vol. 13, no. 3, pp. 91–99, 2018.

[149] N. J. Willis, *Bistatic Radar*. SciTech Publishing, 2005, vol. 2.

[150] H. L. Van Trees, *Optimum Array Processing, Part IV of Detection, Estimation, and Modulation Theory*. New York: Wiley, 2002.

[151] J. W. Crispin, *A Theoretical Method for the Calculation of the Radar Cross Sections of Aircraft and Missles*. University of Michigan, College of Engineering, 1959, vol. 59, no. 774.

[152] M. Series, "Systems characteristics of automotive radars operating in the frequency band 76–81 GHz for intelligent transport systems applications," *Recommendation ITU-R, M*, pp. 2057–1, 2014.

[153] H. Rohling, "Radar CFAR Thresholding in Clutter and Multiple Target Situations," *IEEE Transactions on Aerospace and Electronic Systems*, vol. AES-19, no. 4, pp. 608–621, 1983.

[154] E. J. Candès *et al.*, "Compressive sampling," in *Proceedings of the International Congress of Mathematicians*, vol. 3. Citeseer, 2006, pp. 1433–1452.

[155] T. Strohmer and B. Friedlander, "Analysis of sparse mimo radar," *Applied and Computational Harmonic Analysis*, vol. 37, no. 3, pp. 361–388, 2014.

[156] P. Stoica and A. Nehorai, "MUSIC, maximum likelihood, and Cramer-Rao bound," *IEEE Transactions on Acoustics, speech, and signal processing*, vol. 37, no. 5, pp. 720–741, 1989.

[157] F. Colone, D. O'hagan, P. Lombardo, and C. Baker, "A multistage processing algorithm for disturbance removal and target detection in passive bistatic radar," *IEEE Transactions on Aerospace and Electronic Systems*, vol. 45, no. 2, pp. 698–722, 2009.

[158] J. E. Palmer and S. J. Searle, "Evaluation of adaptive filter algorithms for clutter cancellation in passive bistatic radar," in *Proceedings of the 2012 IEEE Radar Conference*, 2012, pp. 493–498.

[159] J. L. Garry, G. E. Smith, and C. J. Baker, "Direct signal suppression schemes for passive radar," in *Proceedings of the 2015 Signal Processing Symposium*, 2015, pp. 1–5.

[160] E. Fishler, A. Haimovich, R. Blum, D. Chizhik, L. Cimini, and R. Valenzuela, "MIMO radar: An idea whose time has come," in *Proceedings of the 2004 IEEE Radar Conference*, 04 2004, pp. 71–78.

[161] M. E. Davis, *Advances in Bistatic Radar*. SciTech Publishing, 2007, vol. 2.

[162] H. C. Zeng, P. B. Wang, J. Chen, W. Liu, L. L. Ge, and W. Yang, "A novel general imaging formation algorithm for GNSS-based bistatic sar," *Sensors*, vol. 16, no. 3, p. 294, 2016.

[163] H. Griffiths and C. Baker, "Passive coherent location radar systems. part 1: Performance prediction," *IEE Proceedings-Radar, Sonar and Navigation*, vol. 152, no. 3, pp. 153–159, 2005.

[164] Y. D. Zhang, M. G. Amin, and B. Himed, "Structure-aware sparse reconstruction and applications to passive multistatic radar," *IEEE Aerospace and Electronic Systems Magazine*, vol. 32, no. 2, pp. 68–78, 02 2017.

[165] F. Liu, C. Masouros, A. P. Petropulu, H. Griffiths, and L. Hanzo, "Joint radar and communication design: Applications, state-of-the-art, and the road ahead," *IEEE Transactions on Communications*, vol. 68, no. 6, pp. 3834–3862, 2020.

[166] S. H. Dokhanchi, B. S. Mysore, K. V. Mishra, and B. Ottersten, "A mmWave automotive joint radar-communications system," *IEEE Transactions on Aerospace and Electronic Systems*, vol. 55, no. 3, pp. 1241–1260, 2019.

[167] A. Moussa and W. Liu, "Enhanced detection in automotive applications using bistatic radar with cooperative roadside sensors," in *Proceedings of the 2021 CIE International Conference on Radar (Radar)*, 2021, pp. 1649–1653.

[168] A. Moussa and W. Liu, "A Two-Stage Sparsity-Based Method for Location and Doppler Estimation in Bistatic Automotive Radar," in *Proceedings of the 2023 IEEE Statistical Signal Processing Workshop (SSP)*, 2023, pp. 487–491.

[169] V. Chernyak, "Fundamentals of multisite radar systems," in *Multistatic radars and Multiradar Systems*. Gordon and Breach Science Publishers, 1998.

[170] S. Qin, Y. D. Zhang, and M. G. Amin, "Generalized coprime array configurations for direction-of-arrival estimation," *IEEE Transactions on Signal Processing*, vol. 63, no. 6, pp. 1377–1390, 03 2015.

[171] Q. Shen, W. Liu, W. Cui, S. Wu, Y. D. Zhang, and M. G. Amin, "Low-complexity direction-of-arrival estimation based on wideband co-prime arrays," *IEEE/ACM Transactions on Audio, Speech, and Language Processing*, vol. 23, no. 9, pp. 1445–1456, 09 2015.

[172] Q. Shen, W. Liu, W. Cui, and S. L. Wu, "Underdetermined DOA Estimation Under the Compressive Sensing Framework: A Review," *IEEE Access*, vol. 4, pp. 8865–8878, 2016.

[173] N. Simon, J. Friedman, T. Hastie, and R. Tibshirani, "A sparse-group lasso," *Journal of Computational and Graphical Statistics*, vol. 22, no. 2, pp. 231–245, 2013.

[174] S. Ji, D. Dunson, and L. Carin, "Multitask compressive sensing," *IEEE Transactions on Signal Processing*, vol. 57, no. 1, pp. 92–106, 2009.

[175] Z. Zhang and B. D. Rao, "Extension of SBL algorithms for the recovery of block sparse signals with intra-block correlation," *IEEE Transactions on Signal Processing*, vol. 61, no. 8, pp. 2009–2015, 2013.

[176] Q. Wu, Y. D. Zhang, M. G. Amin, and B. Himed, "Complex multitask Bayesian compressive sensing," in *Proceedings of the IEEE International Conference on Acoustics, Speech and Signal Processing*, 05 2014, pp. 3375–3379.

[177] C. Y. Chen and P. P. Vaidyanathan, "MIMO radar ambiguity properties and optimization using frequency-hopping waveforms," *IEEE Transactions on Signal Processing*, vol. 56, no. 12, pp. 5926–5936, 2008.

[178] H. L. Van Trees, *Optimum Array Processing: Part IV of Detection, Estimation, and Modulation Theory*. John Wiley & Sons, 2002.

[179] C. Steffens, M. Pesavento, and M. E. Pfetsch, "A compact formulation for the $\ell_{2,1}$ mixed-norm minimization problem," *IEEE Transactions on Signal Processing*, vol. 66, no. 6, pp. 1483–1497, 2018.

[180] S. Kikuchi, H. Tsuji, and A. Sano, "Pair-matching method for estimating 2-D angle of arrival with a cross-correlation matrix," *IEEE Antennas and Wireless Propagation Letters*, vol. 5, pp. 35–40, 2006.

[181] G. Lu and W. Ping, "Comments on 'Pair-matching method for estimating 2-D angle of arrival with a cross-correlation matrix'," *IEEE Antennas and Wireless Propagation Letters*, vol. 7, p. 807, 2008.

[182] J. D. Taylor, *Ultra-wideband radar technology*. CRC press, 2000.

[183] P. D. Smith, S. R. Cloude, and R. J. Fontana, "Recent applications of ultra wideband radar and communications systems," *Ultra-Wideband, Short-Pulse Electromagnetics 5*, pp. 225–234, 2002.

[184] Y. D. Shirman, S. P. Leshchenko, and V. Orlenko, "Advantages and problems of wideband radar," in *Proceedings of the 2003 International Conference on Radar*. IEEE, 2003, pp. 15–21.

[185] Y. Rahayu, T. A. Rahman, R. Ngah, and P. S. Hall, "Ultra wideband technology and its applications," in *Proceedings of the 2008 5th IFIP International Conference on Wireless and Optical Communications Networks (WOCN'08)*. IEEE, 2008, pp. 1–5.

[186] Nanzhi Jiang, Renbiao Wu, and Jian Li, "Super resolution feature extraction of moving targets," *IEEE Transactions on Aerospace and Electronic Systems*, vol. 37, no. 3, pp. 781–793, 07 2001.

[187] J. Yu, J. Xu, Y. Peng, and X. Xia, "Radon-Fourier Transform for Radar Target Detection (III): Optimality and Fast Implementations," *IEEE Transactions on Aerospace and Electronic Systems*, vol. 48, no. 2, pp. 991–1004, 2012.

[188] F. Roos, D. Ellenrieder, N. Appenrodt, J. Dickmann, and C. Waldschmidt, "Range migration compensation for chirp-sequence based radar," in *Proceedings of the 2016 German Microwave Conference (GeMiC)*, 2016, pp. 317–320.

[189] R. P. Perry, R. C. DiPietro, and R. L. Fante, "Sar imaging of moving targets," *IEEE Transactions on Aerospace and Electronic Systems*, vol. 35, no. 1, pp. 188–200, 1999.

[190] Y. He, P. Aubry, F. Le Chevalier, and A. Yarovoy, "Keystone transform based range-Doppler processing for human target in UWB radar," in *Proceedings of the 2014 IEEE Radar Conference*, 2014, pp. 1347–1352.

[191] S. Bidon, L. Savy, and F. Deudon, "Fast coherent integration for migrating targets with velocity ambiguity," in *Proceedings of the 2011 IEEE Radar Conference*, 2011, pp. 027–032.

[192] F. Uysal, "Comparison of range migration correction algorithms for range-Doppler processing," *Journal of Applied Remote Sensing*, vol. 11, no. 3, pp. 1 – 10, 2017.

[193] Z. Xu, C. J. Baker, and S. Pooni, "Range and Doppler Cell Migration in Wideband Automotive Radar," *IEEE Transactions on Vehicular Technology*, vol. 68, no. 6, pp. 5527–5536, 2019.

[194] Z. Ahmad, Y. Song, and Q. Du, "Wideband DOA estimation based on incoherent signal subspace method," *The International Journal for Computation and Mathematics in Electrical and Electronic Engineering*, vol. 37, pp. 1271–1289, March 2018.

[195] Y. Bai, J. Li, Y. Wu, Q. Wang, and X. Zhang, "Weighted incoherent signal subspace method for DOA estimation on wideband colored signals," *IEEE Access*, vol. 7, pp. 1224–1233, 2019.

[196] H. Chen and J. Zhao, "Coherent signal-subspace processing of acoustic vector sensor array for DOA estimation of wideband sources," *Signal Processing*, vol. 85, pp. 837–847, 04 2005.

[197] E. Doron and M. A. Doron, "Coherent wideband array processing," in *Proceedings of the IEEE International Conference on Acoustics, Speech, and Signal Processing*, vol. 2, 1992, pp. 497–500.

[198] H. Wang and M. Kaveh, "Coherent signal-subspace processing for the detection and estimation of angles of arrival of multiple wide-band sources," *IEEE Transactions on Acoustics, Speech, and Signal Processing*, vol. 33, pp. 823–831, 08 1985.

[199] H. Hung and M. Kaveh, "Focussing matrices for coherent signal-subspace processing," *IEEE Transactions on Acoustics, Speech, and Signal Processing*, vol. 36, no. 8, pp. 1272–1281, 1988.

[200] J. Tsao and B. D. Steinberg, "Reduction of sidelobe and speckle artifacts in microwave imaging: the clean technique," *IEEE Transactions on Antennas and Propagation*, vol. 36, no. 4, pp. 543–556, 1988.